To the Graduate Council:
I am submitting herewith a dissertation written by Laurene Tetard entitled "Surface and Subsurface Physical and Chemical Characterization of Materials at the Nanoscale." I have examined the final electronic copy of this dissertation for form and content and recommend that it be accepted in partial fulfillment of the requirements for the degree of Doctor of Philosophy, with a major in Physics.

Thomas Thundat, Major Professor

We have read this dissertation
and recommend its acceptance:

Ali Passian

Norman Mannella

Hanno Weitering

Accepted for the Council:

Carolyn R. Hodges

Vice Provost and Dean of the Graduate School

(Original signatures are on file with official student records.)

Surface and Subsurface Physical and Chemical Characterization of Materials at the Nanoscale

A Dissertation

Presented for the

Doctor of Philosophy

Degree

The University of Tennessee, Knoxville

Laurene Tetard

December 2010

.

To my sister.

Acknowledgements

Though only my name appears on this dissertation, many people contributed to this achievement. It is very important for me to recognize all those people.

I would like to express my gratitude to my advisor, Prof. T. Thundat, for giving me the opportunity to accomplish this work in his group. I have really learned a lot from his experience and his advice. I would like to thank my advisor and friend, Dr. A. Passian, for his guidance, his constant encouragements and his trust. This experience would not have been the same without him. I am also deeply grateful to Prof. J.P. Goudonnet, who has contributed to my successful journey in so many ways.

All my appreciation to Dr. R.H. Farahi for her contribution, help and support throughout this process. I am very thankful to Dr. B. Davison, who gave us the opportunity to be part of the BioEnergy Science Center at the Oak Ridge National Laboratory. Dr. B. Davison has been a real support and his scientific insight has always made my work more valuable. I would like to express my appreciation to all the other group members, professors and staffs who have contributed to my education, in particular my committee members Dr. H. Weitering and Dr. N. Mannella.

A tribute to my family, for making me who I am, and supporting me through this experience. To my sister, we have made it together. To *ma petite sœur de cœur*, who has helped me become wiser and stronger, we will keep moving forward.

To my friends, who have been taking care of me throughout the years, who have made me laugh and who have taught me so much: Thank you.

Le doute est le commencement de la sagesse.

Aristote - from *Ethique à Eudème*

Abstract

The discontinuity in the atomic fabric of materials that defines the transition into a new medium gives rise to intriguing properties. Examples include the electronic tunneling behavior in scanning tunneling microscope or gigantic enhancement in the Raman emission from molecules near the surfaces of noble metals.

In modern microscopy, spatial and spectral resolutions are of great importance in tackling questions related to material properties. The emergence of the atomic force microscopy (AFM), which surpasses what can be achieved optically due to the inherent diffraction limit, has opened numerous opportunities for investigating surfaces. However, a contemporary challenge in nanoscience is the non-destructive characterization of materials. The ability to non-invasively explore subsurface domains for presence of inhomogeneities is of tremendous importance. In addition, techniques providing both physical and chemical information are needed to reach a comprehensive understanding of the composition and behavior of complex systems.

In order to tackle the subsurface and spectral imaging, here we propose to make use of the nonlinear interaction forces between the atoms of an AFM probe tip and those of a given sample surface. Such forces are known to contain a short range repulsive component and a long range van der Waals attractive contribution. This interfacial force can give rise to a multiple-order nanomechanical coupling between the probe and the sample, offering tremendous potential for obtaining a host of material characteristics. By applying a multi-harmonic mechanical forcing to the probe and another multi-harmonic forcing to the sample, we obtain, via frequency mixing a

series of new operational modes. By varying the nature of the excitations, using elastic or photonic coupling, it is possible to obtain physical and chemical signature of a heterogeneous medium with nanoscale resolution. The technique, termed mode synthesizing atomic force microscopy (MSAFM) is therefore described as a generalized multifrequency AFM.

We highlight the versatility of MSAFM and its potential to contribute to important problems in material sciences, toxicology and energy research, by presenting three specific studies: 1- imaging buried nanofabricated structures; 2- investigating the presence and distribution of embedded nanoparticles in a cell; and 3- characterizing the complex structures of plant cells.

Contents

Chapter 1

Introduction

1.1 Probing the world at the nanoscale

The emergence of nanotechnology and nanosciences has had a tremendous impact on many aspects of our lives. The interests towards the fundamental mechanisms of natural phenomenon are growing with the advances in technology. Thus, there is a permanent need for novel metrology tools that can contribute to the structural and chemical characterization of nanoscale features. A crucial component in dealing with systems at the sub-micrometer scale is the ability to measure the sought properties and response of the material under investigation, with high spatial and temporal resolution but minimum disturbance.

A variety of advanced characterization techniques are available for understanding the properties of bulk materials at macro and microscale. The basic principles of mathematics, physics, chemistry or biology are necessary to assess the structure of the material, its influence on the physical and chemical properties and potentially predict its response to a given set of external triggers.

Nanoscale characterization is a relatively new area. In his talk to the American Physical Society in 1959, R.P. Feynman seeded the idea of "manipulating and controlling things on a small scale" [1]. He emphasized the importance of developing

better characterization tools by devoting a section on the need for "better electron microscopes". His talk, "There is plenty of room at the bottom" [1], is now considered as a visionary reference in the field of nanoscience. His ideas were realized in the development of the scanning tunneling microscope (STM) in 1981 [2], followed by the discovery of buckyballs in 1985 [3] and the invention of the Atomic Force Microscope (AFM) in 1986 [4], marking the beginning of a new era. At this scale, the phenomena originating from quantum mechanics compete with behaviors usually observed at larger scales were classical mechanics predominate. Graphene is a timely illustration of such perspective. In essence, graphene could be considered as a monolayer of graphite. The physical properties of graphite have been largely studied. Graphite is made exclusively of carbon, arranged in a layered planar structure, in which each layer represents a hexagonal lattice. Graphite is an electrical conductor in the plane of the layers. However, electrons and phonons move with difficulty from one layer to the other. After the first successful mechanical exfoliation of graphene flakes by Geim A. and Novoselov K. (Nobel Prize 2010) at the University of Manchester, the unique electronic properties of graphene were observed, such as its metallic behavior, its Young's modulus, and specific behaviors such as the anomalous quantum Hall effect directly resulting from quantum mechanical effects [5, 6, 7, 8, 9].

Complementary to the physical properties of the samples, high spatial resolution spectroscopy holds great promises to obtain a chemical signature of materials. However, diffraction limited optics suffering an inability of focusing the light beyond a photon wavelength dependent threshold calls for new approaches of acquiring spectroscopic information. To date, while spectroscopy techniques are available as standard analytical tools for bulk samples, chemical identification of molecules at the nanoscale remains a challenge. Single atom spectroscopy has been attempted in very complex configurations such as Penning traps, or scanning tunneling microscopes [2] with severely reduced practicality. No system is currently capable of acquiring highly spatially resolved spectra of material in their native host and environment. Therefore, there is a great need for innovations to provide spectral coverage at the

spatial resolution in the submicrometer range and beyond to a few nanometers and ultimately to single atoms. A technique that would successfully provide structural and chemical information on the composition of nanoscale features located on the surface or within a larger complex sample must be developed. The flexibility of Scanning Probe Microscopy (SPM) systems and their performances for high spatial resolution imaging make them the best platforms for innovative techniques aiming at nanoscale characterization. SPM techniques have the potential to host complex evolving platforms, where mechanical and electromagnetic waves can be coupled to the sample in quest of a unique signature of complex submicronic structures.

A potential route may consist of utilizing the nonlinear coupling resulting from the localized probe-sample interaction in AFM to monitor the response of the sample interacting with the photons. The signature of a given molecule is unique and gives important insights on the electronic transitions, rotational and vibrational modes of the chemical bonds present in the material. While recent SPM works suggest that such an approach is plausible, many milestones are to be met to reach the desired resolution, that is, beyond what micro-Raman, micro-infrared, and optical near-field techniques currently offer [10, 11, 12].

1.2 What's below the surface?

A large number of materials are opaque to light. At the macroscale a number of technologies have been developed to circumvent this limitation and explore what is happening below the surface. A prime example is the development of imaging techniques in medecine that make monitoring the activity of the brain, the heart or a fetus in a womb possible and common practice nowadays. However, nanoscale characterization has been predominantly limited to surfaces and interfaces leaving the subsurface as a fantastic opportunity for exploration. Important physical processes in complex systems, such as natural phenomena, take place below the surface with mechanisms happening at the nanoscale. Ultrasonic imaging plays an important

role in subsurface imaging (medical imagery, $\cdots$), however the spatial resolution of ultrasonic-based techniques is rather limited due to the wavelength dependence associated to Abbe's principle. Consequently, coupling ultrasonic waves to a high resolution imaging technique has the potential to become a powerful way to investigate the subsurface information contained in the materials/samples.

1.3 Outline

The major part of this work has been dedicated to the development of new instruments and on demonstrating how they can be contribute to important biological problems.

In Chapter 2, we review the different techniques available when dealing with characterization of materials at the nanoscale, with a specific focus on Atomic Force Microscopy (AFM). The AFM is the core of the subsurface and spectroscopic studies we will discuss in Chapter 5. Thus, we also introduce some important concepts on the interaction of the tip and the sample, which is the core of the heart of the AFM measurements.

Chapter 3 is an overview of the current capabilities of the SPM techniques, where the challenges and promises of our work are presented. We will introduce the concept of using an AFM and mechanical excitations of the probe and the sample for subsurface imaging. In addition, we will demonstrate that the ability to identify the features through a careful study of their structural and chemical composition is an important and challenging problem and we propose to tackle it here by adapting an infrared source of light to illuminated the sample under investigation in the AFM, and let the radius of curvature of the tip of the probe define the resolution. The ultimate goal is to develop an acoustic and spectroscopy based AFM to enable sub-100nm spatial surface resolution with chemical recognition for surface and subsurface elements.

We present the details the experimental designs in Chapter 4. Developing new instruments for subsurface and chemical characterization is a complex task. First,

a careful study of the probes, which are the core of the tip-sample interaction is required in order to understand the rich mechanical behavior of the microscope in action. The customization of the AFM systems for elastic and photonic coupling is not straightforward. We discuss the different compromises that had to be made to achieve our goals. We start with a brief overview of the standard modes of operation of the AFM and then discuss some solutions to couple ultrasonic waves to the probe and the sample. Finally we examine the possibility of photonic coupling to the sample and/or the probe in order to access chemical information of materials at the subwavelength scale. We also introduce the three major applications we targeted during the course of this work to demonstrate the versatility of the synthesized modes by presenting three specific studies: 1- imaging a nanofabricated structure made up of nickel nanoparticles embedded in a germanium matrix residing on a quartz substrate; 2- investigating the presence and distribution of embedded nanoparticles in a cell, an important problem in nanotoxicology; and 3- characterizing the complex structures of plant cells, an important problem in bioenergy research. The first study is shown to serve as a preliminary calibration of the MSAFM subsurface modes. The second study demonstrates the applicability of MSAFM to investigate nanoparticle detection within cells by imaging single-walled carbon nanohorns and silica nanoparticles in macrophages and red blood cells. The third study aims to broaden the application of the MSAFM modes to plant cells by investigating poplar cross sections for the study of intricate networks of celluloses, hemicelluloses and lignins polymers in the cell walls.

Finally in Chapter 5, we analyze and discuss our results. We start by introducing the notations necessary to describe the novel measurements we perform with the Mode Synthesizing Atomic Force Microscope (MSAFM), and we describe how we propose to break the limits of resolution for mechanical and chemical characterization of materials at the nanoscale, with important impact on biology. In particular we present for the first time results revealing the presence of nanoparticles inside

mammalian cells. We also investigate the chemical composition of the plant cell walls, for lignocellulosic biomass of interest in biofuel research.

Chapter 2

Nanoscale Imaging

2.1 Background

Exploring the world that is invisible to the naked eye has been the main focus behind the development of microscopy. While the first microscopes consisted of simple pieces of glass, later named lenses, the instrumentation developed in the past thirty years has led to more complex systems that can now reach atomic resolution. Optical, electron and acoustic microscopy are widely spread among the techniques available to attain sub-micron spatial resolution. A different type of microscopy, one that does not use lenses, debuted in 1981 with the Scanning Tunneling Microscope (STM) [13]. From then on, scanning probe microscopy (SPM) [2, 4] established itself as the leading tools for such investigations and offers a great variety of capabilities for the characterization of samples ranging from semiconductors to live bacteria. Over the past two decades, the realization that atomic resolution was attainable [14] through measurements of the mechanical interactions or electronic tunneling currents opened the way to great discoveries with respect to the various properties of materials, e.g. metals, semiconductors, insulators, $\cdots$. In particular, recent progress in nanomechanics has demonstrated the flexibility of SPM in achieving high-resolution imaging, mappings of molecular forces and chemical compositions in various environments. A prime

example, the AFM [4], is capable of dynamically feeling and decoding the world of the nanoscale. However, this evolving success has been predominantly limited to surfaces and interfaces leaving the subsurface as a fantastic opportunity for exploration [15]. From biological processes to complex semiconductor-based devices, the information buried in the systems is often of great interest, making techniques with the ability to non-invasively feel subsurface properties of materials central in biology or material sciences.

2.1.1 Optical Microscopy

Optical microscopy is based on focusing the light onto a sample, using a succession of lenses. The insight in the optical world provided an overview of undesired effects such as the diffraction limit ($\lambda/2$ in air) that determines the maximum optical resolution. Abbe's principle, presented in 1872, describes the fundamental maximum of the resolution that can be achieved using optical microscopy given the diffraction limit, i.e. two objects separated by less than $\lambda/2$ with λ the wavelength of light, cannot be resolved using conventional optical microscopy. The ability to study living organisms (cells or bacterias for example) is one of the strength of optical microscopes. Bright field, dark field, confocal and fluorescence microscopes are possible variations of the optical microscopes [16, 17]. Confocal microscopy is a powerful optical imaging technique now commonly used in biology. The ability to non-invasively investigate an organism and reconstruct a 3D representation of the system, providing insights on the structure and behavior of the system is an important attribute in the study of living organisms. Confocal fluorescence microscopy is widely used for the sub-cellular investigation of cells [18, 19]. Fluorescence measurements are carried out by labeling the nanoparticles before letting them interact with the cells. Although the process allows recognition and tracking of nanoparticles in different organelles of the cell, it remains limited by the development of highly specific fluorescent labels. With techniques such as confocal microscopy, bright field or dark field microscopy, it is

possible to observe phenomena at scales larger than that of the diffraction limit of light. However, it is then necessary to turn to complementary techniques for studies at smaller scales.

2.1.2 Electron Microscopy (EM)

Electron microscopy was developed as a technique to circumvent the diffraction limit. The beam of electrons is used to probe the sample resulting in a significantly increased resolution. E. Ruska was awarded the Nobel Prize in Physics in 1986 for his work and the introduction of the electron microscope in 1930 [20]. EM takes advantage of the small de Broglie wavelength of electrons to reach magnifications of up to x1.5.10^8 in transmission mode. Consider an electron of rest mass m_e, charge q_e and energy $E_e = m_e.c^2 = 511\ keV$, the corresponding wavelength for a beam energy of 1V is approximately 1 nm, and it reaches 1 pm for a beam energy of 100 kV. The maximum electron beam energy in conventional Scanning Electron Microscopes (SEM) usually comes close to 30 kV.

Since then, advances in the field made atomic resolution possible [21]. Although there is a clear advantage for higher resolution imaging using EM, the harsh environment imposed on the sample when performing the measurements is quite detrimental for biological samples. Note that late improvements of the instrumentation now allow environmental studies [22], which expands the reach of the technique to biological applications.

Electron microscopy is an imaging technique commonly considered in material studies, for its high spatial resolution capability. SEM and transmission electron microscopy (TEM) are the main configurations used for EM. SEM is usually used for morphology inspection and e-beam lithography in nanofabrication. In TEM the detector monitors the beam of electron transmitted through the sample.

2.1.3 Scanning Probe Microscopy

Scanning probe microscopy covers a family of techniques based on scanning a sharp tip across the surface of a sample to provide measurements at the nanoscale [23]. A range of techniques are available to non-invasively characterize materials, and access their physical, structural and chemical properties with high spatial resolution. The general principle of operation was first introduced by Binnig at a.l [13] with their work on the Scanning Tunneling Microscope (STM). In STM, a bias voltage between the tip of the probe and the sample is applied and tip-sample distance is reduced to only a few tens of nanometers, until a tunneling current can flow between them. The tunneling current is a quantum mechanical effect. It responds exponentially to the tip-surface distance, which can be derived from the particle in a box model. The unique nature of the STM stands in that it does not use lenses to generate the image. Instead, the tunneling current is maintained constant through a feedback loop and the tip-sample distance is monitored as a function of the lateral position of the probe over the sample. The mapping of the sample is reconstructed from the measurements at each point of the scan to generate a 3D image. In contrast to EM, STM can be operated at the ambient or in liquid. Consequently STM found applications in various domains such as electrochemistry, semiconductor science or superconductivity. However the main limitation of the STM is the requirement for the sample to be conductive. The AFM was developed soon after to overcome this limitation [4]. In AFM the forces between the tip of the cantilever and the sample are monitored. The AFM will be discussed in more details hereafter.

Near field scanning optical microscopy (NSOM) is another probe-based technique aimed at generating images with resolution higher than the diffraction limit. Synge [24] first introduced the concept of a subwavelength light source (the probe) scanned in the vicinity (distance probe-sample $< \lambda$) of the surface of the sample for subwavelength imaging. The first implementation of this concept was presented by Ash and Nicholls [25] in 1972. In their proof of principle, microwaves were used

to illuminate the sample, leaving more flexibility for the dimension of the aperture of the probe. Indeed in the 1970s the capabilities in terms of nanofabrication, which would have been required for illumination of the sample in the Near Infrared Range (NIR), were not available. In recent years, the NSOM has emerged has a powerful tool in photonics/plasmonics and biology. Due to their small dimensions and dynamic reactions, the lipids and proteins and the associated mechanisms surrounding the cell activity, still remain underexplored. Taking advantage of the advances in NSOM instrumentation, in particular the development of nanoantennas for the probes, Garcia-Parajo and coworkers [26, 27] proposed a step forward in the possible applications of NSOM in biology. Their results revealed a specific architecture of protein receptors on the cell in the absence of ligands associated to the adhesion properties of the cells. The NSOM exhibits a great potential for the investigation of processes of the cellular membrane[26, 27]. [24, 25, 28, 26, 27]

2.2 Atomic force microscopy

The development of the AFM has opened the door to many new ideas while studying a variety of materials from conductors to insulators, in various environments (air, liquid,

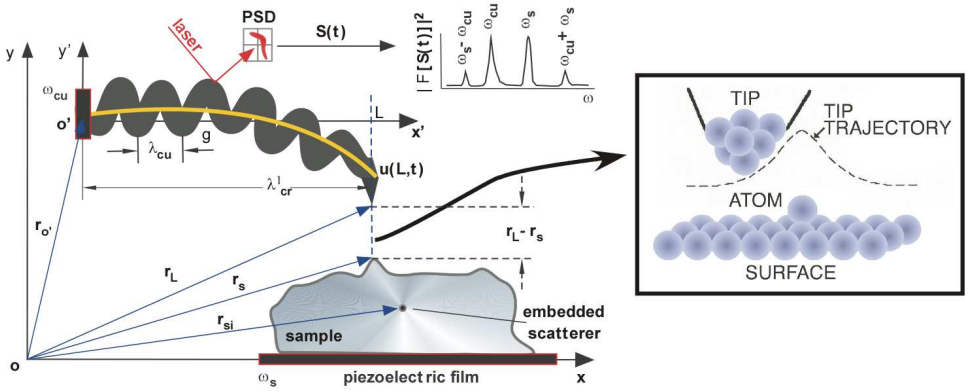

Figure 2.1: Tip-sample interaction in Atomic Force Microscopy. Schematic representation of the nonlinear frequency difference generation. Modeling geometry of the oscillating probe interacting via the tip apex with the oscillating sample.

controlled environment). The main components of the AFM include the head, where the cantilever is positioned and the scanner used to raster the probe over the surface of the sample. The sample is positioned on the base. An optical read-out system is built-in the AFM head: after aligning the diode laser beam on the cantilever, the reflected beam goes to a mirror directing the light to a positon sensitive detector (PSD), as indicated in Fig. 2.1 [29]. Depending on the configuration of the system, either the cantilever or the sample is mounted on a piezoactuator-based scanner. A controller manages the information (controls the scan parameters, monitors the read-out, processes the data in the form of a 2D map or a force curve, $\cdots$). The characteristics of the probe and parameters used by the controller are directly related to the mode of operation selected to perform a scan with the AFM. *Contact mode* and *non-contact (tapping) mode* are the most common ways to run the system.

In *contact mode*, the cantilever is brought in contact with the sample, and the deflection of the cantilever is monitored as it scans the sample, maintaining the force between the probe and the sample constant. The deflection of the cantilever is generally measured by optical deflection, as described above. The signal extracted from the PSD depends on the mode of operation. In *contact mode*, the vertical deflection of the cantilever is monitored. In *non-contact mode*, as the cantilever is driven close to its first natural resonance, the amplitude (R) and the phase (θ) of the signal at the reference (driving) frequency are extracted.

A variety of other techniques could be listed here but the purpose of this manuscript is not to be exhaustive so we will just note that for most of the other modes of operation the mechanisms of detection and data processing mostly consist in a deflection measurement or in monitoring the amplitude and phase of a particular frequency of interest of the system through lockin detection. The information contained in the image formed through this process is solely related to the surface morphology or the mechanical (and eventually physical) properties of the sample.However, a standard AFM is deprived from the ability to reach chemical information.

Chemical force microscopy (CFM) is the one of the few techniques, described in the

literature, capable of chemically investigating the sample using an AFM [30, 31, 32]. CFM uses functionalized AFM cantilever tips, and can provide a *yes or no* information for a selected analyte. Moreover, functionalization of the AFM tip so as to have a single receptor is a challenging task. In CFM, the tip with a single receptor is scanned along the surface to detect increases in receptor-analyte interaction forces in localized areas. Changes in the interaction forces can be monitored and processed to generate a compositional map of the surface of the sample. The applications of CFM, which rule the type of functionalization required for the probe, are still mostly limited to hydrophobic-hydrophilic measurements and protein-related measurements, due to the complexity of the functionalization step.

At larger scales, spectroscopy techniques are used to identify the composition of materials. The interaction of electromagnetic waves with matter engenders vibrations of the lattices or excitation of atoms to higher level of energy in the sample. Molecular vibrations,which occur in the infrared region of the spectrum of light for organic materials, constitute a characteristic signature of a network of atoms. Considering a molecule as a complex network of masses and springs, each of which having characteristic IR-active vibrational modes and studying the radiation-matter interaction for a range of wavelengths, is the idea behind infrared spectroscopy. The measurements result in a fingerprint of the molecule characteristics of the vibrational modes of the network of atoms in the compound. The fingerprint is unique to a given molecule, and sensitive to the crystallinity, conformation or polarization of molecules assembled in bulk material. However, standard IR spectroscopy has poor spatial resolution.

Recently Dazzi et al. developed a photothermal concept capable of submicron resolution for spectral analysis [33, 34]. In the general case of photothermal spectroscopy, a bimaterial cantilever bends depending on the number of photons it absorbs. The cantilever works as a sensitive heat detector. It is also possible to detect the thermal energy by monitoring the amplitude associated with the vibrations of the bimaterial cantilever at a particular frequency. Although of major interest for

research purposes, the system developed by Dazzi et al. uses a free electron laser source from a synchrotron for their studies, which makes it difficult to export the technique into a benchtop system. An adaptation of this technique was recently implemented in a commercial system, the *Anasys NanoIR*, in which a tunable laser illuminates the sample via the evanescent wave, resulting from the total internal reflection configuration. It is common practice in optics, especially in plasmonics, to use a prism (compatible with the range of wavelengths of illumination) and use the evanescent wave created at the surface to study the properties of a (metallic) sample. The main drawbacks of this configuration have to do with the limited spatial resolution caused by the photothermal nature of the process, and the limited range of illumination of the light source (based on nonlinear crystal) [35].

Another team led by Hammiche et al. also proposed to take advantage of the AFM to break the limit of diffraction in spectroscopy studies, using a Wollaston wire in place of the cantilever probe of an AFM to measure the localized variations of temperature induced by the photothermal response of the sample to the infrared illumination [36]. Monitoring the response of the sample using the probe of the Wollaston wire or the microcantilever permits to break the diffraction limit imposed by optical systems. However, the nature of the mechanisms at play limits the spatial resolution of the chemical information to about 100 nm. Indeed due to the difficulties in focusing the light to the surface, an area of the sample larger than that of the microcantilever is excited by the electromagnetic radiations and may have a contribution in the signal detected by the probe.

2.2.1 Spring-mass system

The cantilever used as the probe in the AFM is often referred to as a mechanical beam. The beam is one of the simplest distributed mechanical system. However a common model used to describe the interaction of the tip of the cantilever and the surface of the sample is the mass spring system. We will use this example to

illustrate the mathematical steps to derive the partial differential equations of the system [37, 38].

The Hamilton principle says that the time integral over the Lagrange function L, also called action, is a minimum. The Hamilton principle corresponds to the principle of least action. In other words, the trajectory of a mass m is where its action is minimal. The Lagrangian L is the difference between the kinetic and the potential energy, respectively T and U.

$$\int_{t_1}^{t_2} (T - U)dt = \int_{t_1}^{t_2} L.dt = minimum,$$

The equation of Euler (Lagrange/Newton) corresponds to the variation of the integral equated to zero.

$$\delta \int_{t_1}^{t_2} L(x, \dot{x}, t)dt = 0$$

We recall the Taylor expansion of a function f as:

$$f(x, \dot{x}, t) = f(x_0, \dot{x}_0, t) + \frac{\partial f(x, \dot{x}, t)}{\partial x}\delta x + \frac{\partial f(x, \dot{x}, t)}{\partial \dot{x}}\delta \dot{x} + ...$$

so that by replacing in the derivative:

$$\delta \int_{t_1}^{t_2} L(x, \dot{x}, t)dt = \int_{t_1}^{t_2} [L(x, \dot{x}, t) - L(x_0, \dot{x}_0, t)].dt$$

$$= \int_{t_1}^{t_2} \left[\frac{\partial L(x, \dot{x}, t)}{\partial x}\delta x + \frac{\partial L(x, \dot{x}, t)}{\partial \dot{x}}\delta \dot{x}\right].dt$$

The end points of the motion are fixed and serve as boundary conditions:

$$\delta x(t_1) = \delta x(t_2) = 0$$

. The second term in the integral can be partially integrated so that:

$$\int_{t_1}^{t_2} \frac{\partial L(x, \dot{x}, t)}{\partial \dot{x}}\delta \dot{x}].dt = -\int_{t_1}^{t_2} \frac{d}{dt}\left(\frac{\partial L(x, \dot{x}, t)}{\partial \dot{x}}\right).\delta x.dt$$

By inserting the results obtained above in the initial integral, we now have:

$$\delta \int_{t_1}^{t_2} L.dt = \int_{t_1}^{t_2} \left[\frac{\partial L}{\partial x} - \frac{d}{dt}\left(\frac{\partial L}{\partial \dot{x}}\right) \right] .\delta x.dt = 0$$

where the only solution is for the term inside the integral to be zero:

$$\frac{\partial L}{\partial x} - \frac{d}{dt}\left(\frac{\partial L}{\partial \dot{x}}\right) = 0$$

Since $L = T - U$ and $T = \frac{1}{2}m\dot{x}$, $U = \frac{1}{2}kx^2$, with m the mass and k the spring constant of the system, we can also derive Newton's equation: $m\ddot{x} + kx = 0$

2.2.2 Beam theory

The AFM probes, the cantilevers, are often considered as mechanical beams for theoretical considerations. A beam is a distributed system and their dynamical description involves deflection, stress, strain, and associated energies.

We introduce the following notations, some of which can also be found in Fig. 2.2: E is the Young's modulus of the material, σ represents the stress strain, A is the area of the cross section with $A = h.b$, h and b are the width and height of the cross

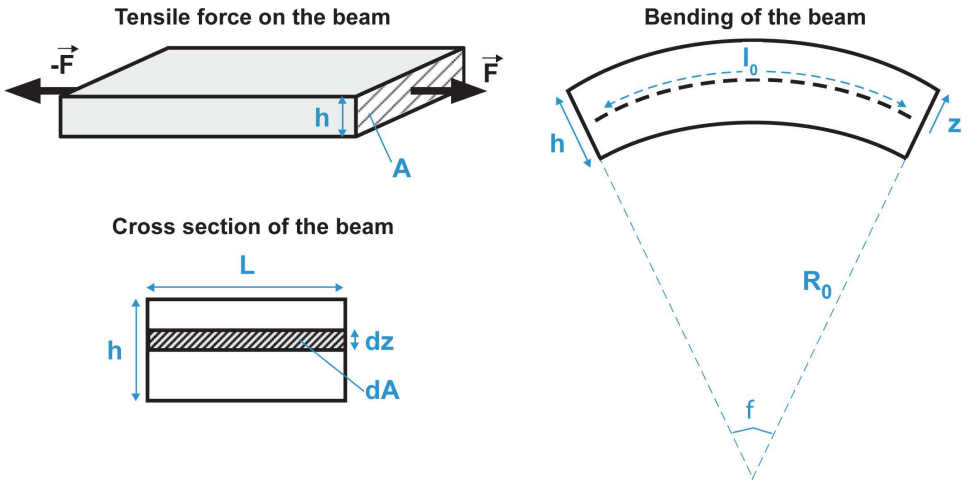

Figure 2.2: Illustration of the mechanical beam (Top left) Straight beam, (Right) Distorted section of the bent beam, (Bottom Left) Cross section of the beam.

section. The length of the beam is referred to as l, with l_0 the length of the beam at the unbent position. I is the moment of inertia, which equals $\frac{bh^3}{12}$ for a rectangle section.

Expression of the Lagrangian

The Lagrange function of a bent beam is reported in the literature to be:

$$L = \frac{1}{2}\int_0^l dx \left(\rho A \left(\frac{\partial w}{\partial t}\right)^2 - EI\left(\frac{\partial^2 w}{\partial x^2}\right)^2 - T_0\left(\frac{\partial w}{\partial x}\right)^2 - P_0 w\right)$$

with the potential energy contributions where $U^*_{ext} = -P_0(x)w(x)$ represents the term for the external contribution, $U^*_{ax} = \frac{1}{2}T_0\left(\frac{\partial w(x)}{\partial x}\right)^2$ the force acting on the beam or axial potential energy, $U^*_{bend} = \frac{1}{2}EI\left(\frac{\partial^2 w}{\partial x^2}\right)^2$ the force associated to the bending and the kinetic energy contribution of the beam $T^* = \frac{1}{2}\rho A\left(\frac{\partial w(x)}{\partial t}\right)^2$.

Stress and strain

The stress in a beam can be expressed in different ways : $\sigma = \frac{F}{A} = E\frac{\Delta l}{l}$ in the case of an elastic material. The strain ϵ is defined as the ratio of the elongation with respect to the original length: $\epsilon = \frac{\Delta l}{l}$. Note that we will neglect the deformation (contraction) of the slab in the direction of the normal axis that accompanies the deformation (elongation) along the axis of the force (see Fig. 2.2).
The energy along the axis, U_{ax}, can then be expressed as :

$$U_{ax} = \int F dx = \int AE\epsilon d(\epsilon l) = \frac{1}{2}AE\epsilon^2$$

Bending

When the beam or cantilever bends, the strain changes along the z-axis (see Fig. 2.2). The change in length is $l(z) = \phi(R + z)$, where $l(0) = l_0$. For bendings of small

amplitude, $\phi = \frac{l_0}{R}$ and the strain can be expressed as a function of z: $\epsilon = \frac{\Delta l}{l_0} = \frac{\phi z}{l_0} = \frac{z}{R}$. The energy associated to the bending, U_{bend}, can then be expressed as :

$$U_{bend} = \int \frac{1}{l_0} dU$$

where dU is the potential energy for a thin slice of the beam:

$$dU = \int F.d(\Delta l) = \int \sigma dA d(\epsilon l_0) = dA.l_0 \int (E.\epsilon) d(\epsilon)$$

$$dU = E.dA.\frac{l_0}{2}\epsilon^2$$

External load

The energy associated to the external load P_0 takes the form: $U_{ext} = -\int_0^l P_0(x)w(x)dx$

Euler Lagrange equation

By variation of the Lagrange function of a flexible beam, it is possible to obtain the Euler-Lagrange equation for the beam. We will just indicate the result here, as the details of calculations can be found in the literature [37].

$$\frac{\partial L^*}{\partial w} - \frac{\partial}{\partial t}\frac{\partial L^*}{\partial \dot{w}} - \frac{\partial}{\partial x}\frac{\partial L^*}{\partial w'} + \frac{\partial^2}{\partial x^2}\frac{\partial L^*}{\partial w''} = 0$$

where w' stands for a derivative with respect to x and $\dot{w}$ stands for a time derivative.

Boundary conditions

Finally the boundary conditions will be as follows:

$$\delta w(0)[T_0 w''(0) - EIw'''(0)] + \delta w'(0)EIw'''(0) = 0$$

$$\delta w(l)[T_0 w''(l) - EIw'''(l)] + \delta w'(l)EIw'''(l) = 0$$

There are some specific cases used as reference for the boundary conditions of a beam, but only two will be of interest for our case: (1) the clamped-free, which is used to represent a free cantilever, and (2) the clamped-simply supported, for the case of a cantilever in position engaged for AFM imaging.

2.2.3 Tip-sample interaction

Fig. 2.1 shows the schematic of MSAFM operation in presence of an interaction force. A microcantilever beam in a two-dimensional framework, where there is a base motion

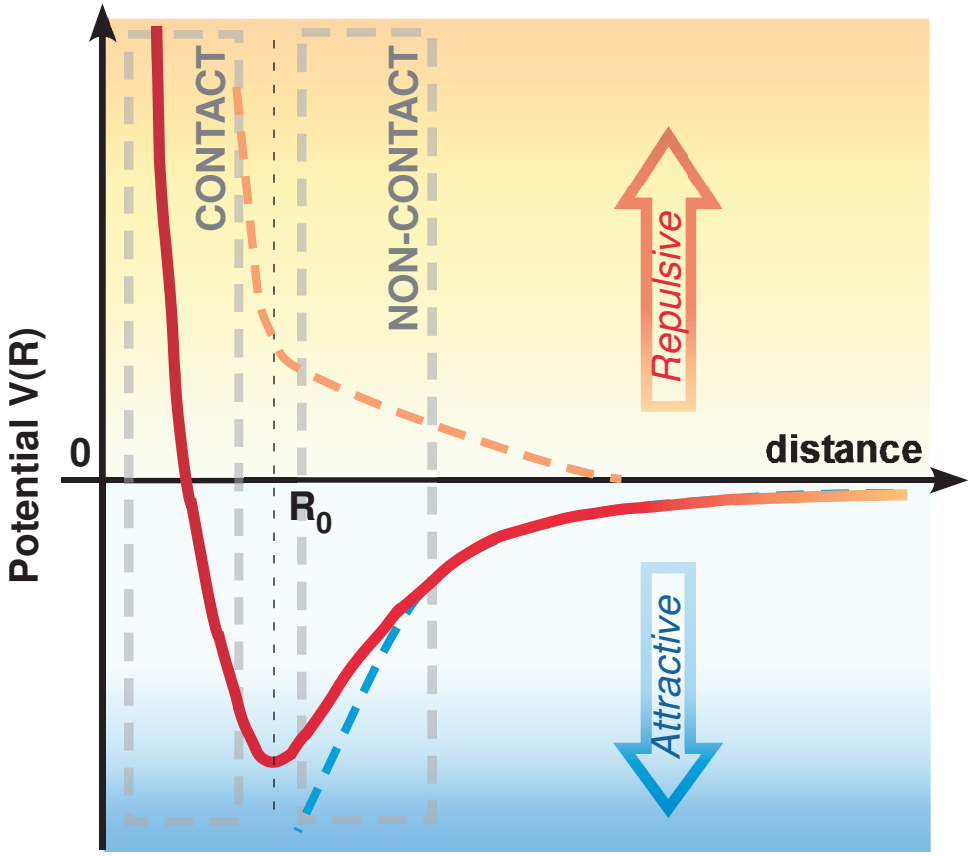

Figure 2.3: Interaction potential. The minimum at R_0 corresponds to the distance where the two atoms system reaches its equilibrium. For short range interactions, when $R < R_0$ the contribution of the repulsive force becomes predominant and the potential increases to ∞. For long range interactions, when $R > R_0$ the term corresponding the the attractive force is predominant and the potential tends to 0.

for the beam in x and y directions. Point P can be an arbitrary point on the beam with the transverse deflection of the beam represented by $w'(x', t')$ or $w(x', t)$ in the following coordinates:

- Coordinate of sample S : oxy inertial reference frame
- Coordinate of sample S' : $o'x'y'$ moving frame with beam base

In general, the origin of the moving frame is denoted by and represented as:

$$\vec{r}_{o'} = (x_{o'}, y_{o'}) = (g(t), h(t))$$

where $g(t)$ and $h(t)$ are respectively defined as the horizontal and vertical distances from the origin of the moving frame with respect to the origin of the inertial frame. Without loss of generality, a harmonic motion is assumed for $g(t)$ as:

$$g(t) = 0, h(t) = A_c cos(f_c t + \Psi)$$

where A_c is the amplitude, f_c is the excitation frequency, and Ψ is the phase of the base excitation, respectively. The point P, an arbitrary point on the beam, can be transformed to the inertial frame as:

$$\vec{r}_p = \vec{r}_{o'} + \vec{r'}_p$$

Moreover, the coordinate of the sample particle, S (representing the surface of the sample) in the moving frame can be transformed into the inertial coordinate as:

$$\vec{r}_s = \vec{r}_{o'} + \vec{r'}_s$$

Potential Energy

The Euler-Bernoulli beam model with structural damping for the microcantilever is considered here, with clamped-free boundary condition at one end and tip-mass m_e at the other end. The variation of the potential energy in the system can be expressed

as [39]:

$$\delta U = \frac{1}{2}\delta \int_0^L EI(w_{xx}(x,t))^2 dx = \int_0^L EI w_{xx}(x,t)\delta(w_{xx}(x,t))dx$$

Kinetic Energy

The kinetic energy of the system can be written as [39]:

$$T = \frac{1}{2}\int_0^L \rho \dot{\vec{r}}_p^2 dx + \frac{1}{2}m_e(\dot{g}(t)^2 + (\dot{h}(t)^2 + \dot{w}(L,t))^2)$$

consequently the variation of the kinetic energy in the system can be expressed as:

$$\delta T = \int_0^L \rho \dot{w}(L,t)\frac{d}{dt}(\delta(w(x,t)))dx + \int_0^L \rho \dot{h}(t)\delta(\dot{w}(x,t)dx) +$$

$$m_e \dot{w}(L,t)\delta(\dot{w}(L,t)) + m_e \dot{h}(t)\delta(\dot{w}(L,t))$$

Hamiltonian

Substituting the expressions above to the Hamiltons Principle formulation:

$$\int_{t_1}^{t_2} (\delta T - \delta U + \delta W)dt = 0,$$

it is then possible to derive the PDE of the beam [39]:

$$\rho \ddot{w}(x,t) + \rho \ddot{h}(t) + EI w_{xxxx}(L,t) + C w_{xt}(x,t) = 0$$

with boundary conditions: $w(0,t) = 0$, $w_x(0,t) = 0$, $w_{xx}(L,t) = 0$, and

$$m_e \ddot{w}(L,t) + m_e \ddot{h}(t) - EI w_{xxx}(x,t) = \Gamma(t)$$

The interaction potential between the tip and the sample is often estimated to a Lennard-Jones potential as depicted in Fig. 2.3.

Using a distributed-parameters modeling, and a general interaction force, we investigated the nature of the force involved in the formation of the difference mode in MSAFM. The extension of this work, in particular for the study of higher-level coupling modes will be presented elsewhere.

Chapter 3

Physical properties and chemical composition of materials at the nanoscale

What can we measure at the nanoscale? When one refers to physical or chemical properties of a material, it often relates to the properties of this material at the macroscale. At the macroscale the observations result from an average of the possible responses of the material to the excitation over the area under investigation and possibility over large time scales. In the case of nanoscale characterization, the volume of the material under investigation is substantially reduced. Using the AFM, the tip only "sees" the material in contact with the tip (few tens of nanometers), which leads to a need for new standards for control experiments. For example, in spectroscopy, it is quite common to study the sensitivity of a technique with respect to the concentration of a molecule in the blend of interest. However, in the case of nanoscale spectroscopy, what would it mean? Imagine the tip of a cantilever probing the surface of a copolymer, trying to identify the compounds in the system. It is unlikely that the domains would be smaller than the region of contact between the tip and the sample. Thus the probe will only see one domain (or a part of a domain)

at a time. Is concentration relevant then? At the macroscale, it is difficult to study the properties and effect of interfaces of different domains because their contribution will be encompassed in the contribution from the rest of the sample response. At the submicron level, interfaces and grain boundaries will have significant contribution. We will discuss here some of the properties of interest in various AFM-related studies reported in the literature.

3.1 Physical properties

The AFM probes the cumulative forces activity between the tip of the cantilever and the surface of the sample. But how is the force of the interaction registered? Various techniques have been developed to measure the behavior of the cantilever. We will discuss some of them in this section. The distance between the tip and the surface is of tremendous importance. The force results from the collective tip-substrate interaction and the atom-atom interaction. Thus at different distances, different forces will contribute. The short range forces generally predominate for $d < 10\ nm$, with d the distance between the tip and the surface of the sample. Van der Waals forces include three major contributions (i.e. orientation, induction and dispersion), and vary as $1/d^6$ (Fig. 2.3). Magnetic and electrostatic forces are longer range forces. Consequently, they can be measured in non-contact mode of the AFM.

3.1.1 Elastic properties

Contact Mode imaging

Contact mode is commonly operated for AFM imaging. The tip is brought in hard contact with the surface of the sample. Scanning across the region of interest, the deflection of the cantilever beam is mapped and represents the topography of the surface. In a feedback-loop system, the feedback in the system is constantly adjusted

for the cantilever deflection to remain constant. In open-loop system, the deflection alone is monitored.

Dynamic AFM Modes

The dynamic operation of the AFM is advantageous in that it reduces the contact between the tip and the sample, and consequently decreases the chances of damaging the sample, the wear of the tip as well as the friction between the probe and the sample. There are several possible modes of operation for dynamic imaging. The common method used for the characterization of soft matter samples is *intermittent contact mode*, also known as *tapping mode* imaging. The cantilever is oscillated at or close to its resonance frequency, and the amplitude/phase of the response are monitored during the scan. *Non-contact mode* is another method to probe the surface properties of the sample. In this case the tip does not come into contact with the sample. The force remaining between the tip and the sample are of the order of the picoNewton. Long range forces, such as magnetic or electric forces, can be measured with this configuration. The novel modes we present in this manuscript result from dynamic AFM configurations. For advanced implementations of AFM new modes, one should also consider the importance and advantages of phase contrast imaging and frequency modulation mode.

Lateral Force Microscopy LFM

In LFM, the AFM is operated in contact mode, but the "twist" of the cantilever in the horizontal direction is monitored instead of the vertical direction in standard AFM. The sticking or sliding of the tip resulting from the forcing on various regions of the sample is monitored using a PSD made of four domains (quad-cell). Thus, the topography information results from the $(A + C) - (B + D)$ measurement in the quad-cell, while the frictional information results from $(A + B) - (C + D)$. The concept of the quad-cell is illustrated in Fig. 3.1.

Numerous studies took advantage of this technique, for instance in polymers or assembled monolayers studies. Although the topography image can be relatively smooth, the contrast in LFM image may exhibit regions of various mechanical properties.

Force Modulation Microscopy FMM

In FMM the cantilever is mechanically excited at high frequency and the tip is positioned in the repulsive regime. By measuring the slope of the force-distance curve it's possible to retrieve some information on the elasticity of the sample. The measurements are usually presented along with topography images.

Magnetic and Electrostatic Force Microscopy

It is possible to investigate the magnetic response of a sample to a magnetic stray field or the localized surface charges in metals, semiconductors or insulators, with

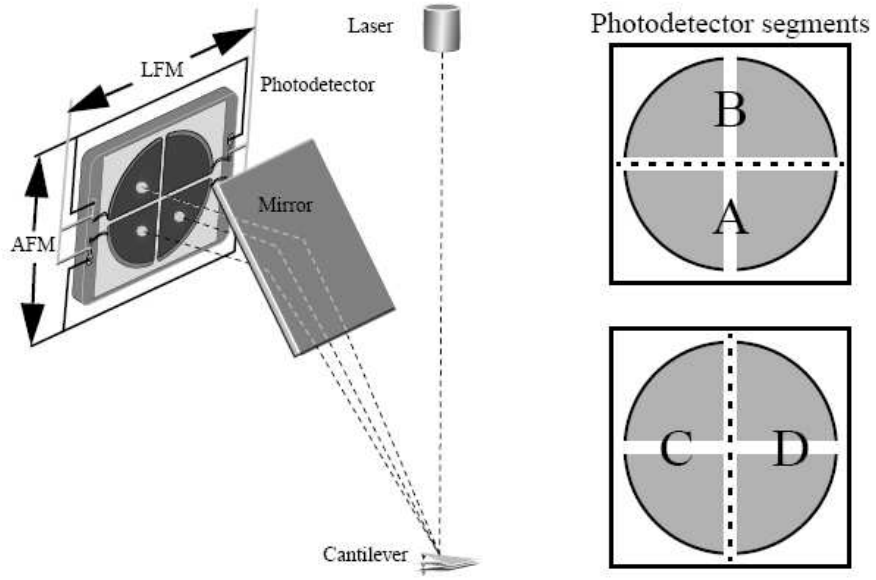

Figure 3.1: AFM read-out system. Representation of the concept behind the optical readout system common to various commercialized AFM system. *Source: Veeco Multimode Nanoscope III manual*

high resolution. For these types of measurement, the probe should be prepared with a specific coating. These techniques are usually operated in the dynamic mode, where the oscillations of the cantilever are monitored by a lockin amplifier. Amplitude and phase contributions contain important insights on the properties of the sample.

3.1.2 Heat transport properties

Thermal radiation is based on electromagnetic (EM) wave propagation and as such, can be described by Maxwell's EM wave equations. Statistical thermodynamics and quantum mechanics are also crucial in the understanding of the mechanisms associated with thermal radiations. Heat carriers in solids are divided in two types: 1- electrons, 2- phonons (crystal vibrations). At the macro and microscale, i.e. when the characteristic length in the system is larger than the photon wavelength at play, the problem is usually treated considering Planck's blackbody radiation law and Boltzmann transport equation. In the case of nanostructures, where the size of the structure is comparable or smaller than that the photon wavelength, these laws are no longer valid. Thermal radiations occur at various occasions in a solid. It is possible to perform a localized thermal analysis of materials using thermal probes in an AFM-like configuration. The concept is simple: by heating the sample locally using a specially designed thermal probe, the subsequent deflection of the probe, in contact with the sample, will contain information on the response of the material to the initial stimulus [40].

3.2 Molecular spectroscopy

We are constantly exposed and interacting with electromagnetic radiations, starting from the Sun and the stars but also from engineered sources. Spectroscopy is a specific

area of research interested in the interaction of electromagnetic radiations with atoms and molecules, used to identify the composition of materials and complex systems.

3.2.1 The chemical bond

Providing a description for the chemical bonds was one of the greatest achievements of quantum mechanics. Chemical bonding refers to the strong (attractive) forces holding the atoms of molecules and solids together. The nature of a chemical bond depends on the two atoms at play in the interaction. The normal modes of vibration of molecules resemble those of a mass-spring system, in which the modes of the system are directly linked to the mass and the spring constant. The resonances of the system can be excited through various external stimuli, including infrared and Raman spectroscopy.

3.2.2 Infrared spectroscopy

In FTIR spectroscopy, the range of wavelengths is comprised in the infrared region of the spectrum, and the spectrometer consists of a Michelson interferometer. The interferometer is composed of a beam splitter and two mirrors, a fixed mirror and a moving mirror. The incident light is split into two beams, one reflected off to the fixed mirror, the other one to the moving mirror. The different path of the two beams of light results in a phase difference, generally referred to as *optical retardation* or *optical path difference (OPD)*. The principle of operation is to first collect an interferogram, and then obtain the spectrum (absorption or transmission vs wavelength) by performing a Fourier Transform. Consequently, the reference point of the interferometer corresponds to the point where $OPD = 0$. In the FTIR spectrometer, all the wavelengths are collected simultaneously, causing the interferogram to be a quite complex signal.

In a spectrometer, the light source is focused on the sample and the light, whether scattered, absorbed or transmitted by the atoms and molecules, is detected for

analysis.

The transmitted intensity follows Beer-Lambert law:

$$I = I_0 10^{(-\varepsilon[J]l)},$$

where l is the length of the sample, [J] the molar concentration of the sample J, and ε the molar absorption coefficient. At fixed wavelength, the intensity of the electromagnetic radiation transmitted through the sample follows an exponential decrease with the length (or thickness) of the sample, and its molar concentration. The absorbance A is defined as follows:

$$A = log\frac{I_0}{I} = -logT = \varepsilon[J]l,$$

also known as the optical density.

FTIR spectroscopy measurements involve the illumination of the surface of the sample using an appropriate combination of optical components to focus the light onto the sample in the region of the probe-sample interaction. The response of the probe itself is used as a background to the FTIR spectra. Here, scanning the optical path difference results in recording an interferogram corresponding to the response of the thermal probe in time and space. Given that the probe can respond to the fast changes in thermal responses of the sample, it is then possible to resolve the absorption bands of the material under investigation.

3.3 Subsurface microscopy and spectroscopy

3.3.1 Challenges

In the microelectronics industry, where the complexity and the density of components grow exponentially, exploring and characterizing the subsurface regions represent a

real metrology challenge. Similarly in biology, the rising need to study localized biological processes requires the development of novel instruments. Auger electron spectroscopy (AES), Low energy electron diffraction (LEED), X-ray photoelectron spectroscopy (XPS), Time of Flight (TOF) spectroscopy, and other spectroscopy methods commonly used in physics or material science are considered as surface analysis techniques since they will probe up to 10 nm of the surface of the material. These techniques are usually operated in utra-high vacuum (UHV) to avoid contamination, which limits their practicability for problems such as nanotoxicology or biomass characterization. Throughout the literature, the term "subsurface imaging" take a slightly different meaning whether the application concerns solid state physicists, engineers or biologists. These nuances should be addressed in order to identify solutions in instrumentations. In solid state physics, subsurface refers to dopants or atoms 1-15 atomic layers below the surface, which would be considered as the surface for biologists. A biological cell is a closed entity. Its size can vary from 1 to 200 microns. The thickness of the cell membrane is typically of the order of 5-10 nm [41], out of the range of the "subsurface" techniques employed in solid state.

3.3.2 The potential of SPM

Subsurface imaging holds great promises for characterization at the nanoscale. Several attempts have been reported to access physical and chemical properties of buried features in bulk materials. We review here some of this work. Several attempts to determine the depth, size, shape of features one to fifteen atomic layers below the surface of metals using STM have been reported [42, 43, 44]. Schmid et al. [42] investigated the presence of argon (Ar) bubbles implanted in Al(111) crystals. The STM imaging conducted under UHV exhibits hexagonal features approximately 20 pm high and few nanometers in diameter, in addition to the Al(111) surface lattice. Changes in the tunneling voltage affect the form of the hexagons. In addition, the correlation between the number of features observed and the concentration of

the Ar determined by Auger spectroscopy infer that the hexagonal features are in fact electronic interferences originating from the bulkstates. The Ar bubbles form a quantum well between the surface of the sample and the subsurface reflector. As such, they display a quantized interference pattern with respect to the variations in tunneling current. Furthermore, theoretical considerations indicate that it is possible to deduce the shape of the embedded features given the interference patterns. Rose et al. [43] also demonstrate the possibility to differentiate distinct impurities in a Pd(111) substrate by studying the image contrast, diffusion properties and behavior of molecules adsorbed on the surface. Although the authors were able to identify sulfur as one of the inhomogeneities by carrying out AES measurements, their hypothesis on the other two atoms, namely carbon and oxygen, remain uncertain given the lack of tools for direct chemical speciation.

In cases where the region of interest is several hundreds of nanometers below the surface, acoustic imaging techniques have been coupled to AFM systems for studies in various environments [45]. Given the limits in spatial resolution of conventional acoustic microscopy, imposed by Abbe's principle, the developments in AFM provided a unique opportunity for atomic resolution. Various implementations of this concept, involving ultrasonic excitations of the sample and/or the tip, have been presented in the literature. A illustration of the concept is illustrated in Fig. 2.1. We review here the main ones, namely Ultrasonic Force Microscopy (UFM), Atomic Force Acoustic Microscopy (AFAM), intermodulation AFM, and Scanning Near-Field Ultrasound Holography (SNFUH). The atomic force microscopy (AFM) is now widely used in life sciences. It is advantageous because of simpler sample preparation and ability for ambient imaging. However, conventional AFM typically only probes the surface of a specimen, making it difficult [15] to analyze structures within a cell. AFM imaging is generally performed using contact or tapping mode imaging. In contact mode, the tip of the cantilever probe is in direct contact with the sample during the image scan, exerting a force of 50-100 pN on the sample at all time. In tapping

mode, the cantilever is mechanically excited close to its resonance frequency. The tip and the sample contact only at the lowest position of the oscillation, significantly decreasing the forces applied on the sample. Tapping mode is very popular in biological applications, especially for imaging of soft samples or samples that are not well attached to the substrate, which is generally the case in liquid environment. The measurements performed in contact or tapping provide insight on the surface and interfacial properties on the system of interest. Subsurface imaging with nanoscale resolution remains an underexplored area. One may envision this limitation as being due to a lack of mechanical excitation of the sample resulting in the inability of the probe to gather the subsurface dynamic attributes [48, 47, 90, 63]. The term UFM was coined by Kolosov et al. [46] to describe their technique. Exciting the sample with mechanical waves in the ultrasound frequency range results in vertical vibrations of the surface of the sample that the cantilever can detect. Since the resonance frequency of the probe is generally below 100 kHz, it cannot follow the surface vibrations at megahertz or gigahertz frequencies. However, the forcing applied on the sample engenders a periodic indentation of the probe and a shift in the average position of the "frozen" cantilever can be observed due to the nonlinear nature of the tip-sample interaction. Elastic properties of various materials have been reported using this technique [46, 47]. Rabe et al. [48] introduced a similar idea, although driving the sample (or the cantilever) at one of the resonance frequencies of the cantilever in contact with the surface of the sample. The resulting response of the system is much stronger, and allows qualitative and quantitative studies of local elastic properties. Young's modulus can be calculated from the contact stiffness and represented as an image. AFAM can be operated to obtain (1) cantilever vibration spectra or (2) acoustic images. A similar method was studied by San Paulo et al. [49] using the first bending mode of the probe to access topography information, and the second bending mode as reference in the external lockin to monitor the mechanical vibrations of the resonator. UFM and AFAM imaging can be performed in air or in liquid. Other techniques involving multiple forcings on the probe and/or

the sample have been developed. In the case of multiple excitations, the difference-frequency generation, resulting from the nonlinear tip-sample interaction, has been exploited to gain information on the mechanical properties of surface and subsurface features of materials. Rohrbeck and Chilla [50] presented the concept of exciting two SAWs sources with different frequencies and detecting the mixing (in particular at the difference frequency) using a so-called force sensor in the vicinity of the sample surface. Another system with two SAW sources (in the form of interdigital transducers) and a tip located at the surface of the sample was presented by Chilla et al. [51]. The nonlinear elastic effects of SAW propagation in the bulk are neglected. The nonlinear frequency mixing is generated by the nonlinear nature of the tip-sample interaction. Investigation of the influence of the topographical gradients on the phase of the difference peak signal is reported with a specific focus on the phase velocity dispersion at the nanoscale.

Similarly to the AFM, the capabilities of the techniques discussed above is in general limited to topography and physical properties (density, elasticity, $\cdots$). Subsurface imaging involving spectroscopy measurements is a complex problem and a limited number of works have discussed this problem in the literature. Anderson et al. [52] proposed to take advantage of the electromagnetic radiation response of the sample to the enhanced field of a laser-irradiated gold tip of a Near-field Raman microscope. Optical antennas in Near-field microscopy confine the radiations within a few tens of nanometer of the tip and thus enhance the signal levels. The calculations of the electromagnetic field distribution along the vertical axis of the tip indicate a strong decrease of the excitation field within the sample, although the major drop is associated to the gap between the tip and the sample. Note that near-fields are evanescent and thus follow an exponential decrease along the tip axis. Nevertheless, by experimentally decreasing the gap size while looking at nanotubes covered with a thin layer (5-10 nm) of SiO_2, it was possible to gain information on the location, shape and structure of defects induced phonon localization in the nanostructures. Similarly, using a scattering -type scanning near-field optical microscope (s-NSOM),

Taubner et al. [53] demonstrated that it is possible to reach subsurface imaging in the case of gold islands covered with PMMA. The near field interaction is directly related to the refractive index and the absorption of the material at the excitation wavelength. In the case of low refractive index and low absorption, the material simply act as a spacer between the tip and the buried structures. The technique presented offers yet another solution for high resolution nondestructive imaging, with access to subsurface and spectroscopic information. However, given the exponential drop in signal with respect to the distance from the tip, s-NSOM remains limited to few tens of nanometers in depth resolution.

Chapter 4

Experimental Design

4.1 Instrumentation

All the measurements presented here were performed on AFM systems commercialized by Veeco. MSAFM was primarily developed on a Multimode system (Fig. 4.1,Fig. 4.2) while the spectroscopy measurements were performed on a Dimension 3100 ((Fig. 4.3) with a Nanoscope III controller and a basic extender. A Signal Access Module (from Veeco), an oscilloscope with megahertz sampling rate (Agilent DSO5034A), lock-in amplifiers (200 Megahertz SRS 844, and SRS 530), and network analyzers for various bandwidths (HP 4195A, SRS SR760) were used to carry out all the measurements. Instrument automation and control, and data acquisition were implemented in Labview using GPIB communication.

4.1.1 Microcantilever probes

The individuality of SPM is in the probes they use and their specific response to the interaction of the tip with the surface of the sample. In the case of the AFM, the probe is a microcantilever designed with a tip of few tens of nanometers in diameter, and made of specific materials and geometries. Resonators are characterized by the quality of their oscillations around their natural modes. These parameters, in

particular the quality factor (Q-factor), the natural frequencies or the stiffness of the microcantilevers can then be optimally designed to meet the requirements imposed by specific applications. For instance, imaging soft tissues often requires to operate

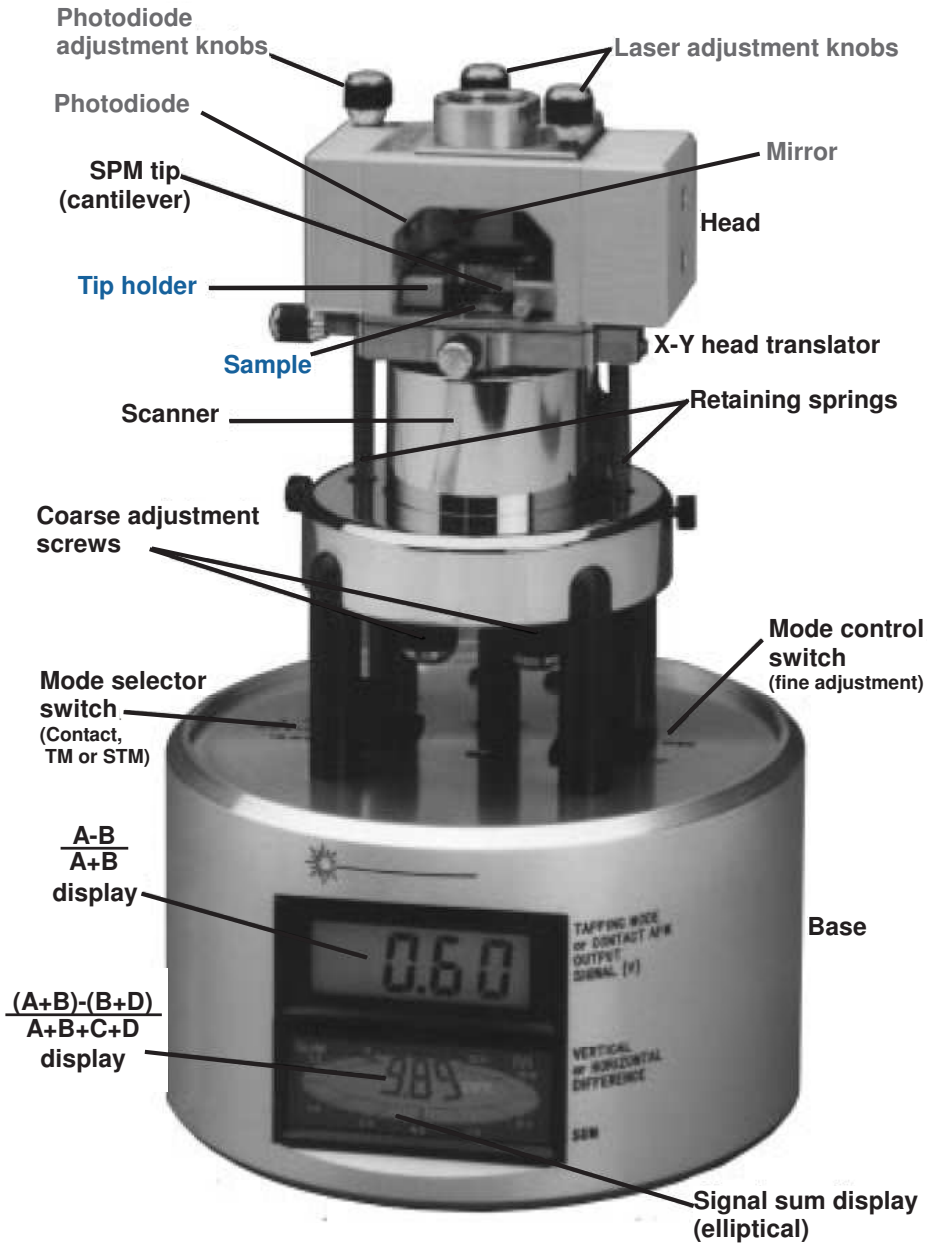

Figure 4.1: Multimode AFM. An example of commercial AFM system by Veeco. The various parts of the system are labeled for reference. *Source: Veeco Multimode Nanoscope III manual*

the system with low forces, which is achieved in part by using a soft cantilever, i.e. low k.

A variety of AFM probes we used in the course of this work were selected to cover a large span of spring constants, compositions, and geometries. In the studies concerning the dynamics of the system in MSAFM, stiffer probes were preferred to obtain a richer spectrum with respect to the modes resulting from the higher level coupling synthesized. However, softer probes are generally better suited to image soft materials such as cells. In the spectroscopy measurements, the surface area and the composition influence the profile and amplitude of the probe signature, which can have a significant impact when imaging complex samples, as will be discussed in Chapter 5.

The resonances in the oscillatory motion of the microcantilevers can be obtained analytically for simpler geometries and computationally otherwise. We computed the eigenfrequencies and eigenmodes of both rectangular and triangular silicon cantilevers used in our work. The results are shown in Fig. 4.4, where the eigenfrequencies are plotted and selected megahertz eigenmodes are displayed for the rectangular (stiff,

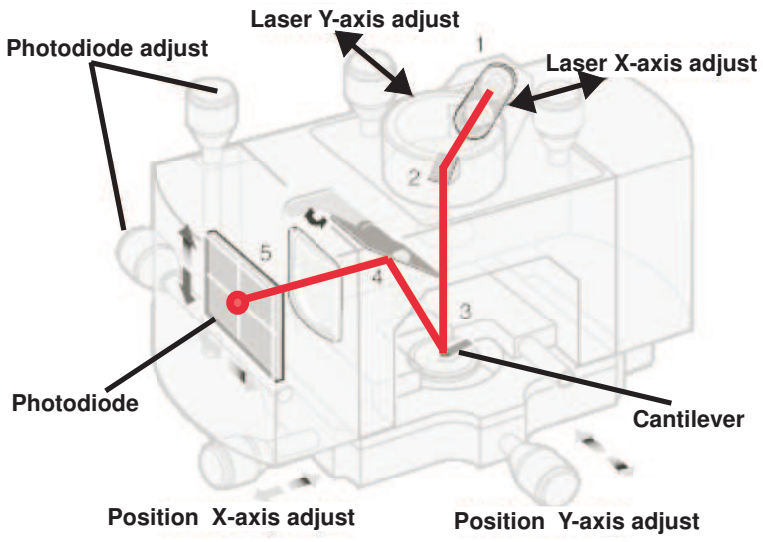

Figure 4.2: Multimode AFM Head. Zoom on the configuration of a AFM head designed and commercialized for a Multimode system. *Source: Veeco Multimode Nanoscope III manual*

$k = 42N/m$, from Olympus, OMCL-AC160 TS-W2) and the triangular (soft, $k = 0.06N/m$, from Veeco Probes, DNP-S) cantilevers. We note that the microcantilever possesses an infinite number $\kappa = 1, 2, \cdots$ of eigenmodes, some of which can resonantly be excited. Thus, by resonance frequency we refer to an actual excited eigenmode of the probe whereas, the off-resonance response of the cantilever is the result of the propagation of the forced oscillations from the (mechanical) actuators, such as piezoelectric bimorphs. In Fig. 2.1, the wavelength of the elastic propagation has been denoted by λ_p, regardless of whether the mode represents the resonance or off-resonance conditions.

The free spectra of the cantilevers used, that is, for a large probe-sample separation

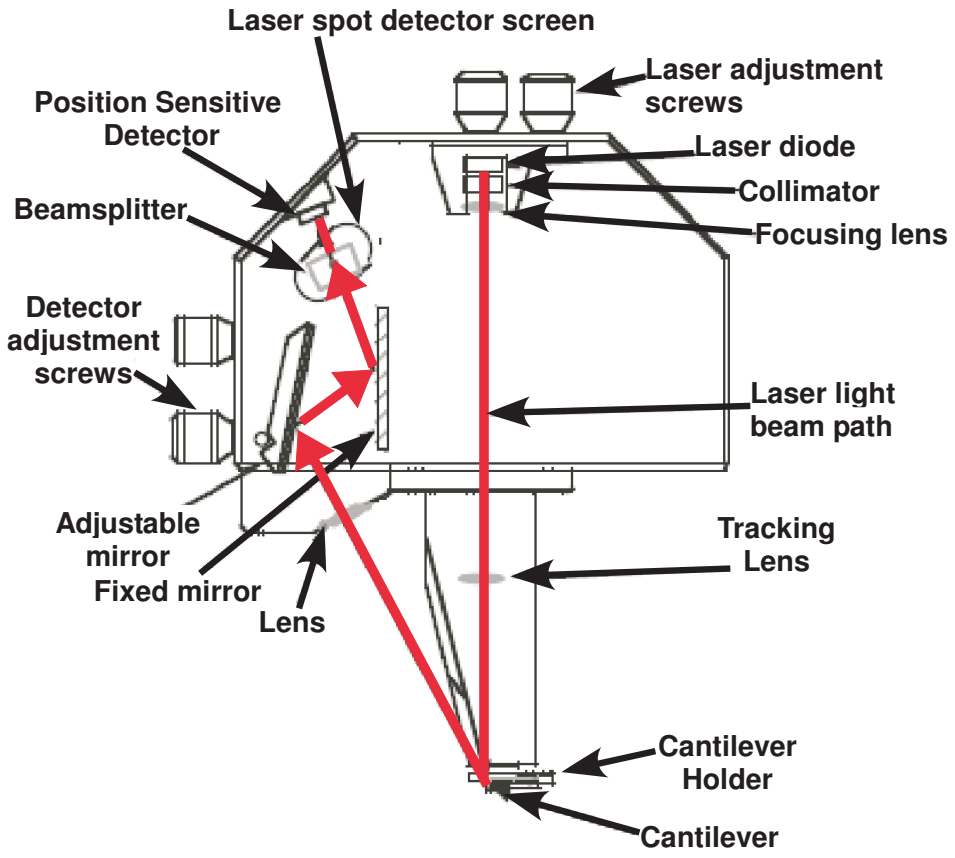

Figure 4.3: Dimension 3100 AFM. An example of commercial AFM system by Veeco. The various parts of the system are labeled for reference. *Source: Veeco Multimode Nanoscope III manual*

$(d = |\bar{r}_L - \bar{r}_s|$ large in Fig. 2.1) and $(a_s, a_p) = (0, 0)$ (both piezoelectric crystals turned off), were found to be $f_p^\kappa = (23, 144, 403, 790, 1307, \cdots)$ kHz for a soft probe with a spring constant $k = 0.06$ N/m, and $f_p^\kappa = (380, 1800, \cdots)$ kHz for a stiff probe with spring constant $k = 42$ N/m in good agreement with the computational results of Fig. 4.4.

4.1.2 Principle of operation of the AFM

Experimentally, using a laser and a position sensitive detector (PSD), the dynamics of the microcantilever is extracted by measuring the instantaneous position of a segment

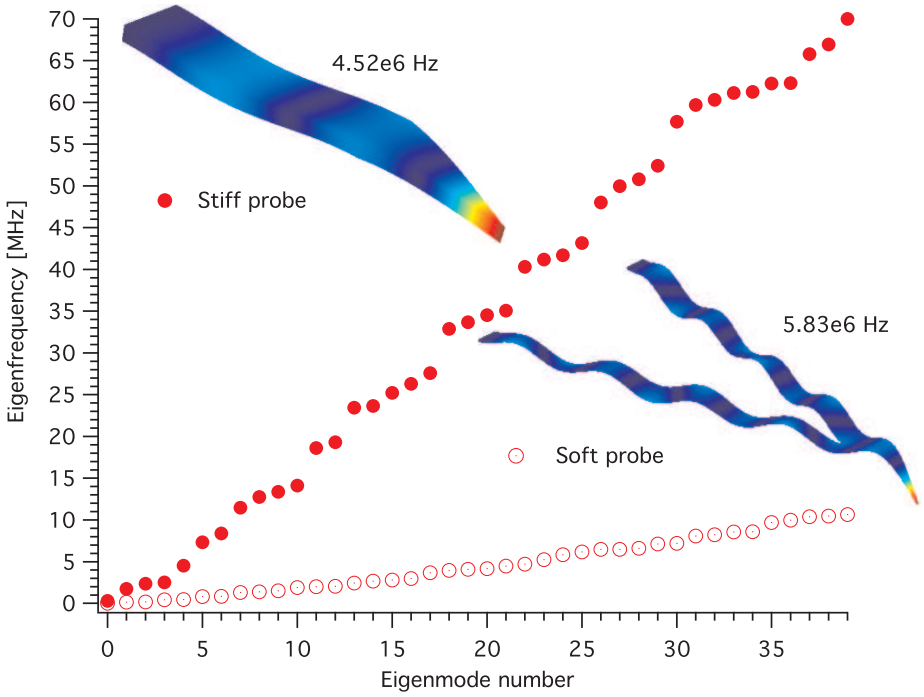

Figure 4.4: Computed eigenfrequencies and eigenmodes of the microcantilevers used. The stiff rectangular probe was 160 μm long, 50 μm wide, and 4.6 μm thick, while the soft triangular cantilever was 180 μm long, 18 μm wide, and 0.6 μm thick. As expected, for the same eigenmode number, the stiff probe exhibits a much faster dynamics. The insets show the computationally determined transversal mode-shapes at selected eigenfrequencies. The color scale restates the deformation state of the probes.

of the cantilever, as denoted by $S(t)$ in Fig. 2.1. From the spectrum of the Brownian motion of the cantilever, or by explicit frequency sweeping of the voltage that drives the piezoelectric bimorph on which the cantilever rests, it can readily be observed [54] that all the eigenmodes κ undergo a "redshift" when d is reduced beyond some threshold (small shift in the case of a stiff cantilever). For the (soft) probe used here, the f_p^1 shifted from 23 kHz to few kHz, while f_p^2 shifted from 130 kHz to 85 kHz, $\cdots$. In our experiments, $\mathcal{C}$ could be measured over the entire frequency range limited only by various bandwidths.

Due to the bandwidth limitation of the PSD ($\approx$ 1 MHz frequency roll-off), an appropriate window for (f_s, f_p) has to be considered so that $S(t)$ will adequately contain information on new mode synthesized in our work.

4.1.3 Elastic coupling

The ultrasonic based AFM [55] is operated using a set of mechanical excitations on the probe, and another set of excitations on the sample. In the first phase of development, the excitations are mechanically induced using piezoelectric bimorphs. The waveform consists of a pure sine wave or the sum of two sine waves. Standard procedures for AFM imaging in contact modes were followed. When the tip and the sample are in contact, the signal S(t) is analyzed with respect to time using an oscilloscope and in Fourier space using a spectrum analyzer. The evolution of each of the modes of the system, corresponding to the peaks observed on the spectrum analyzer, can be monitored using a lock-in amplifier. The amplitude (R) and phase (θ) can then be plotted in the form of a 2D map in the AFM software, for simultaneous comparison to the topography image.

Two piezoelectric (PZT) films (from Physik Instrumente model PIC255) were adapted to accommodate the cantilever probe and the sample. Both films were wirebonded to accept multiple driving waves from the excitation voltage sources (Agilent 33120A). Using a network analyzer (HP PSA Series E444XA), impedance measurements were

carried out to obtain the frequency response of the PZTs and determine their resonances. The resulting specifications for the two crystals are presented in Fig. 4.5. This information is needed for the determination of the total experimental and measurement bandwidth.

4.1.4 Photonic coupling

The measurements presented in this manuscript were targeted for infrared spectroscopy. Infrared light excites the vibrational modes of the chemical bonds of the molecule. At the level of the molecule, the excitation provokes some vibrations of the molecule and generates heat. Cantilever probes can detect these variations. We used two infrared light sources to perform the measurements: a Fourier Transform Infrared Spectrometer for large span of wavelengths, and Quantum Cascade Lasers for single wavelength measurements.

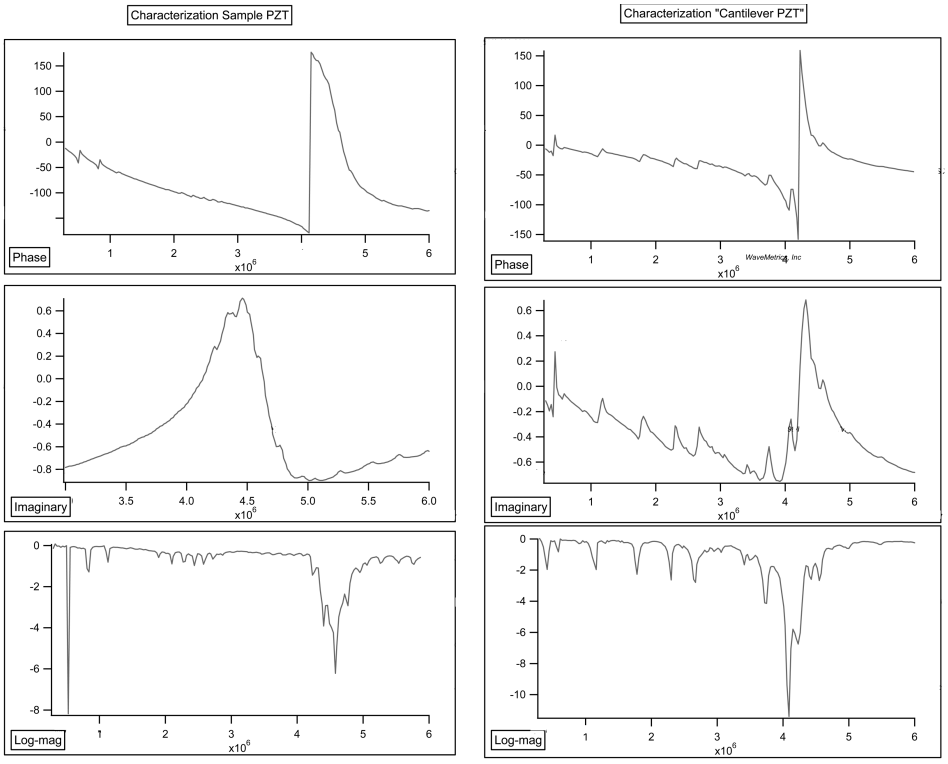

Figure 4.5: Impedance measurements of the piezoelectric bimorphs.

Fourier Transform Infrared Spectrometer

The FTIR measurements were performed using a Perkin Elmer Spectrum GX spectrometer, which was customized to accommodate an external detector. The light is rerouted to the AFM system and focused on the sample of interest, where the cantilever is engaged. In the work presented here, the sample is prepared on a ZnSe substrate, transparent to IR, and the sample is illuminated from the bottom. An optical module, using a succession of aluminum mirrors and ZnSe lenses, was developed in order to focus the light onto the sample. The spectrum of ZnSe crystals is flat between 400-700 cm^{-1}. The size of the focus spot on the sample plate can reach a few millimeters.

The Dimension 3100 AFM from Veeco is well designed to accommodate this type of configuration because the scanner is built-in the AFM head, leaving more flexibility for large sample holders (unlike a Multimode system where the scanner is located directly underneath the sample). The cantilever response is monitored through the optical read-out system, and the PSD sends out a signal S(t) to the controller. Older version of the Nanoscope controller, such as Nanoscope III, require a Signal Access Module (SAM) to access or send various signals in the system. Using the SAM, it is possible to route S(t) to the FTIR spectrometer for signal processing. S(t) resembles an interferogram and its Fourier-transform generates an infrared spectrum of the materials illuminated under the tip of the cantilever.

Quantum Cascade Laser

Quantum cascade lasers have been introduced by Faist et al. in 1994 [21]. The name finds its origin from the phenomenon of electrons "cascading" down several energy levels, emitting a photon at each step of the process. Unlike conventional semiconductor lasers, where the electron-hole recombination across the semiconductor bandgap is the origin of the photon emission, QCLs are based on quantum wells, made of very thin layers of semiconductors, in which the electrons cascade down up

to 100 times, emitting a photon at each step [56, 21]. The QCLs have great potential for spectroscopic applications because of their emission wavelengths in the mid-IR wavelengths (3-25 μm).

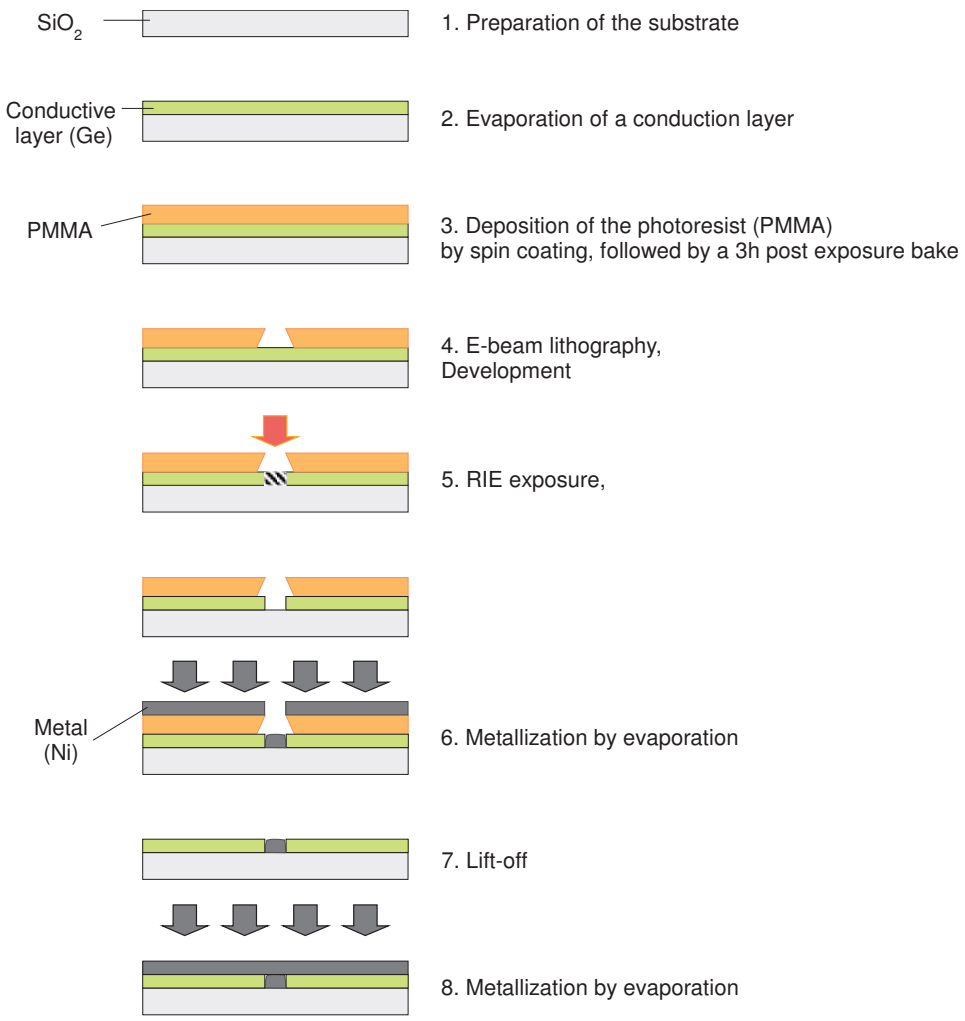

Figure 4.6: Sequence for the nanofabrication of embedded calibration structures for MSAFM.

4.2 Sample design and preparation

4.2.1 Quality control for the semiconductor industry

A nanofabricated sample was designed in order to demonstrate the wealth of new information available with MSAFM. As described in Fig. 4.6, a conductive layer was first deposited (step 2) on the cleaned (step 1) SiO_2 substrate. Photoresist was then spincoated on the sample prior to e-beam lithography (step 3). After a 3 hour soft bake (step 3), by exposure of designed matrices on selected areas, the structures were written on the sample. After development of the photoresist, the exposed photoresist was removed leaving an open site for the nanostructure (step 4). Reactive Ion Etch (RIE) exposure creates a hole in the conductive layer in place of the structures (step 5). Metalization is performed in order to fill the holes, creating the buried part of the structures. After lifting the PMMA off, (in an ideal case) the sample now exhibits a flat surface (step 7). In order to embed the nanostructures a final layer is deposited by evaporation. The images are presented in Fig. 5.16.

A second nanofabricated sample, described in Fig. 4.7, was designed in order to demonstrate further sensitivity of MSAFM. Photoresist was spincoated (step 3) on a clean silicon wafer (step 1) covered of a conductive layer (step2) prior to e-beam lithography. After a 3hours soft bake, various matrices were then exposed onto the

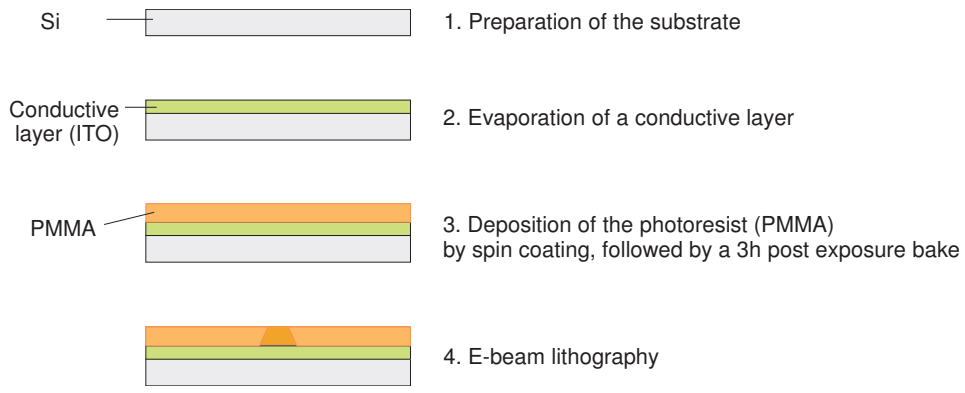

Figure 4.7: Sequence for the nanofabrication of calibration structures for MSAFM.

sample. The samples were not develop nor baked post exposure, but stored in a clean environment until imaging. As seen in (a) the structures are apparent in the topography. Exposure of the PMMA layer by e-beam lithography seems to modify the polymer in such a way that creates deformation of the surface (few nanometers).

4.2.2 Understand biomass at the cell wall level to overcome recalcitrance

The BioEnergy Science Center (BESC) is a partnership between leading teams of researchers across the US, led by Oak Ridge National Laboratory, created to focus on fundamental aspects of the conversion of wood products to biofuel. The main focus of the center is to develop a fundamental understanding of biomass recalcitrance. Recalcitrance is the resistance of the biomass, composed of cellulose, to its breakdown into sugars, which is necessary for biofuel production. A specific task of the project is to develop techniques for the characterization of biomass at the nanoscale.

Populus is a woody plant belonging to *Salicaceae* family [57]. Petiole or the stalk portion of a leaf is the slender stem supporting the blade of a leaf. The samples were chosen due to their importance in the scientific initiative of bioenergy production. Cryotome sections of stem of *Populus* wood was performed at Georgia Institute of Technology using a LEICA CM 3050S cryostat equipped with a disposable steel blade and embedding material (OCT compound, Tissue-TEK) [58]. The thickness of the samples varies from 10 to 50 μm. The cross sections are prepared from fresh samples in both cases. *Populus* samples were stored in a dry environment between two glass slides to prevent distortion and maintain the native form of the samples, then immobilized on a substrate using an adhesive film typically used in SEM. Petiole sections were prepared on glass cover slides, which were then glued on the PZT prior to imaging.

The study will consist of a sequence of samples prepared using various chemical treatments, similar to the treatments involved in biomass processing for biofuel. The goal of this study is to identify the regions of the cell wall structures affected by the

chemical treatment, with high spatial resolution. In addition, the goal is to study to chemical composition at the cell wall level, using the novel infrared AFM technique developed in the project.

4.2.3 Monitor the fate of nanomaterials and their interaction with biological systems - Nanotoxicology

The fate of nanoparticles in biological systems is a problem emerging from the rise of nanotechnologies. The effects of nanomaterials, in particular nanoparticles, are of great concern. However, the number of techniques capable of visualizing local populations of nanoparticles *in situ*, with nanometer resolution, is limited. In our study, we take advantage of the great potential of MSAFM for subsurface imaging, and demonstrate that it is indeed possible to detect embedded nanoparticles within a cell. The study involved exposing mice to nanoparticles and study the effects 24 hours and 7 days post-exposure.

Single-walled carbon nanohorns (SWCNH).

Belonging to the fullerene group of carbon allotropes, the Dahlia-like SWCNH discovered recently by Iijima et al. are particularly attractive as potential intracellular delivery vehicle [59]. In our investigations, SWCNH were produced in a high temperature laser ablation system using a Nd:YAG laser (600W maximum average power). Since SWCNH are not soluble in phosphate buffered saline (PBS), the nonionic surfactant pluronic acid F-127 (Molecular Probes) was added to suspend the particles. The aggregation tendency of SWCNH was attenuated. A $1\mu g/\mu L$ solution of SWCNH was soluble in PBS with 1% pluronic. Pluronic-coated SWCNH (diluted to $0.1\mu g/\mu L$ in PBS with 1% pluronic) alone were imaged with an AFM in contact mode in order to acquire topographic information for recognition purposes in bronchoalveolar lavage (BAL) samples. Nanohorns were imaged using AFM by placing vigorously vortexed drop on freshly cleaved mica and air-drying prior to

imaging. As a control, 1% pluronic in PBS was also analyzed. All mica substrates were treated with a 1.2% solution of MgCl in order to neutralize the negative charge before adding the samples. The solution of SWCNH suspended in PBS and pluronic was used to acquire the Raman spectra presented in Chapter 5. It was found that the carbon nanohorns assemble into spheres approximately 100 nm in diameter which is consistent with previous studies that reported spherical masses with individual nanohorn projections around the periphery, creating a dahlia-like structure.

Animals and Experimental Design.

Each mouse was exposed to 30 μg of SWCNH, an amount estimated to approximate OSHA-permissible exposure limits for graphite particles across twenty 8-hour work-days [60]. Agglomeration of the SWCNH within the aspiration media (PBS) was controlled using the non-ionic surfactant pluronic F-127 and sonicating the solution prior to dosing, allowing the evaluation of the uptake of nanoparticles rather than larger agglomerates. Control and SWCNH-exposed mice were sacrificed 24 hours and 7 days post-exposure. Adult male mice from the stocks maintained at ORNL were used in study. All mice were housed in the specific pathogen-free facility at ORNL and given water and standard rodent chow *ad libitum*. The Animal Care and Use Committee at ORNL approved all experimental procedures. The mice were randomly assigned to two experimental groups: (1) 1% Pluronic/PBS aspiration group and (2) 1 μg/μL SWCNH in 1% Pluronic/PBS aspiration group. Prior to exposure, the SWCNH solution was sonicated to ensure dispersion of the particles. Three mice from each group were sacrificed 24 hours and 7 days after aspiration. Mouse pharyngeal aspiration was used for carbon nanohorn administration. Aspiration has been shown to consistently deliver particles to the alveolar region of the lung [61]. Aspiration was chosen because it is less traumatic and invasive than instillation, and is technically easier than inhalation. Aspiration was performed as previously described [60]. Briefly, mice were anesthetized with isoflurane and hung by their incisors on an inclined board. The animal's tongue was extended using forceps, and 30 μL of the control solution

or SWCNH solution was placed on the back of the tongue. The tongue was extended until all of the fluid was aspirated into the lungs.

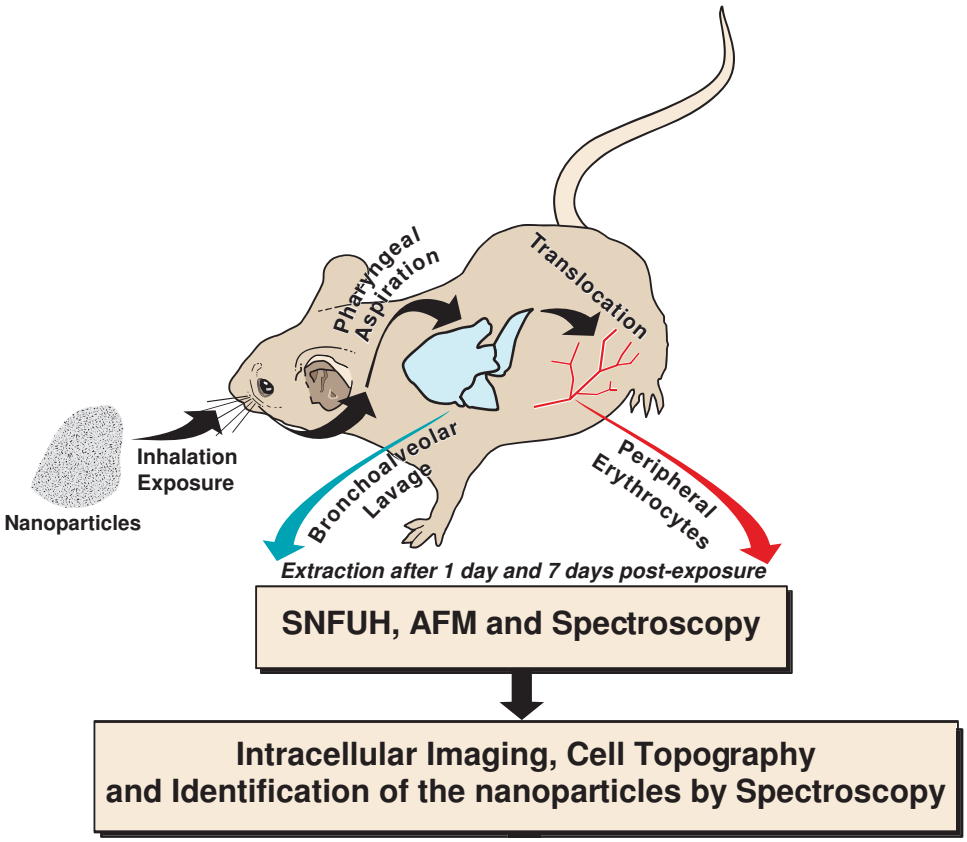

Figure 4.8: Protocol for the mice exposure to SWCNHs. Each mouse was exposed to 30 μg of SWCNH. Control and SWCNH-exposed mice were sacrificed 24 hours and 7 days post-exposure. Mouse pharyngeal aspiration was used for carbon nanohorn administration. Mice were sacrificed by isoflurane overdose in a bell jar, and BAL was performed according to standard protocols.For light microscopy analysis, cytospin slides were stained with a Hema3 kit (Fisher Scientific). For AFM analysis, cells were centrifuged onto freshly cleaved mica using a cytospin and fixed with methanol. In addition, peripheral blood was collected using heparinized capillaries from the abdominal aorta. Blood samples were diluted in PBS, centrifuged onto freshly cleaved mica using a cytospin, and fixed with methanol.

Sample Preparation.

Mice were sacrificed by isoflurane overdose in a bell jar, and BAL was performed according to standard protocols. Briefly, the trachea was exposed and a blunt 22-gauge needle inserted into the trachea. After securing the needle with sutures, lavage was performed five times with cold sterile PBS. Fluid was gently aspirated while massaging the chest. The first lavage was performed with 0.6 ml of PBS and was kept separate for analysis for another study. The second and third lavages were performed with 1.0 ml of PBS and were pooled in sterile tubes, centrifuged, and resuspended in PBS. For light microscopy analysis, cytospin slides were stained with a Hema3 kit (Fisher Scientific). For AFM analysis, cells were centrifuged onto freshly cleaved mica using a cytospin and fixed with methanol. In addition, peripheral blood was collected using heparinized capillaries from the abdominal aorta. Blood samples were diluted in PBS, centrifuged onto freshly cleaved mica using a cytospin, and fixed with methanol.

Chapter 5

Analysis and Discussions

5.1 Mode Synthesizing Atomic Force Microscopy (MSAFM)

Increasing the dynamic attributes of the probe of an AFM that permits simultaneous acquisition of manifold nanoscale information holds great potential in nanosciences [62, 63, 15]. In dynamic AFM [15], a silicon microcantilever, a mechanical oscillator with frequency f_p, interacts with a surface of interest via a van der Waals potential (often with contributions from other interactions such as thermomolecular, electrostatic, Casimir, $\cdots$) prevailing in the nanometer interfacial region between the surface $\bar{r}_s$ and the cantilever probe tip $\bar{r}_L$, as partially shown in Fig. 5.1. One may also consider the (sample) surface to constitute a second mechanical oscillator, with a frequency f_s, as a result of a possible forcing on the sample exerted by a piezoelectric material's ultrasonic vibrations at the contact interface, also depicted in Fig. 5.1. We show that such a boost in information dimensionality can be accomplished via a diversification of the frequency content of a force probe. Retrofitting an AFM, we introduce the concept of mode synthesizing atomic force microscopy MSAFM by presenting the experimental manifestation of a local mechanical probe-sample coupling that facilitates sensitive amplitude and phase mapping of nanoscale material

features. It is shown that such a coupling is not unique in the excitation parameter space of the system but forms bands that occupy several megahertz of available frequencies. A rich spectrum of first- and higher-order couplings is discovered, opening up for new modalities of force microscopy [55, 64].

5.1.1 An hydrogen atom-like system

Here, we introduce the concept of MSAFM [55, 64], and show that signal transduction and image formation can occur in an expanded frequency space by utilizing a multiple-order coupling, symbolically denoted by $\mathcal{C}$, which is solely induced by the nonlinear probe-surface interaction. We then show that $\mathcal{C}$, provided by the

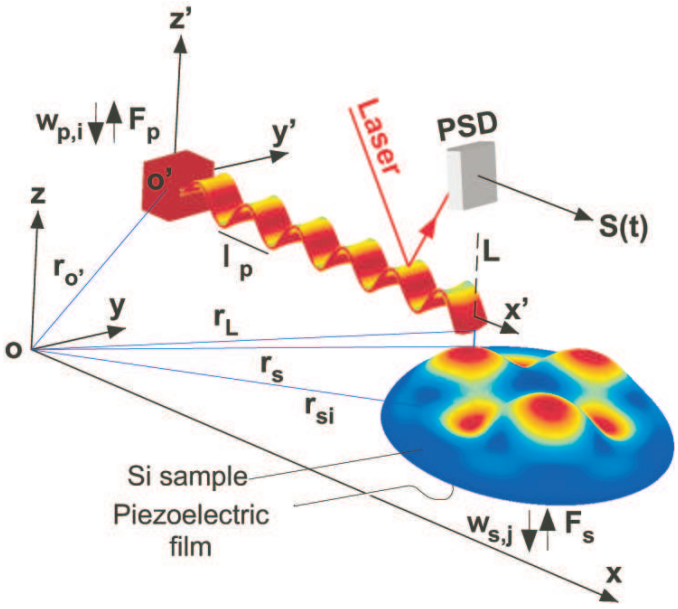

Figure 5.1: Computed eigenmodes of a silicon microcantilever and a silicon sample. The left boundary of the cantilever probe (length L) is fixed with respect to the origin $\bar{r}_{o'}$ of the accelerated reference frame $o'x'y'$, but oscillates with respect to the inertial reference frame oxy. The probe and the sample are driven by piezoelectric films exerting forces F_p, and F_s, respectively. The motion of the sample at $\bar{r}_s$ is measured with respect to oxy. A laser and a position sensitive detector (PSD) represent the dynamics of the system in time domain by $S(t)$. An embedded inhomogeneity at $\bar{r}_{si}$ modifies the dynamics of $\bar{r}_s$ affecting the signal $S(t)$ through the coupling $\mathcal{C}$. The wavelength of the high frequency ω_p oscillations of the cantilever is denoted by λ_p [55].

much faster (than the excitation time scales) interfacial electronic interactions, allows synthesis of a multitude of new operational modes, or $\mathcal{C}$-modes, limited only by the system and measurement bandwidth. The vast dynamic landscape of $\mathcal{C}$ renders MSAFM to be drastically different than existing modalities.

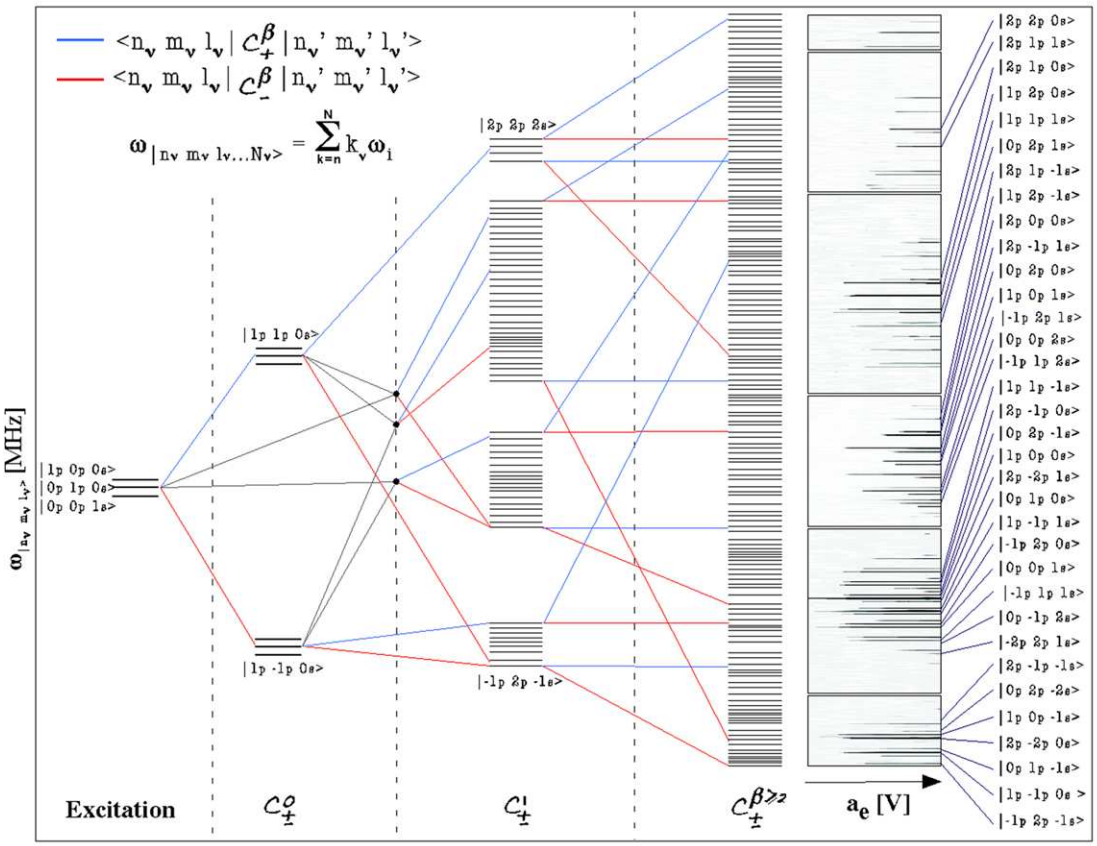

Figure 5.2: Multiple orders coupling in frequency space during MSAFM. This 3-stimuli diagram represents all the dynamic states created by $\mathcal{C}$.The three excitations (two for the probe and one for the sample) listed in the first column, the initial states of the system, are mixed by $\mathcal{C}$ to theoretically generate 6 new states by the first order coupling $\mathcal{C}^0$, 62 states for the second order coupling $\mathcal{C}^1$, and so on. A spectral contour plot of the measured $a_{|nml>}$ (with $n, m, l = -2, -1, \cdots, 1, 2$) with $a_{|001_s>} = a_{|01_p0>} = a_{|1_p00>} = a_e$ containing 34 selected states, which can all be used simultaneously for imaging is presented in the last column [55].

In order to systematically describe the synthesized modes, we may, somewhat metaphorically, resort to an atomic analogue for the coupled system and invoke a Dirac-like notation. For example, in a hydrogen atom, the electron and the nucleus constituting the two oscillators, interact via a Coulomb potential to generate the discrete quantum states $|nlm>$. In the case of MSAFM, the probe and the sample constituting the two oscillators, interact via a van der Waals potential to generate the well-defined states $|n_\nu m_\nu l_\nu \cdots>$. Thus , a Groterian-like diagram may be constructed to graphically represent the observed states. A formal diagram can be constructed for any number of input stimuli and output synthesized $\mathcal{C}$-modes. MSAFM is founded upon exerting a multi-harmonic forcing $F_s = \sum_j a_{s,j} \sin(2\pi f_{s,j} t + \varphi_{s,j})$ on the substrate, and another $F_p = \sum_i a_{p,i} \sin(2\pi f_{p,i} t + \varphi_{p,i})$ on the probe, such that when the probe-sample separation d $(= |\bar{r}_L - \bar{r}_s|)$ is reduced beyond a threshold, the nonlinear probe-sample interaction $\mathcal{C} \neq 0$ creates a time domain signal $S(t)$ that represents the dynamic state of the probe, as annotated in Fig. 5.1. Then assigning a series of integers $n, m, l, \cdots = 0, \pm 1, \pm 2, \cdots$, and an index $\nu = s, p$, where s and p refer to the sample, and the probe, we define $|n_\nu m_\nu l_\nu, \cdots>$ to be a state with a frequency $\omega_{|n_\nu m_\nu l_\nu, \cdots>} = n_\nu \omega_1 + m_\nu \omega_2 + l_\nu \omega_3 + \cdots$ and an amplitude $a_{|n_\nu m_\nu l_\nu, \cdots>}$. The number of excitation states determine the number of integers $(n_\nu, m_\nu, l_\nu \cdots)$, which will populate the state $|s>$. For example, in Fig. 5.2, we consider three excitation states and the notation will take the form $|s>= |n_\nu m_\nu l_\nu>$. In Fig. 5.3 and Fig. 5.18, the measurements presented result from exciting the system with two driving frequencies, in which case $|s>= |n_\nu m_\nu>$. Now, representing each Fourier component of S, symbolically as $|n_\nu m_\nu l_\nu \cdots>$, MSAFM utilizes the amplitude and phase of $S(t)$, by simultaneously locking onto the frequency of any given number of $\mathcal{C}$-modes, that is, $\omega_{|n_\nu m_\nu l_\nu \cdots>}$. We note that $\mathcal{C} \to 0$, in the limit of large d, and each oscillator will possess a spectrum originating from its own driving frequency tuning, that is, ω_s^q and ω_p^κ, $q = \kappa = 1, 2, \cdots, \infty$.

In order for our notation to be coherent, excitation states should be used to represent the driving signal with the same symbolism. In Table 5.1, we present the notation in

the case of two excitations (first when the cantilever and the probe are excited and second when the probe only is excited by two different driving frequencies) and three excitations of the system. The same procedure applies for higher order couplings. For example the first order nonlinear coupling between $|01_p>$ and $|1_s0>$ will create two states, and we can describe it in these terms : $<1_s0|\mathcal{C}_+^\beta|01_p>=|1_s1_p>$ for the sum and $<1_s0|\mathcal{C}_-^\beta|01_p>=|-1_s1_p>$ for the difference. Juxtaposition of the modes in the proposed Groterian-resembling diagram, in fact surpasses a simple storing utility. The diagram clearly keeps track of whether a given mode is a result of a summation or subtraction, and whether the mode is a result of a first coupling or a higher order coupling. In addition it also includes the information about the origin of the excitation ($\nu = p$ for probe, s for sample). Furthermore, the modes are vertically dispersed according to their frequency.

Table 5.1: Excitation modes expressed in the MSAFM notation.

Number of excitations	Frequency	Operation	Notation
2	ω_p	$0*\omega_s+1*\omega_p$	$\|01_p>$
	ω_s	$1*\omega_s+0*\omega_p$	$\|1_s0>$
2	ω_{1p}	$1*\omega_{1p}+0*\omega_{2p}$	$\|1_p0>$
	ω_{2p}	$0*\omega_{1p}+1*\omega_{2p}$	$\|01_p>$
3	ω_{1p}	$1*\omega_{1p}+0*\omega_{2p}+0*\omega_s$	$\|1_p00>$
	ω_{2p}	$0*\omega_{1p}+1*\omega_{2p}+0*\omega_s$	$\|01_p0>$
	ω_s	$0*\omega_{1p}+0*\omega_{2p}+1*\omega_s$	$\|001_s>$

For example, when $i = 1, 2$ and $j = 1$ in F_p and F_s, a striking 62 $\mathcal{C}^1$-modes are predicted as mapped in Fig. 5.2. Here, a selected 34 experimentally measured $\mathcal{C}^1$-modes are shown, for which the contour plots in the fifth column collectively represent the measured amplitudes $a_{|n_\nu m_\nu l_\nu>}$ as a function of the amplitude of the excitations. The first order coupling $\mathcal{C}^0$, mixes the three excitation modes $|001_s>$,$|01_p0>$ and $|1_p00>$ to give rise to 6 modes via sum and difference generation, whereas the second order coupling $\mathcal{C}^1$ mixes the previous modes to create the 62 modes by further sum and difference generation. Thus, the coupling may be viewed upon as an operator

reinforced as $\mathcal{C}_{\pm}^{\beta}$ to signify the order β and sum/difference operation performed on the states $|n_\nu m_\nu l_\nu, \cdots >$, as annotated in Fig. 5.2. Consequently, $\mathcal{C}$ may be envisioned as being analogous to the susceptibility χ in nonlinear optics albeit the role of a material nonlinear polarizability is played by the nonlinear interfacial forces in MSAFM.

In light of the self-coupling $\mathcal{C}_p$, one may envision extending the parameter space of the entire system by also mechanically exciting the sample with a series of harmonic elastic waves of various frequencies. In such an event, one may symbolically define a total coupling $\mathcal{C} = \mathcal{C}_p + \mathcal{C}_{ps}$, where $\mathcal{C}_{ps}$ represents the probe-sample coupling discussed previously. To form $\mathcal{C}$, a minimum of two excitation parameters is required. For the same parameters (a_p, a_s) and (f_p, f_s), a host of $\mathcal{C}$-modes is synthesized by higher order couplings that can be detected at frequencies $\omega_{|n_\nu m_\nu l_\nu>}$. However, this is not unique and an extended criterion can be established for detection at $\omega_{|n_\nu m_\nu l_\nu \cdots>}$ corresponding to an arbitrary number of stimuli. Thus, in the multidimensional parameter space of MSAFM, $\mathcal{C}$-modes can be designed by a purposeful arrangement of the input stimuli [55, 64].

5.1.2 Nonlinear interactions in MSAFM

The parameter dependencies of $\mathcal{C}$ may be unveiled, for example for the simplest case of $i = j = 1$, by studying $\mathcal{C} = \mathcal{C}(f_{p,1}, f_{s,1}, a_{p,1}, a_{s,1}, d)$. For fixed $a_{p,1} = a_{s,1}$, the experimental measurements are shown in Fig. 5.3 for the spectral and amplitude dependencies of the selected $\mathcal{C}$-modes $|n\ m >= |-1_s\ 1_p >$ (a), $|1_s\ 1_p >$ (b), $|2_s\ -1_p >$ (c), and $|-1_s\ 2_p >$ (d). The observed bands correspond to $\omega_{|nm>} = \omega_p^\kappa$, with the values corresponding to the first few κ annotated. The vertical lines formed in Fig. 5.3 are indicative of a maximum in the displacement of the cantilever at any of the $\omega_{|nm>}$ when the driving frequency applied to the cantilever corresponds to one of the ω_p^κ.

In Fig. 5.4, the observation that the strongest coupling (phase and/or amplitude) is obtained when the probe is retracted from its original collapse point to the surface (before the probe ‘ ‘jumps out of contact”), that is, $\mathcal{C} = \mathcal{C}_{max}$ when $d = |\bar{r}_L - \bar{r}_s| > \delta$,

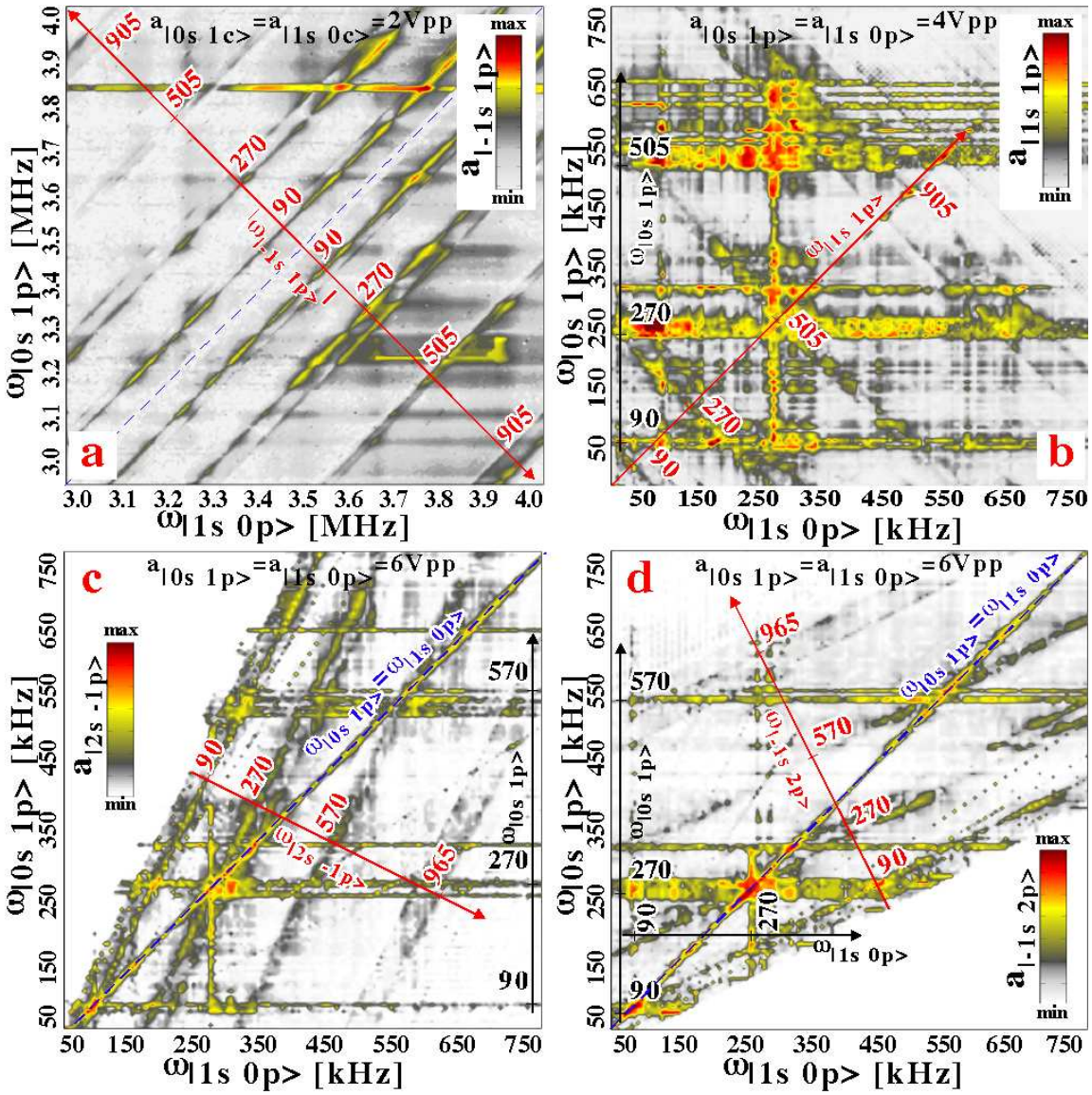

Figure 5.3: Parameter dependence of selected $\mathcal{C}$-modes. (a) The variation of the amplitude of the $\mathcal{C}^0$-mode $|-1_s1_p>$ in the higher frequency excitation. (b) Lower frequency amplitude dependence of the $\mathcal{C}^0$-mode $|1_s1_p>$ at higher excitation amplitudes. (c,d) Dependence of selected $\mathcal{C}^1$-modes upon the excitation frequency at higher excitation amplitudes. In all, red and black axes mark the occurrence of ω_p^κ, while the blue axis demarcate the equality of excitation frequencies. The excitation amplitudes are annotated on the top portion and a scale bar is provided to categorize the contour levels. The exhibited bands can be identified to correspond to (in-contact) ω_p^κ, $\kappa = 1, 2, \cdots$ [55].

where δ is the distance of closest approach, implies that both attractive and repulsive forces participate in forming $\mathcal{C}$. The anticipation of the presence of $|1_\nu 1_\nu >$ was based on the assumption that, it is the nonlinear nanoscale interfacial forces that gives rise to $\mathcal{C}$ and thus to $|-1_\nu 1_\nu >$. Thus, in analogy with nonlinear optics using nonlinear crystal materials to generate sum and difference frequencies [65], we have established a nanomechanical sum and difference generation not based on nonlinear material but nonlinear interaction. Therefore, the oscillation of the probe is essential in the formation of $\mathcal{C}$, in lack of which no other interference effects due to sample excitation alone may simply be picked up by the probe. To truly establish that the mechanical wave-mixing is a result of the nonlinear interfacial forces, and thus exclude any potential interference from the sample, we maintained a stationary sample, but imposed, on the piezobimorph on which the cantilever was mounted, two independent high frequency voltages. Then analyzing $S(t)$ in Fourier domain, for large d, yields only two distinct peaks corresponding to the off-resonance forced oscillations of the cantilever. However, a striking wave mixing can be observed when d is made

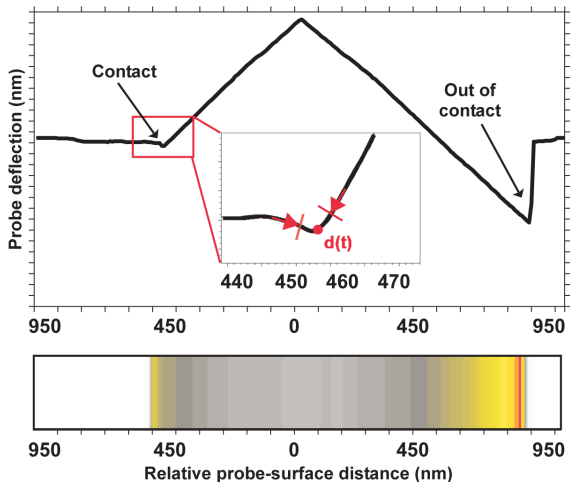

Figure 5.4: Behavior of nanomechanical frequency difference generation. Experimental measurement of the distance dependence of the force obtained for the amplitude of oscillation at the difference frequency exhibited by MSAFM, as a function of the form of d, the distance between the tip of the cantilever and the surface of the sample. The contour plot represents the strength of the signal, white being the lowest amplitude, red the strongest.

sufficiently small for the probe tip to engage in the nonlinear interaction with the sample surface. Thus the surface interaction induces a self-coupling $\mathcal{C}_p$ that mixes the elastic waves to generate additional oscillations at the sum and difference frequencies, which in view of the order β can extend beyond several megahertz. These new modes are fully functional and can be used to provide unique image formation. Again, the image formation is superior when the generated $\mathcal{C}_p$ mode frequencies are tuned to coincide with an in-contact resonance frequency of the cantilever, $\omega_p^\kappa, \kappa = 1, 2, \cdots$. Furthermore, we observe no formal limitation on the number of imposed driving signals.

The cantilever probe motion as a function of time was isolated and examined. Time traces of the motion of the cantilever, the detected signal S(t), is represented in Fig. 5.5. The first case is a free cantilever, shown in Fig. 5.5 (top), and the second case is where the distance between the probe and the substrate is sufficiently small to generate the nonlinearities in the system, shown in Fig. 5.5 (bottom). The direct comparison of the traces demonstrates the modulation attributed to the nonlinear coupling between the probe and the sample. The traces presented were recorded at a fixed tip-sample distance. The strength of the coupling, that is, the emergence of the peak at $| -1_s \; 1_p >$, is directly dependent on the driving amplitudes of both piezoelectric crystals.

5.1.3 Subsurface scattering and imaging using MSAFM

The underlying mechanism of subsurface scavenging of information in the context of force microscopy has not yet been described. MSAFM relies on the $\mathcal{C}$-modes to acquire subsurface information. Using elastic excitation and therefore initially an "acoustic probe" to sense the interior of the sample. The variation in the $\mathcal{C}$-modes will then register the embedded inhomogeneities. In a hypothetical measurement scenario, in principle, using the same $\mathcal{C}$-modes, one could measure the presence of any (thought) nanoparticles within the material domain of the cantilever probe via

the detection of an induced perturbation. However, in this *gedanken* experiment, one would need to be able to detect the local oscillation of the sample surface, near the contact point, with a comparable sensitivity to that of the cantilever. In an attempt to computationally visualize the subsurface elastic perturbation induced by embedded nanoparticles that would give rise to a detectable surface manifestation altering the contact point dynamics (and thus altering the $\mathcal{C}$-modes attributes), we solved for

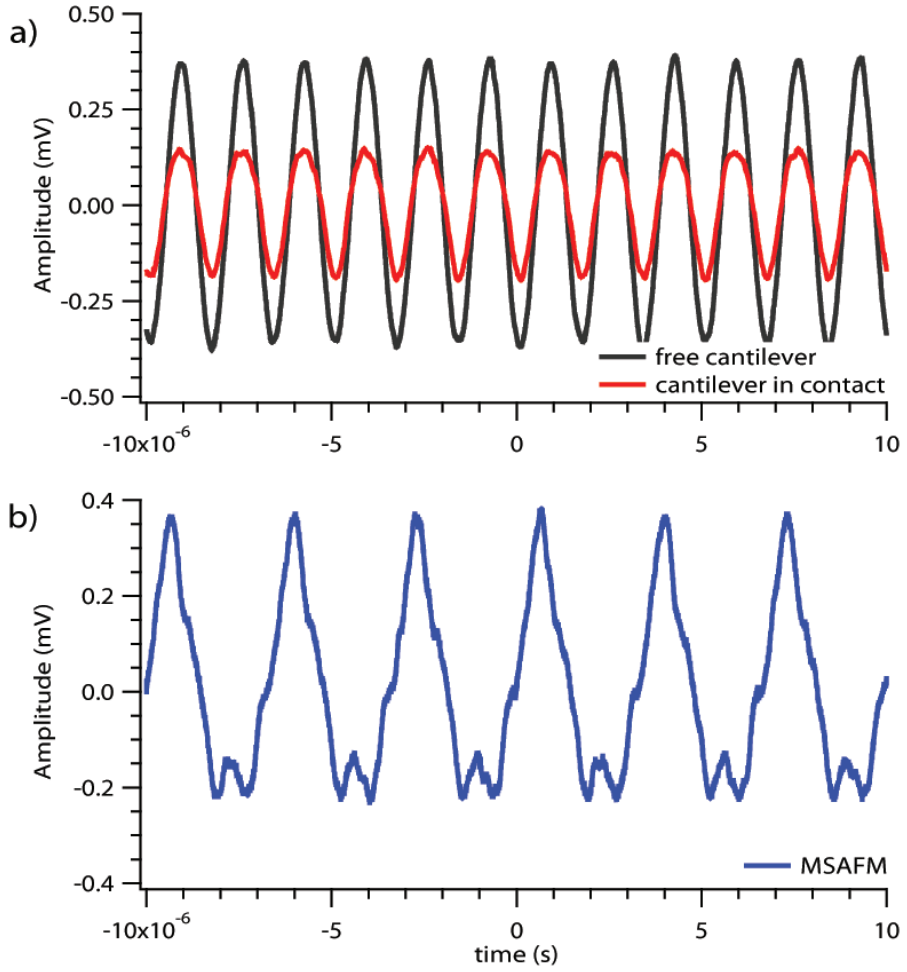

Figure 5.5: Time traces representing the motion of the cantilever. (top) The cantilever is free and two mechanical forcings are applied to the base of the probe. (bottom) The cantilever is in contact with the surface of the sample. The amplitude of the motion of the cantilever is modulated as a consequence of the nonlinear coupling between the probe and the surface of the sample.

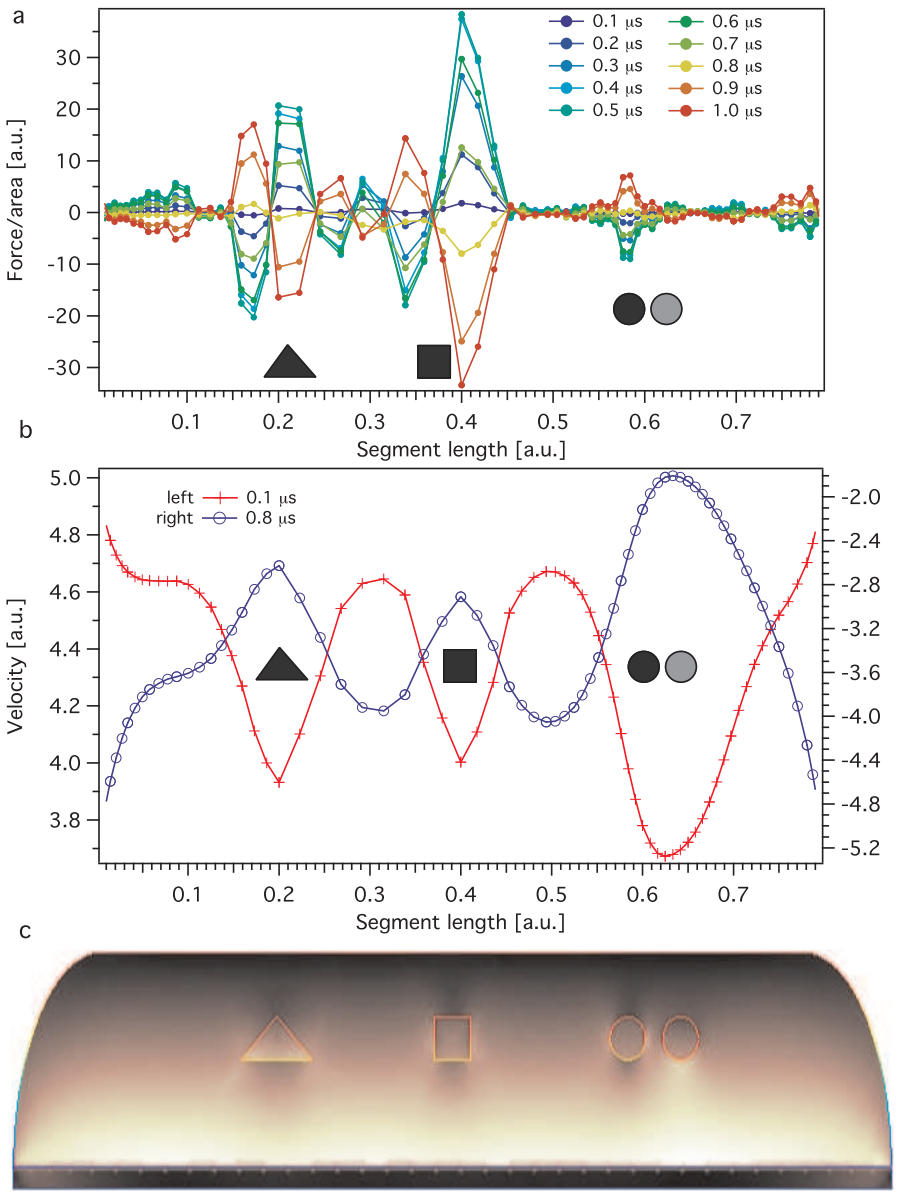

Figure 5.6: Computational subsurface detection of embedded inhomogeneities. (a) Surface traction, and (b) surface velocity measured at a segment of the top boundary of the surface in (c) where a cell-like silicon disc containing nanoparticles of three different geometries, and two different materials (for the two circular particles) is elastically excited from the bottom layer. The surface color scheme represents the strain energy density, and the color of the boundary of the disc and the particles indicate the total displacement of the material. [55]

the surface stress, surface velocity, deformation, and strain energy density of a cell-shaped silicon medium that has various shaped embedded material inhomogeneities. The results, shown in Fig. 5.6, clearly indicate that the loci of the embedded structures can engendered at the top surface of the embedding structure.

5.2 Photonic coupling - A step forward towards high resolution chemical identification

Outlining some of the advantages of cantilever shaped microstructures, we study the spectral response of these mechanical oscillators. Microcantilevers can be mass-produced, are cost effective, and can be integrated in miniaturized systems. Due to their small sizes, large surface-to-volume ratio, and the availability of materials with various elastic parameters, cantilevers exhibit a very high sensitivity to external stimuli and also readily self-excite into measurable resonances by the ambient stochastic processes [66]. In particular, photon scattering provides a channel to affect the mechanical state of the structure. The small active area of the micro- and nano-cantilevers provides excellent spatial resolution which, for the appropriate part of the infrared spectrum, can be considered to be at the sub-wavelength scale. An important benefit of using microcantilevers as detectors to complement spectroscopy is that much smaller samples down to nanogram quantities can be detected or analyzed in comparison with the milligram amounts needed for standard methods [67]. The absorption properties of the various molecules of the probe-sample system, as a result of their interaction with electromagnetic radiation [68, 69, 67], are directly related to their vibrational modes in the case of wavelength in the infrared range. The unique response of individual chemical bonds combine to form a complex and unique signature of the system with the possibility of dynamical measurements in time. Here the response of the cantilever itself without the sample material is used as a background to the FTIR spectra as illustrated in Fig. 5.7. In this study, scanning

the optical path difference results in recording an interferogram corresponding to the thermal response of the microcantilever probe in time. Given that the probe can respond to the fast changes in thermal responses of the sample material, it is then possible to resolve the absorption bands of the material under investigation. The experiments were conducted using coated cantilevers with a total thickness in the range 0.55-1.3 μm. These probes were used due to their availability and good absorption characteristics in spectral range 7800-400 cm^{-1}.

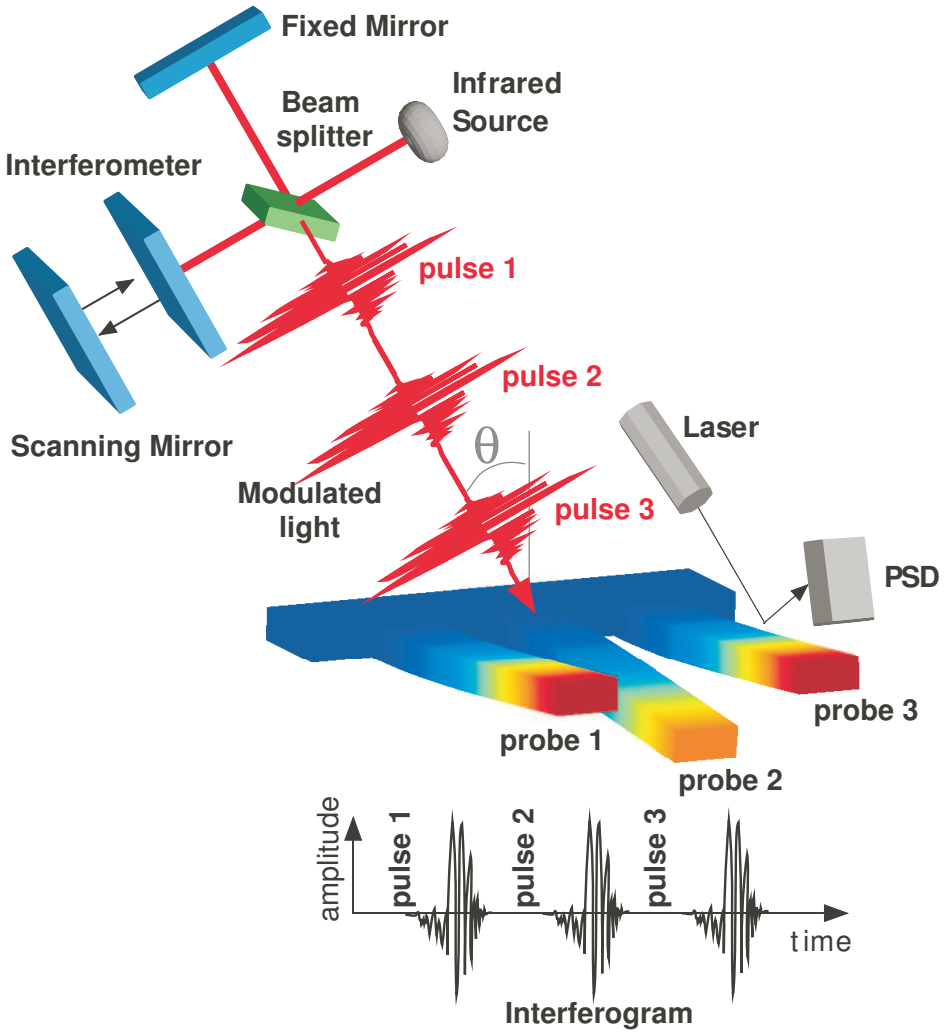

Figure 5.7: The setup. Schematic representation of the experimental setup used for spectroscopic measurements. The IR beam of light is focused onto the microcantilever to generate the interferogram.

The new "thermal signal" prepared for the spectrometer input was evaluated by adjusting the operating parameters of the spectrometer, as shown in Fig. 5.8 and Fig. 5.9. Spectra of a clean microcantilever coated with Al was analyzed as the scanning velocity and resolution were systematically varied. Resolutions of 4 cm^{-1}

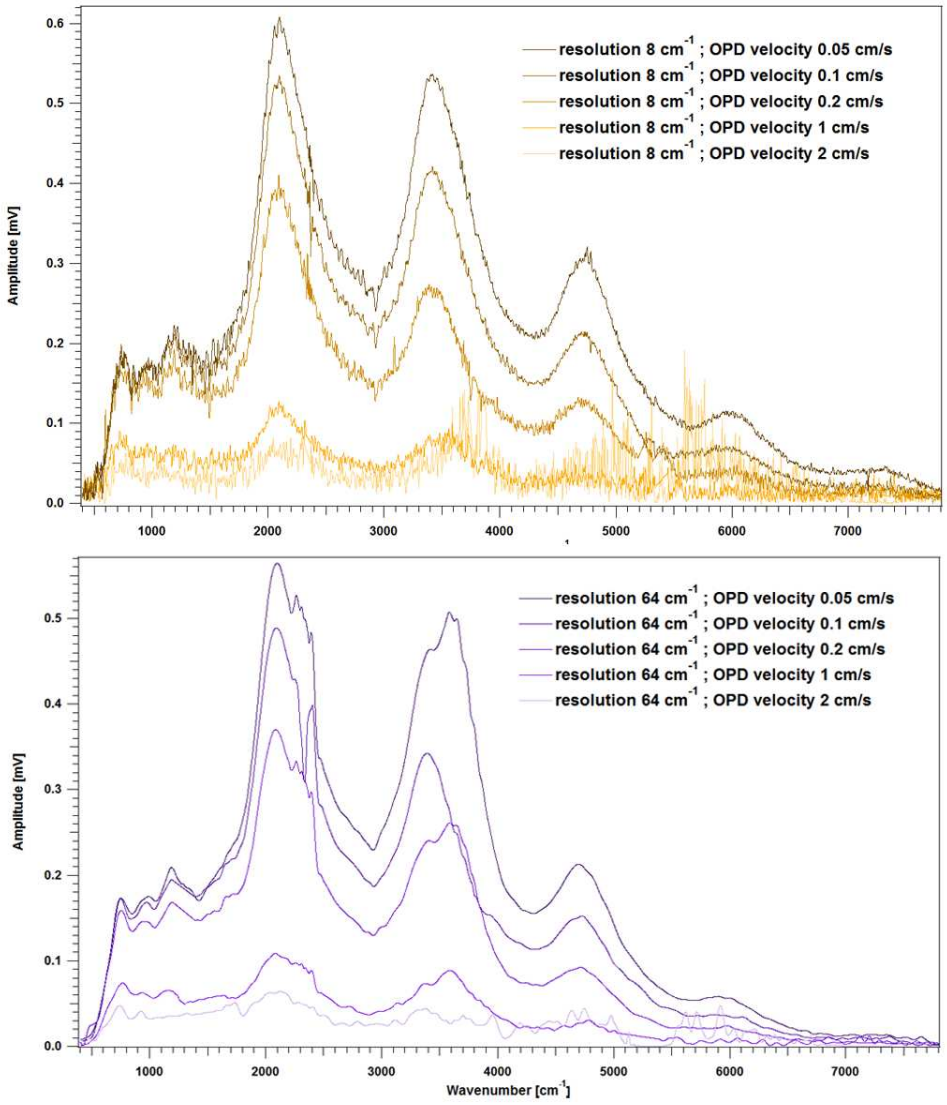

Figure 5.8: Effect of OPD velocity on the cantilever response. The response of the microcantilever spectra to variations in the scanning parameters (7800 cm^{-1} to 400 cm^{-1}). The results are presented when the resolution of the spectrometer was set to 8 cm^{-1} and 64 $cm^{-1}$with the velocity of displacement of the mirror varying from 0.05 to 2 $cm.s^{-1}$. A soft rectangular microcantilever (f_0=11 kHz) made of silicon (1 μm thick) and coated with aluminum (30 nm thick) was used.

and 8 cm^{-1} at velocities of 0.05 cms^{-1} and 0.1 cms^{-1} were determined to be the best operating parameters. The resulting spectra are consistent with the spectra of silicon and aluminum. The influence of the surface area, associated with the dimension, in the response of the MEMS system to infrared illumination is presented in Fig. 5.10. The spectra of two Al coated silicon microcantilevers with two different lengths (300 and 350 μm) exhibit a noticable difference in the amplitude of the signal. The band of absorption remains the same because of the similar composition of the probes. The material chosen to design the mechanical oscillators are of tremendous importance, as can be seen in Fig. 5.11. Note that a strong absorption band in the spectrum of the cantilever, used as a dectector here, might engender loss of sensitivity when investigating a material with absorption in the same region of the spectrum. Indeed the absorption of energy by the mechanical oscillator can potentially saturate the system and prevent its response as a detector for this region.

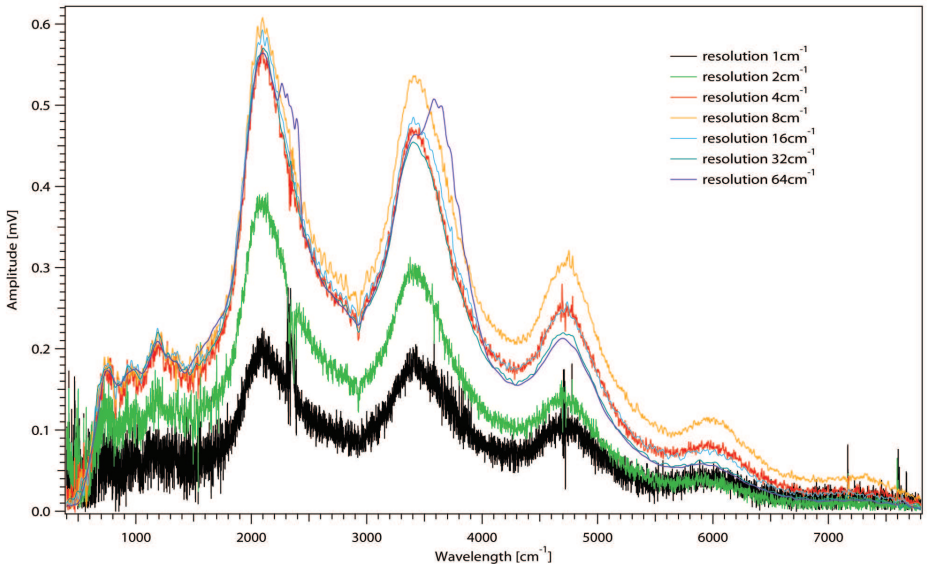

Figure 5.9: Effect of resolution on the cantilever response. Various dependencies of the the microcantilever spectra on the scanning parameters (7800 cm^{-1} to 400 cm^{-1}). The results are presented when the resolution of the spectrometer was set to 8 cm^{-1} with the velocity of displacement of the mirror varying from 0.05 to 2 $cm.s^{-1}$. A soft rectangular microcantilever (f_0=11 kHz) made of silicon (1 μm thick) and coated with aluminum (30 nm thick) was used.

Polystyrene beads (PS) of 5 μm in diameter were used to obtain preliminary spectra using the developed system. The corresponding AFM image is presented in Fig. 5.12. In additon, two types of cellulose were also used: 1) a-cellulose (Sigma) and 2) carboxymethyl cellulose (CMC) or cellulose gum. Cellulose is of current importance in biofuel research [70]. The comparative absorption spectra between standard FTIR (shown in black) and the background-corrected microcantilever probe (shown in blue) are graphed in Fig. 5.13. In Fig. 5.14 the sample material (shown in red) is directly deposited on the microcantilever and in Fig. 5.13 the sample material is on a transparent substrate in the beam path. Consequently, the probe response is due to the light transmission of the sample in Fig. 5.13 and is due to the light-induced thermal processes of the sample in Fig. 5.14, resulting in opposite curves. The main absorption bands of PS were highlighted in Fig. 5.13. The aromatic

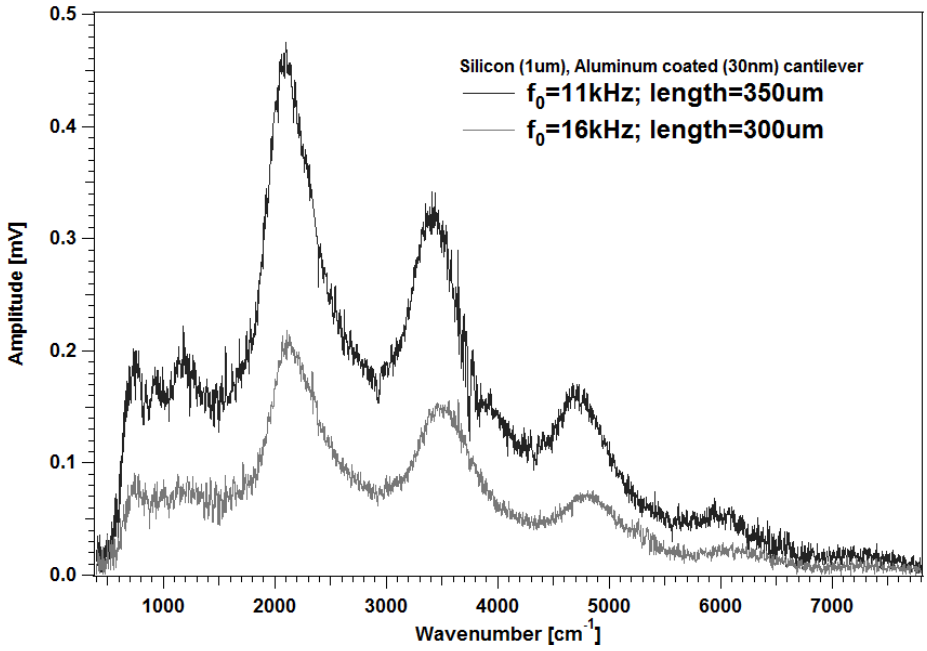

Figure 5.10: Effect of cantilever size. MEMS size dependence of the spectra. The results are presented when the resolution of the spectrometer was set to 8 cm.s^{-1} with the velocity of displacement of the mirror varying of 0.05 cm.s^{-1}. Two soft rectangular tipless microcantilevers of different length 350μm (black) and 300 μm (gray), and frequency $f_0 = 11\ kHz$ (black), $f_0 = 16\ kHz$ (gray) made of silicon (1 μm thick) and coated with aluminum (30 nm thick) were used.

ring of the polymer chain causes stretching vibrations around 1600 cm^{-1} (yellow), associated with strong absorption due to the stretching of =C-H group between 3000 and 3100 cm^{-1} (green). Additional bands corresponding to the out-of-plane deformation of C-H bonds to the aromatic ring can also be observed around 760 cm^{-1} (red). The weaker peaks in the 1600-2000 cm^{-1} region correspond to the overtone and combination bands. The other bonds of the polymeric chain, not directly related to the aromatic ring are partly seen around 2800-3000 cm^{-1} (blue). The spectra of a-cellulose (Sigma) (blue curve) and CMC (green curve) are shown in Fig. 5.15. Note that the morphology of the sample affects the quality of the spectra: CMC, being soluble in water, forms a uniform film whereas cellulose (sigma) remains a powder of 20 μm sized particles. The infrared spectrum of cellulose is quite complex to

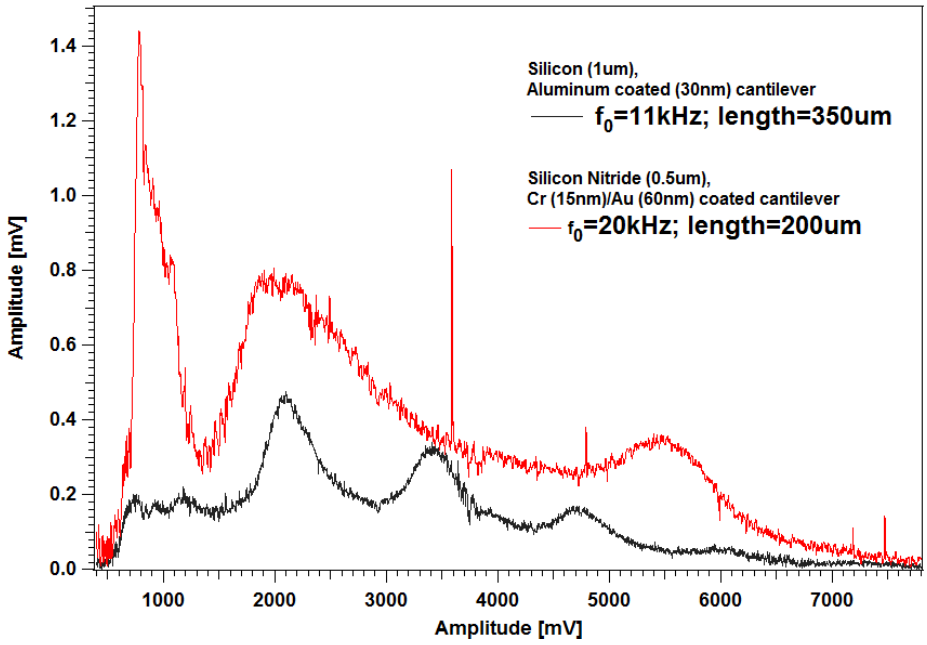

Figure 5.11: Effect of the material multilayer composition on the MEMS on the spectra. The results are obtained for a spectrometer resolution setting of 8 cm^{-1} with the velocity of displacement of the mirror varying as 0.05 $cm.s^{-1}$. (Black) Soft rectangular microcantilever (f_0 = 11 kHz) made of silicon (1 μm thick) and coated with aluminum (30 nm thick). (Red) Soft rectangular microcantilever (f_0 = 20 kHz) made of silicon nitride (0.5 μm thick) and coated with Cr (15 nm) and Au (60 nm).

assign with absorption bands, given the overlapping of various bands corresponding to various types of vibrations in the chain. The "OH region" is located between 3100-3600 cm^{-1} (bands around 2720, 3278, 3344, 3422, and 3450 cm^{-1}). The multiple

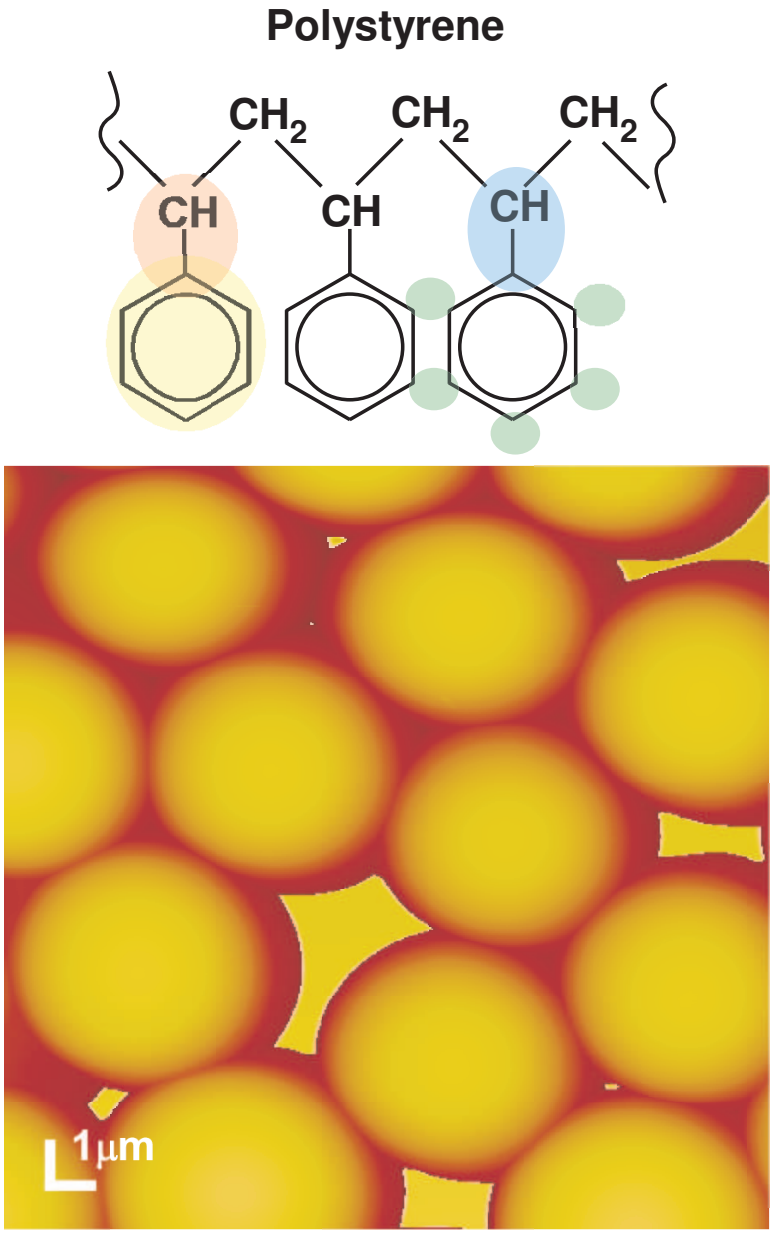

Figure 5.12: AFM topography image of the Polystyrene bead (PS). Structure of polystyrene (top). The colored circles correspond to the absorption band labeled in the infrared spectra presented in Fig. 5.13. Atomic force microscope image of the polystyrene microbeads used to provide reference spectra (5 μm).

vibrations of the CH group cause different peaks in the spectrum: symmetric stretch around 2900 cm^{-1} , wagging in the place (1400 cm^{-1}), deformation-stretch (1300-1350 cm^{-1}) and wagging (1325 cm^{-1}) [71].

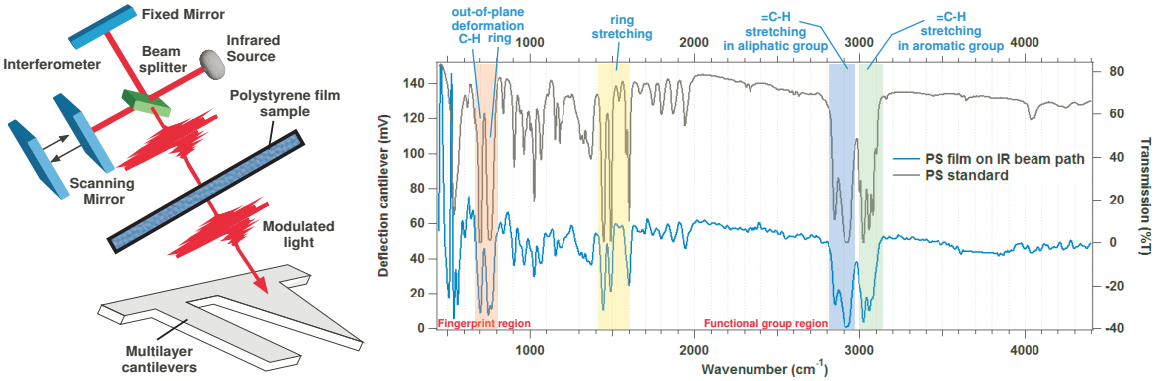

Figure 5.13: FTIR spectrum of PS filter located on the path of the IR beam of light recorded through the cantilever. Monitoring of the cantilever response using polystyrene (PS), a common IR standard. Comparison of standard FTIR spectrum of a PS film (gray), FTIR spectra of PS obtained with the cantilever, when the PS is placed in the light path (blue) and when PS is coated on the cantilever (red). The spectra are corrected using the spectrum of the bare cantilever (presented in Fig. 5.11) as the background.

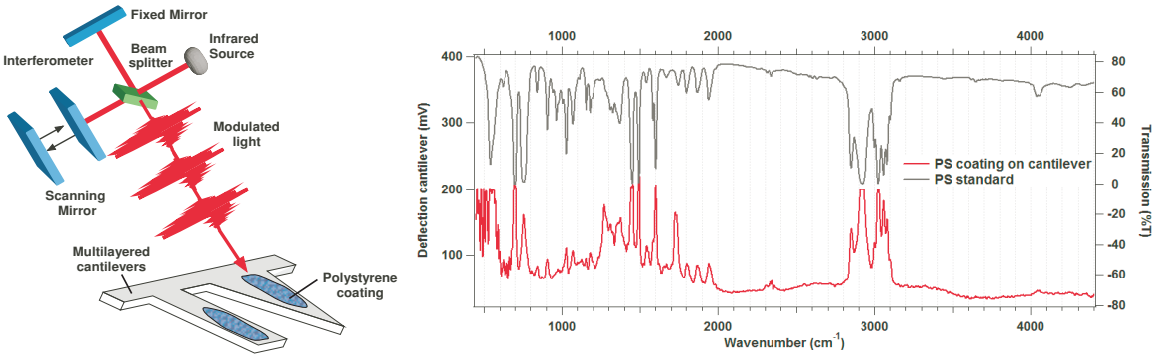

Figure 5.14: FTIR spectrum of PS coating on the cantilever. Monitoring of the cantilever response using polystyrene (PS), a common IR standard.Comparison of standard FTIR spectrum of a PS film (gray), FTIR spectra of PS obtained with the cantilever, when the PS is placed in the light path (blue) and when PS is coated on the cantilever (red). The spectra are corrected using the spectrum of the bare cantilever (presented in Fig. 5.11) as the background. The slight saturation observed in the red trace for the band around 2920 cm^{-1} and several bands between 500-600 cm^{-1} are due to the gain setting of the interface electronics of the FTIR.

Other processes that are of consequence for the local thermal state of the supporting nanostructure, such as nonradiative decay of surface modes may thus be competing with the spectroscopic response. Here we note that while transient response for example due to photon pressure or carrier generation can be useful, in this work we are concerned with essentially steady-state deformation.

Excitation of optical modes in the condensed matter can be described by the solutions of the wave equation (Maxwell's equations) subject to appropriate boundary conditions and availability of dielectric functions of the involved materials [69]. For the geometries relevant to the microcantilever platform, we have obtained analytical solutions and further simulated the optical response of a number of typical combinations of material domains for which experimental data were acquired. A full treatment of the temperature dependent optical response of a multilayered elastic beam for arbitrary polarized or unpolarized broad-spectral wide-angle illumination is

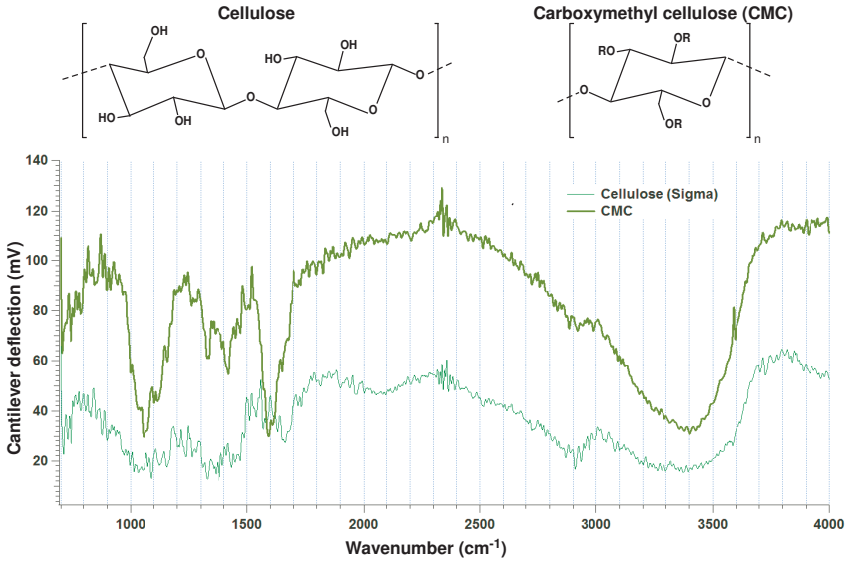

Figure 5.15: Cellulose and Carboxymethyl Cellulose. Infrared spectrum (7800 cm^{-1} to 400 cm^{-1}) of cellulose (a-cellulose (sigma)) and CMC. The results are background-corrected for the soft rectangular microcantilever (same as in Fig. 5.11) when the resolution of the spectrometer was set to 8 $cm.s^{-1}$ with the velocity of displacement of the mirror equals to 0.05 $cm.s^{-1}$.

beyond the scope of the present work. However, important results with regards to the thermal bending of the cantilevers has recently been reported [72].

5.3 Applications

5.3.1 Localization of embedded nanostuctures

For the first nanofabricated sample described in Fig. 4.6, as can be observed by direct comparison between the topography image and the ones from MSAFM in Fig. 5.16, numbers 4 and 6 are not apparent at the surface level. This is what the sample was designed for initially. The residues present for dots 1, 2, 3, and 4 are mainly due to non-optimized parameters, such that the hole (dot) created in the conductive layer by RIE could not be filled at the same level as the level of the matrix.

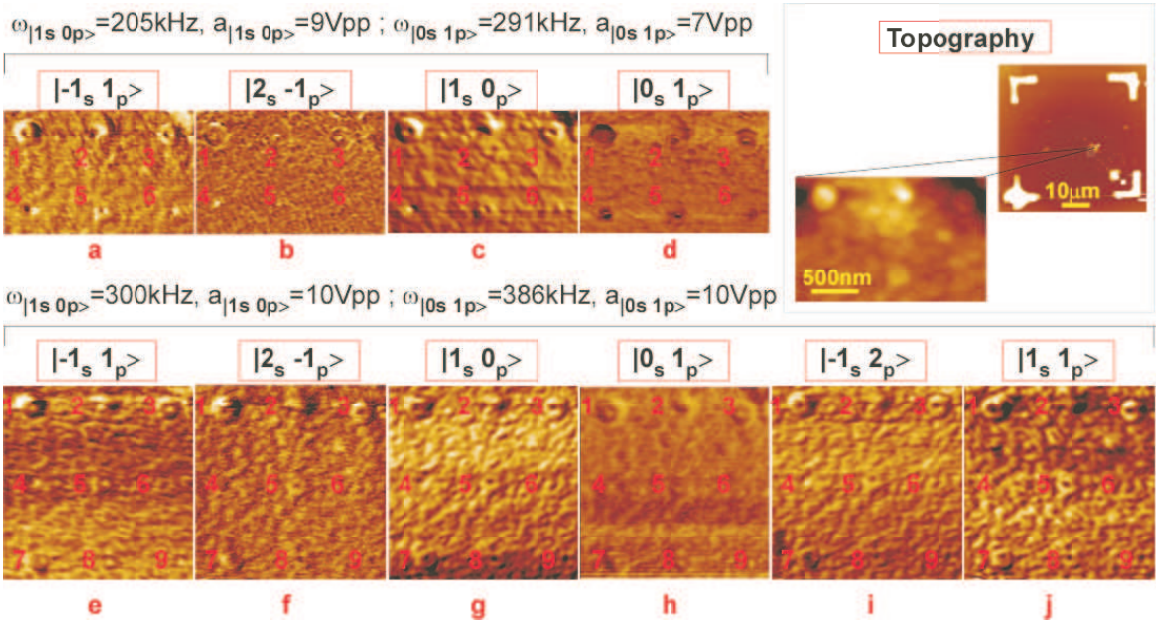

Figure 5.16: Analysis of nickel nanostructures confined in a germanium coating on a quartz substrate using MSAFM. (a-d) Simultaneous mode-images of six nanofabricated dots confined at various locations within the germanium layer. (e-j) Simultaneous modes images of nine nanofabricated dots confined at various locations within the germanium layer.[55]

All the images presented here result from the amplitude of the signal at the indicated frequency $\omega_{|ij>}$. In the first set of data (a-d), although the amplitude of the signal varies from one mode to the other, the six dots are visible in all four images. Images (a) and (c) present some common features, which indicate the subsurface

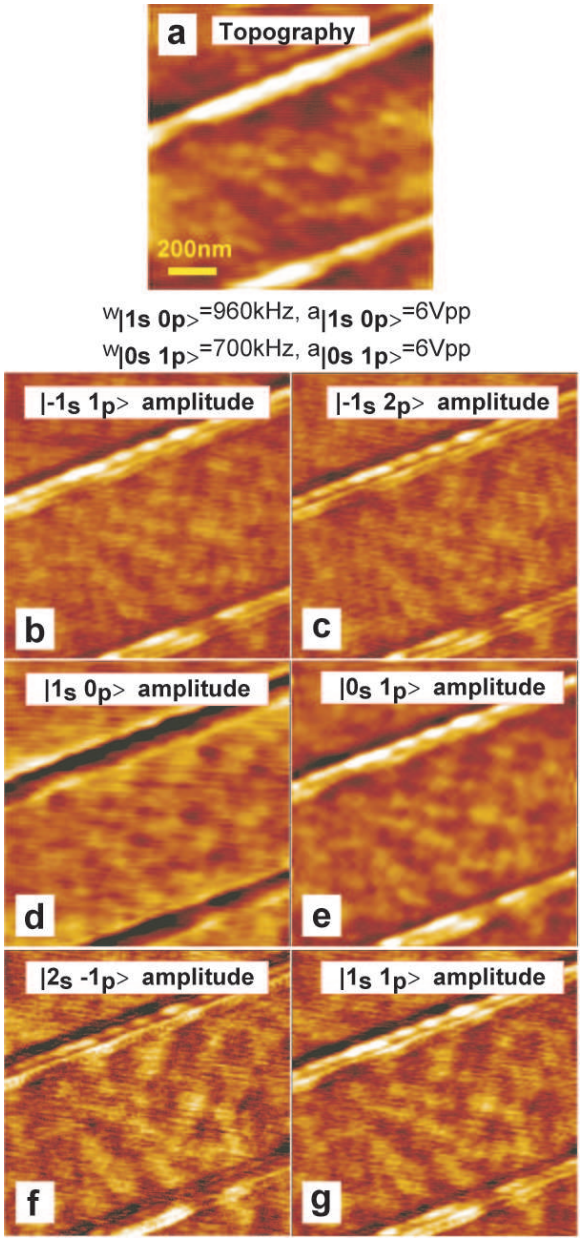

Figure 5.17: Analysis of lines of exposed PMMA using MSAFM. Simultaneous mode-images of two e-beam exposed lines on PMMA film.[55]

information provided by MSAFM. A stronger contrast between the substrate and the dot structures can be observed in (d). (6d) is still apparent although it is the best embedded structures of all. Although the amplitude associated with $|2s - 1p >$ did not compete with the lower order coupling, all 6 dots can also be observed, with a strong contrast between the core of the dots and the rest of the sample. We note that the images associated to the higher order coupling, when the frequencies do not match with any of the resonance frequencies of the system, tend to have smaller amplitude. It is especially true for softer cantilevers (k=0.06N/m). The peripheral region around the dots, in particular around 1 and 3, are associated to the nanofabrication process, which can sometimes be uneven. In this particular case, 1 and 3 can be observed clearly in the topography image, which lead us to think that the feature was not in fact buried. In the second set of data (e-j), 9 dots can be distinguished, 6 of which (1-6) are similar to the ones presented in the first row. (e) and (j) tend to be more sensitive to the roughness of the surface of the sample, but present also subsurface information from the buried structures. It is interesting to notice that, in some cases such as between (g) and (h), the contrast is inverted. For example, the central dot structure reveals a stronger signal in (5e) but appears darker in (5j). When comparing (g) and (h), (3) might be a better example. Note also that the peripheral region is not exactly responding the same way to the different frequencies. It might be a interesting point to keep in mind for further investigation. We could also compare the same mode for different excitations. For instance, (a) and (e) both exhibit a variation in the signal at the location of the structures 6. However there is a noticeable difference in the response of the rest of the sample to the different frequencies involved in the system, (a) revealing a finer grain than (e). This might in fact be related to the original depth of the information. Inspection of the sample described in Fig. 4.7 using MSAFM reveals details about the mechanical properties of the exposed polymer, which were not readily apparent in the AFM topography image. In this set of data (Fig. 5.17), the higher coupling modes indicate some difference in the composition of the lines when compared to the excitation modes and/or the topography. Different regions can

readily be distinguished. Since we designed to sample so that PMMA would be the only material on the surface, the difference in composition is expected to originate from the e-beam exposure. Depending on the parameters used, the polymer is affected in different ways. Between the lines, the material appears to be pretty homogeneous and composed of different grains according to the variations of amplitude. $|1s\ 0p>$ (d) and $|0s\ 1p>$ (e) do not exhibit the differences of structures of the PMMA layer within the lines. It might be of interest to note that the features resulting from locking onto $|1s\ 0p>$ (d) appear to be opposite to the ones resulting from locking onto $|0s\ 1p>$ (e). The details revealed in (f) are richer than in any of the other images. In general we observed more details coming out of higher order couplings, although they are more difficult to excite given the novelty of the technique. It is expected that engineering optimizations would improve most of these drawbacks.

5.3.2 Characterization of biomass at the cell wall level

To demonstrate how MSAFM successfully accesses new dimensions of sample information, we use two sets of $\mathcal{C}$-modes to image the poorly understood cross sections of *Populus* wood. In the first set, shown in Fig. 5.18 (a-d), the participant modes were selected to be $|nm>=|-1_s\ 1_p>$ (Fig. 5.18 (a,e)), $|-1_s\ 2_p>$(Fig. 5.18 (b,e)), $|1_s\ 1_p>$(Fig. 5.18 (c,e)), and $|0_s\ 2_p>$(Fig. 5.18 (d,e)) originating from $i=j=1$, while Fig. 5.18 (g-j) display images acquired by $|nm>=|-1_p\ 1_p>$ (Fig. 5.18 (g,f)), $|2_p\ -1_p>$(Fig. 5.18 (h,f)), $|-1_p\ 2_p>$(Fig. 5.18 (i,f)), and $|0_p\ 2_p>$(Fig. 5.18 (j,f)) originating from $i=1,2$, and $j=0$ (i.e., no subsurface contribution). A remarkable diversity in the gained information can readily be observed in these results. We emphasize that the information in any one image cannot simply be generated by a scaling or a transformation from another image, and that each $\mathcal{C}$-mode taps into an auxiliary dimension of information space of the sample. Thus, MSAFM, in a single run, yields a detailed manifold and exploits the true dynamic richness of the nonlinear

interaction.

The chemically and morphologically complex *Populus* wood and plant cells are currently of prime interest for biomass conversion [57, 73]. However, due to this complexity, nondestructive characterization of such samples is challenging, providing a superb opportunity for force microscopy. Indeed, an accurate model of the organization (chemical, structural, $\cdots$) of biomass at the cellular level is still missing, slowing progress towards overcoming recalcitrance[57, 73]. In Fig. 5.18 (a-d) the

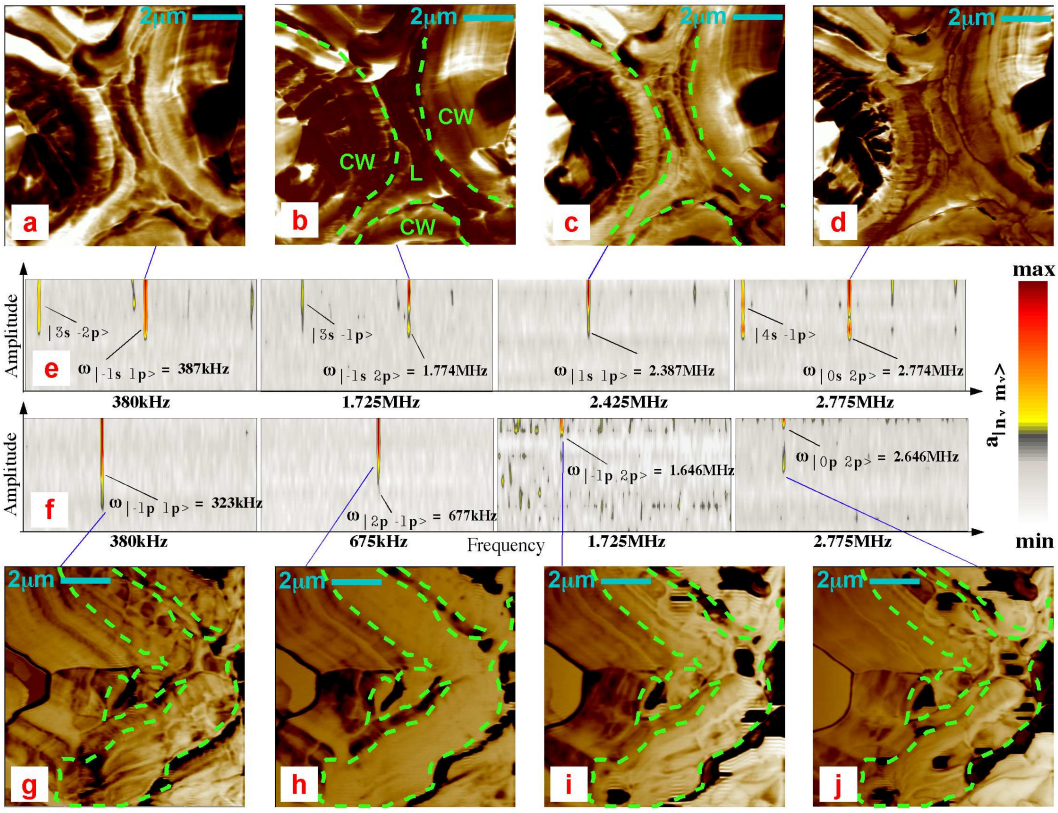

Figure 5.18: Analysis of cross sections of fresh *Populus* wood with MSAFM. (a-d) Simultaneous $\mathcal{C}$-mode imaging of a *Populus* sample resolving cell walls (CW) and middle Lamella (L), reveals distinct features of the complex organic matrix. (e) Contour plots of partial spectral windows containing the invoked $\mathcal{C}$-modes. (f-j) The $\mathcal{C}$-modes from the excitation of the probe with two independent waves but maintaining a stationary sample. The cell wall regions and the lamella can be identified from the complementary information contained by each image.[55]

middle lamella (L), interstitial region between different cell walls (CW) are presented in light of the different higher order couplings of MSAFM. Here, the probe was driven at amplitude of 10 Vpp, and the sample at amplitude of 9 Vpp. The spectrum providing each $\mathcal{C}$-mode invoked is presented in Fig. 4e: $\omega_{|-1_s\ 1_p>}$ = 387 kHz (a), $\omega_{|-1_s\ 2_p>}$ = 1.774 MHz (b), $\omega_{|1_s\ 1_p>}$ = 2.387 MHz (c) and $\omega_{|0_s\ 2_p>}$ = 2.774 MHz (d). Clearly each of the MSAFM images highlights unique features of the plant cell walls, not retrievable from others by post-processing. The AFM image (topography as well as a larger scan of the same region) are presented in Fig. 5.19 for comparison.

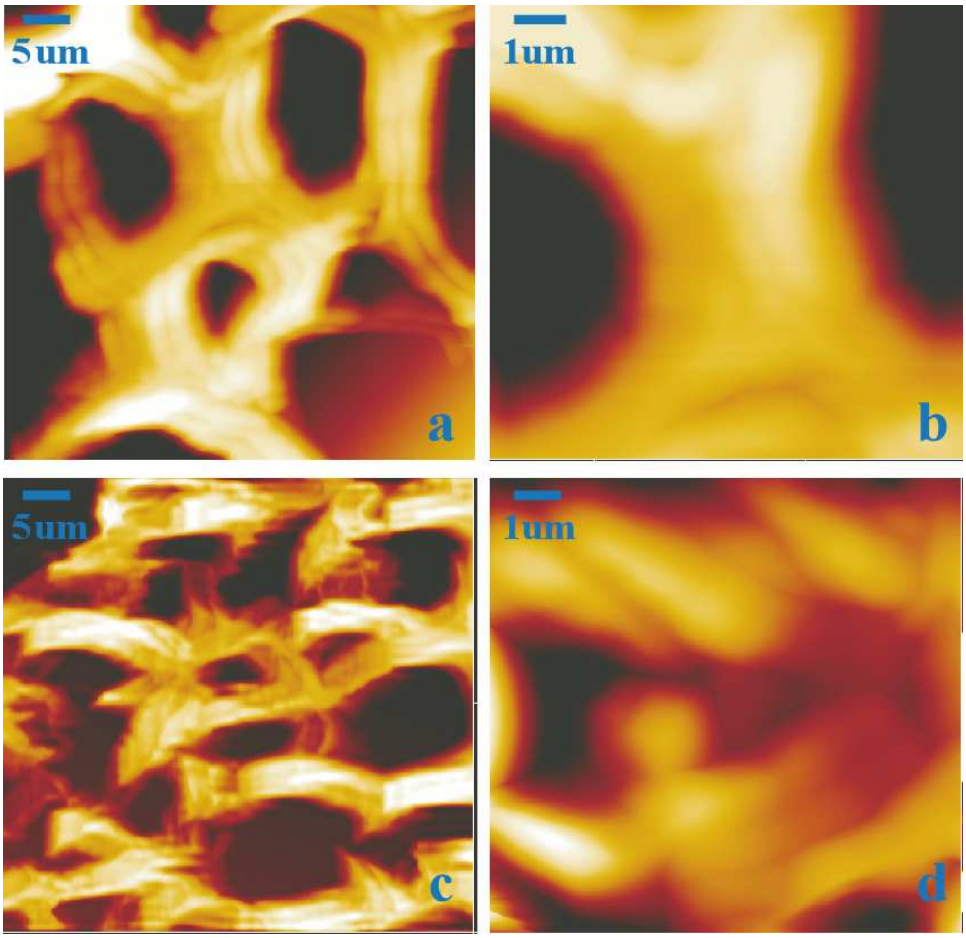

Figure 5.19: Topography images of a cross section of fresh poplar wood obtained with standard AFM. (a,b) Topography images (respectively 50 μm and 9 μm) corresponding to Fig.4(a-d). (c,d) Topography images (respectively 50 μm and 10 μm) corresponding to Fig.4(a-d).[55]

The observed difference in the textures and contrast in the figures are related to the properties of the sample and can be used to characterize the different layers of the plant cell wall. MSAFM allows both the amplitude and the phase of $S(t)$ to be used to study the differences in the roughness, elasticity, viscosity, compliance,$\cdots$. In Fig. 5.18 (g-j), a larger CW of the sample is presented by invoking the $\mathcal{C}$-modes:

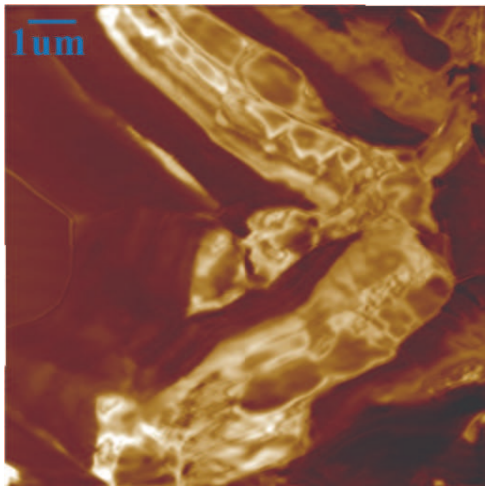

Figure 5.20: MSAFM image for $|0_s\ 2_p>$-mode. The excitation of the sample in the case of MSAFM with two initial excitations gives access to additional details (subsurface) when compared to the images of the same region obtained for the same excitations (Fig. 5.18 (i)) by driving only the cantilever (with two frequencies).[55]

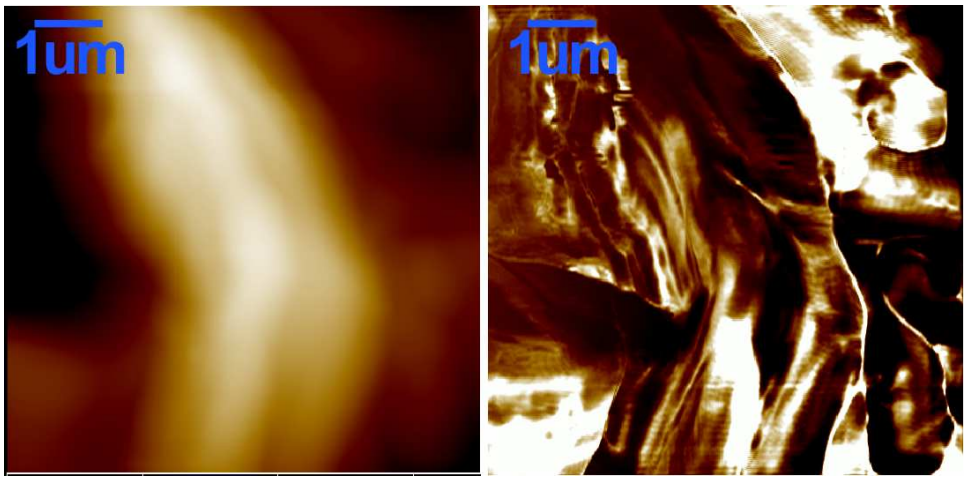

Figure 5.21: MSAFM image of a *Populus* cell wall in the configuration of three excitation states. (left) Standard AFM topography image (7 μm scan) of a *Populus* cell wall. (right) MSAFM images of the same region at $|1_p\ -1_p\ 1_s>$.

$\omega_{|-1_p\ 1_p>} = 323$ kHz (g), $\omega_{|2_p\ -1_p>} = 677$ kHz (h), $\omega_{|-1_p\ 2_p>} = 1.646$ MHz (i), and

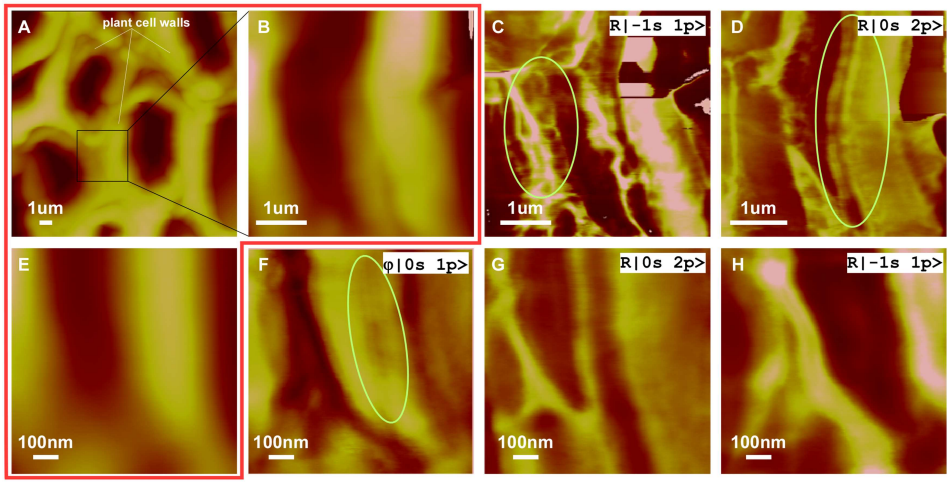

Figure 5.22: Imaging the cell wall using MSAFM modes. Characterization of the cell walls of fresh Populus. (A, B, E) Topography AFM images (marked in the red box). (C, D, F-H) The corresponding MSAFM images reveal nanoscale features of the complex composition of the plant cell walls, which were not accessible with standard AFM microscopy. For example vacuole-like structures in (C) or the interface between layers (D,F) can be observed (see circles). MSAFM parameters: $|1_s\ 0_p\rangle = 1$ MHz, 5 Vpp -$|0_s\ 1_p\rangle$=1.39 MHz, 6 Vpp. (C) R$|-1_s\ 1_p\rangle$, (D) R$|0_s\ 2_p\rangle$, (F) j$|0_s\ 1_p\rangle$, (G) R$|0_s\ 2_p\rangle$, (H) R$|-1_s\ 1_p\rangle$.

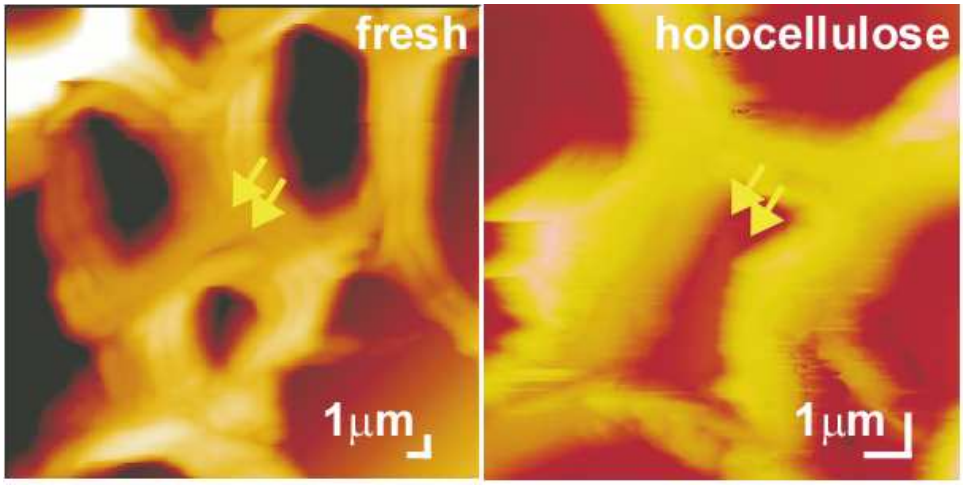

Figure 5.23: Fresh *Populus* vs. Holocellulose. Effect of the chemical treatment on the cell walls (scale bar 1μm). Fresh *Populus* (left), and Holocellulose (right). The chemical treatment contributed to the removal of the middle lamella accross the sample, resulting in a change of mechanical properties of the cell walls.

$\omega_{|0_p\ 2_p>} = 2.646$ MHz (j) originating from the spectrum in Fig. 5.18 (f). Both Fig. 5.18 (a) and (g) display a higher sensitivity to the roughness of the sample with (g) revealing details that are absent in all the other bottom images. The corresponding image from AFM does not resolve these details (see Fig. 5.19 for AFM topography and Fig. 5.20 where we also present an image of the same area when both the cantilever and the sample are excited). An impressive set of details of the sample can be observed. Cellulose microfibrils are present in Fig. 5.18 (a) and (g) in the region closer to the vacuole, indicative of the cellulose content of the secondary CW. The different properties of the lamella (L) appear in the series of the top images, in particular Fig. 5.18 (b). The secondary CW also appears as an inhomogeneous medium. Fig. 5.18 (c) and (d) highlight other details of the CWs: (d) is richer in the

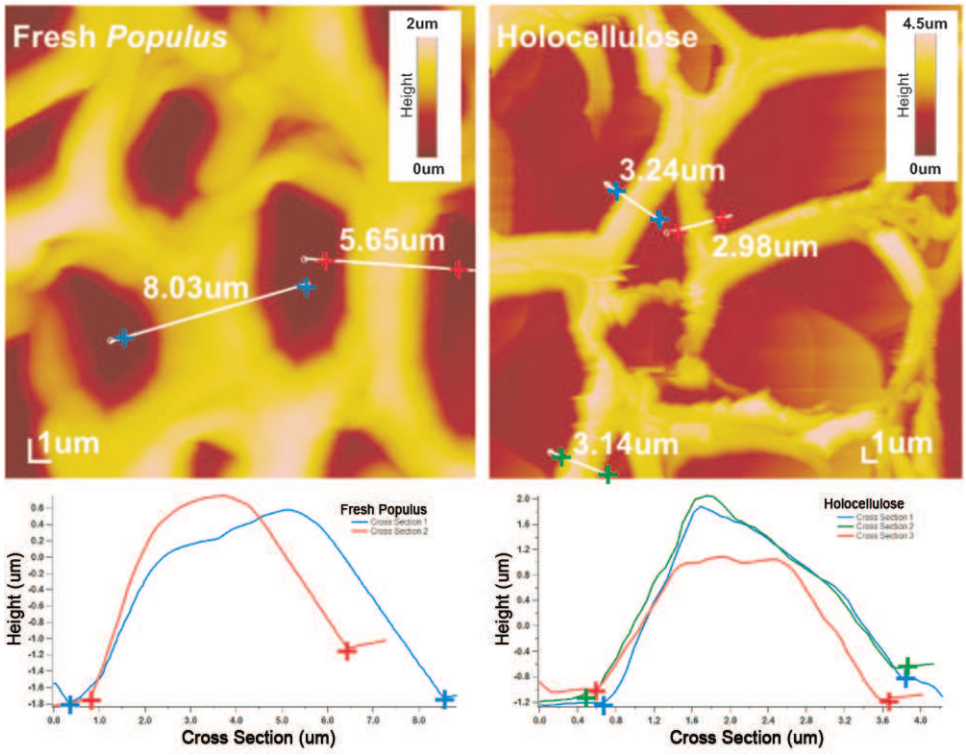

Figure 5.24: The influence of chemical treatments on the cell wall morphology. Measurements of the thickness of the cell wall obtained by cross section on the AFM topography images of holopulp sample show the effect of the holopulping treatment on the cell wall structures.

contrast and exhibits certain grain structure, especially in L, whereas the contrast in (c) tends to show that the amplitude of the signal is more sensitive to the changes in z (height) (dark regions) than (a), (b) and (d). Indeed (c) is the only image that does not exhibit a change of color in the CW on the left (close to the green limit), which is observable in the others, especially in (d). Parallel study of the various $\mathcal{C}$-mode images helps differentiate the different main regions (CM and L).

The images obtained without a direct subsurface contribution (probe excitation only), Fig. 5.18 (h to j), tend to respond strongly (high signal is black on the bottom images) to edges or particular structures for large and rough areas and thus limit the contrast for the rest of the sample. Comparing Fig. 5.18 (h to j) to the image obtained for the same parameters but with the sample at contribution (see Fig. 5.20) it is then possible to identify subsurface features. In Fig. 5.21 we present an MSAFM image obtained while three mechanical forcings were applied on the system (two on the probe, one on the sample), for the same area as the one presented in Fig. 5.18 (h to j).

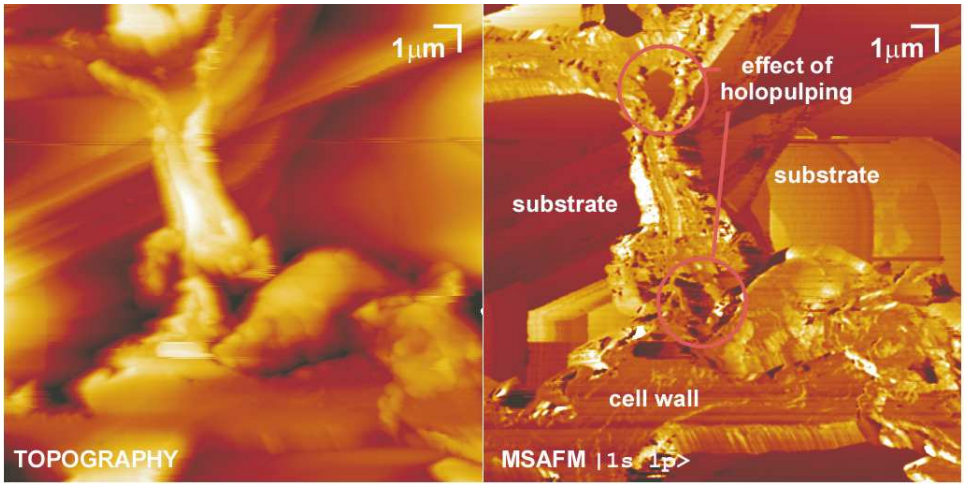

Figure 5.25: Imaging the cell wall of the holocellulose sample using MSAFM $|1_s\ 1_p>$**.** MSAFM image of holocellulose sample (scale bar 1μm). The MSAFM image (right) was acquired using R$|1_s\ 1_p\rangle$ with $|1_s\ 0_p\rangle$ = 200 kHz, 1 Vpp -$|0_s\ 1_p\rangle$=50 kHz, 2 Vpp. MSAFM allows the identification of change in material (substrate and voids in cell walls).

Fig. 5.18 and Fig. 5.22 illustrate the performance of MSAFM on a cross-section of fresh *Populus* wood. In addition to the complex structure of the sample at a given location, from the differences between the top and bottom series of images one can notice that variations of morphology exist between two different regions of a same cross section. For example, the average size of the cell walls in the region where the bottom images of Fig. 5.18 where taken was larger than the top images. Topography images corresponding to the MSAFM images of Fig. 5.18 are presented in Fig. 5.19. The increase in the size of the CW can be due to the evolution of the populus system. The primary and secondary CWs are formed at different stages in the evolution of the *Populus*. Growing and dividing cells will be composed of primary CW, which is thin and flexible. The stronger and more rigid secondary CW will appear after maturation of the cell. Secondary CWs are abundant in *Populus* tissues and is rich in cellulose.The lamella is now believed to be rich is lignin and act as a "glue" between the different cells of the plant. These different properties are reflected by the difference in contrast and features between the different images of MSAFM. Fig. 5.20 is the $|0_s\ 2_p>$ image to be compared to Fig. 5.18 (h-i). Clearly in the case of this particular sample, MSAFM opens a new dimension in the study of nanoscale features of biomass. The images complement each other by highlighting different properties simultaneously. These results have been reported in [55, 70].

A deeper understanding of the mechanisms involved during the chemical treatments and processes used to breakdown cellulose into simple sugars and for their conversion into biofuel is still needed. This information would facilitate progress in the development of engineered plants dedicated to biofuel production. Using the unique capabilities of MSAFM for imaging materials and detecting changes in physical properties at the nanoscale, we characterized fresh *Populus* cross sections (Fig. **??**) and a similar cross section after holopulping treatment intended to remove the lignin content of the cell wall (Fig, 5.23).

In Fig. 5.22 the standard AFM topography images are marked with a red outline (A, B, E). Corresponding simultaneous MSAFM images (C, D, F-H) reveal new

nanoscale features of the complex composition of the plant cell walls, which were not accessible with standard AFM microscopy. For example vacuole-like structures in (C) or the interface between layers (D, F) could be observed (see circles). For this study the MSAFM operational parameters were: $|1_s\ 0_p\rangle$ = 1 MHz, 5 Vpp - $|0_s\ 1_p\rangle$=1.39 MHz, 6 Vpp. (C) R$|-1_s1_p\rangle$, (D) R$|0_s2_p\rangle$, (F) $\theta|0_s1_p\rangle$, (G) R$|0_s2_p\rangle$, (H) R$|-1_s1_p\rangle$. The effect of holopulping treatment on the sectioned samples is illustrated in Fig. 5.23, where the area richer in lignin content seems to be removed in the holocellulose sample (see arrows). In Fig. 5.23 and Fig. 5.24, a comparison between the cell walls of the fresh sample and the cell walls of the holocellulose sample is made, using the AFM topography images. The cross section (data processing) of the cell wall, taken at the location of the line markers, produces a profile that allows further analysis such as cell wall thickness measurements. As indicated on Fig. 5.24, the cell wall before treatment is around 8 μm, whereas the measurements indicate $3-4$ μm for the holopulping sample. The overall morphology of the chemically modified sample exhibits changes when compared to the fresh sample, with an apparent void appearing in the naturally lignin-rich lamellar region after lignin removal by holopulping treatment. Similar observations were made in previous study by Ragauskas et al. [58]. Morphological changes can be correlated to chemical changes in the cell wall, and provide valuable information on the role of lignin or cellulose in the stiffness/rigidity/cohesion of the wall [74, 75, 58]. The cell wall thickness changes may relate to the collapse of the cell wall when dried after pretreatment. Furthermore, the MSAFM images of the holocellulose sample obtained simultaneously reveal the complex structure of the surface. The results are presented in Fig. 5.25. MSAFM clearly facilitates the localization of areas where the chemical treatment affected the cell walls. It also helps differentiating the substrate (in this case glass slide) from the plant sample. The MSAFM image in Fig. 5.25 was acquired using R$|1_s1_p\rangle$ with $|1_s0_p\rangle$ = 200 kHz, 1 Vpp and $|0_s1_p\rangle$=50 kHz, 2 Vpp. We note that the extend to which surface versus subsurface features are resolved in MSAFM will depend on the particular mode utilized. In the case of complex samples the differentiation

among the depth of subsurface information, beyond what may be gathered based on visual inspection, will require careful comparison of the various amplitude and phase images in conjunction with a calibration scheme. Even at this early maturation level, the wealth of information provided by MSAFM while investigating plant cells is noteworthy from the data presented here.

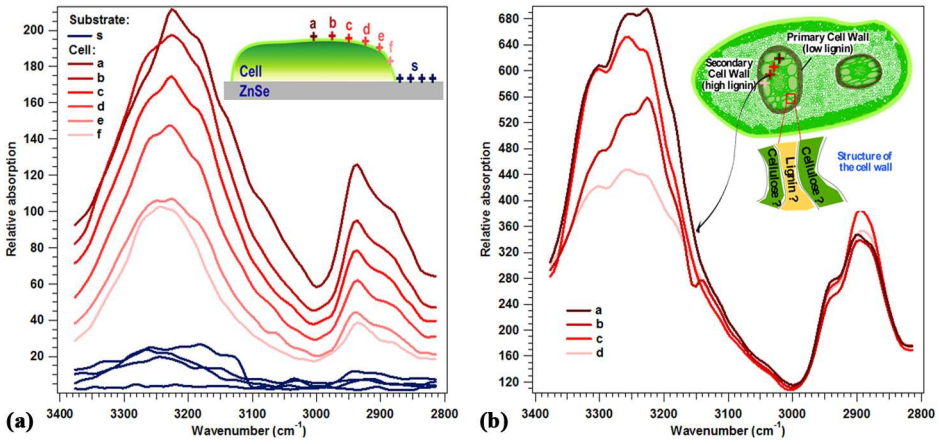

Figure 5.26: Partial infrared spectrum of biomass material at the nanoscale. Infrared spectra obtained for a single plant cell (left) and a cross section of wood (right). The measurements exhibit variations in chemical composition within the cell wall (left). The results were reproducible and the signature disappeared away from the biomass material (blue curves,right). The 3400-2800cm^{-1} corresponds to the region where the hydrogen bonding stretching happens.

However, despite the great promises of this work, the information provided remains limited to mechanical and structural properties. Taking advantage of the results we obtained using photonic coupling to the cantilever, we performed a series of measurements on the fresh cross section of *Populus* and were able to detect infrared spectra of the plant cell wall using an AFM configuration. The first results are presented in Fig. 5.26. Although they demonstrate, for the first time, some variations in the chemical composition within the cell wall, numerous challenges remain concerning the meaning of the peaks observed, or the resolution of the technique. The advances study of these challenges will be the focus of upcoming

publications. In addition, the limited span of wavelengths available in the data presented (hydrogen bonding stretching happens in the 3400-2800cm^{-1} region of the spectrum) here indicate the need for FTIR-like measurements at the nanoscale, when dealing with complex systems such as the plant cell walls. This works great promises for important discoveries.

5.3.3 Localization of various nanoparticles inside cells

Biological impact of nanomaterials is an emerging research area due to their potential applications such as in drug delivery, but also because of the adverse effects and the cytotoxicity that they may invoke. One of the exposure routes of greatest concern is inhalation because of the ease with which nanoparticles can become aerosolized. Imaging techniques that allow localization and visualization of

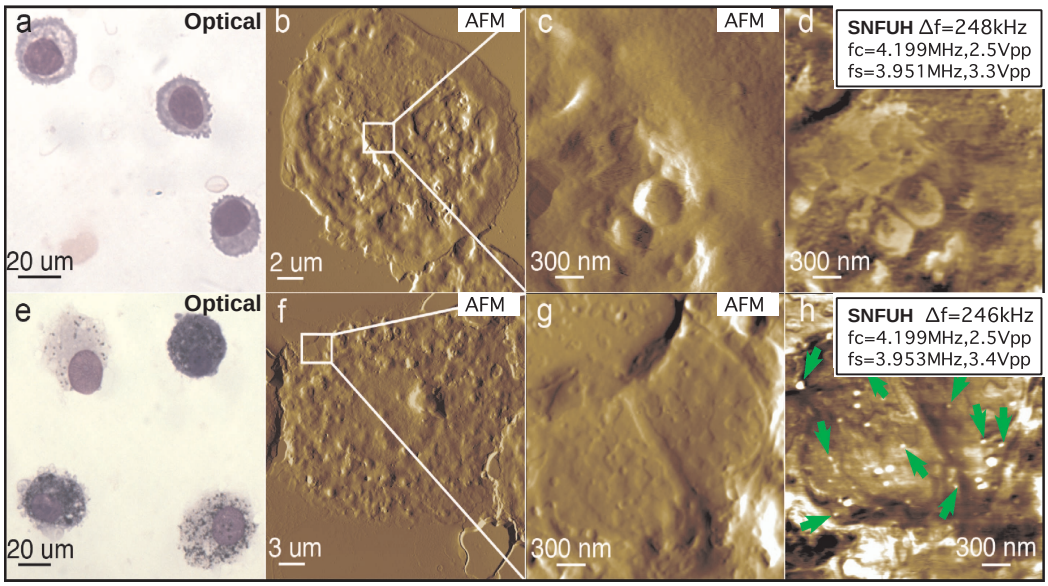

Figure 5.27: Presence of SWCNHs inside the cells obtained from mice lungs. Alveolar macrophages from vehicle control (a-d) and mice exposed to SWCNH after 7 days (e-h). Representative optical (a,e), AFM topography (b,c,f,g), and MSAFM phase (d,h) images from control and treated mice. White dots in (h) (some indicated by the green arrows) correspond to SWCNH [76].

nanoparticles with nanometer resolution within the cellular structure are therefore of paramount importance. We have investigated the fate of nanoparticles using mouse

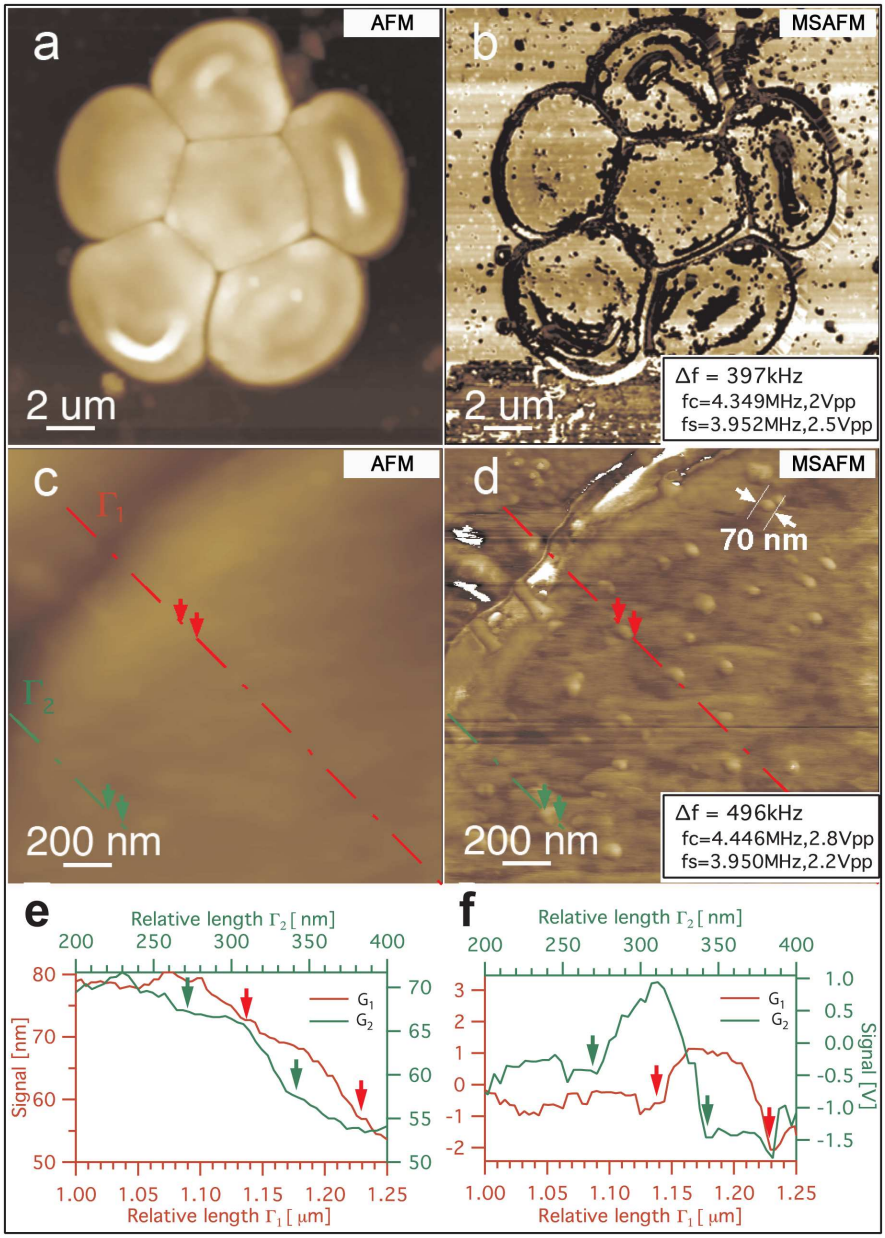

Figure 5.28: Nanoparticles detected inside red blood cells. AFM Topography (a,c) and MSAFM phase (b,d) images of erythrocytes from BAL fluid of an SWNCH-exposed mouse 24 h post-aspiration. Profiles in (e) and (f) have been taken along Γ_1 and Γ_2 across buried nanohorns in (c) and (d), respectively, show that MSAFM can resolve nanoparticles that are inside cells [76].

model exposed to SWCNH by pharyngeal aspiration [76, 77, 78]. Subsurface cellular imaging of BAL using MSAFM reveals carbon nanohorns residing inside the cells.

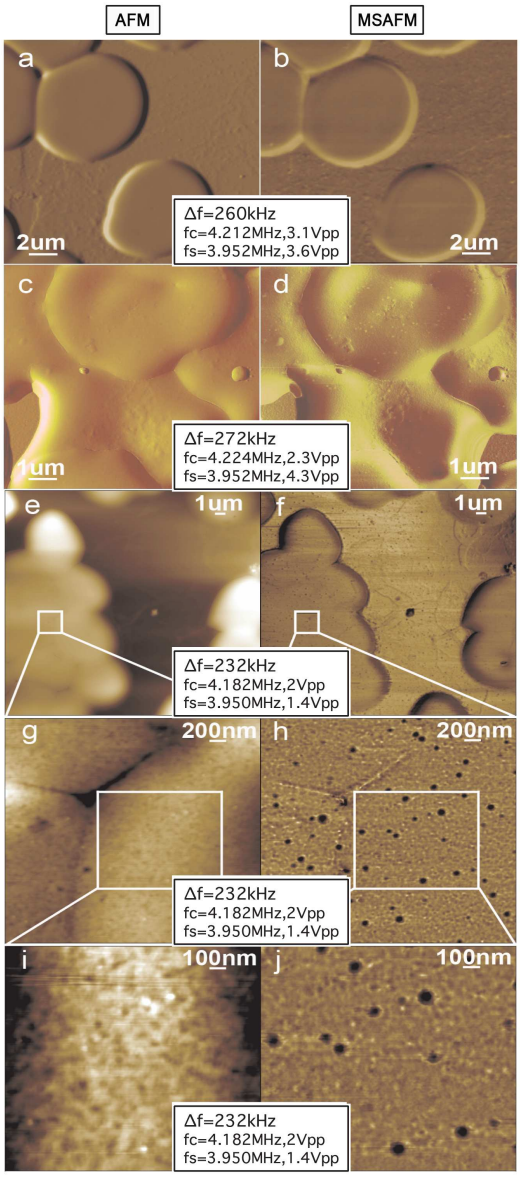

Figure 5.29: High-resolution images of nanoparticles in red blood cells. AFM topography (a) and MSAFM phase (b) images of peripheral erythrocytes from a control mouse. Topography (c,e,g,i) and MSAFM phase (d,f,h,j) images of peripheral erythrocytes from a SWCNH-exposed mouse sacrificed 24 hours after exposure. Successive reduction in the scan size (24.4 μm to 3 μm to 1.55 μm) resolves the 80-100nm particles inside the cells [76].

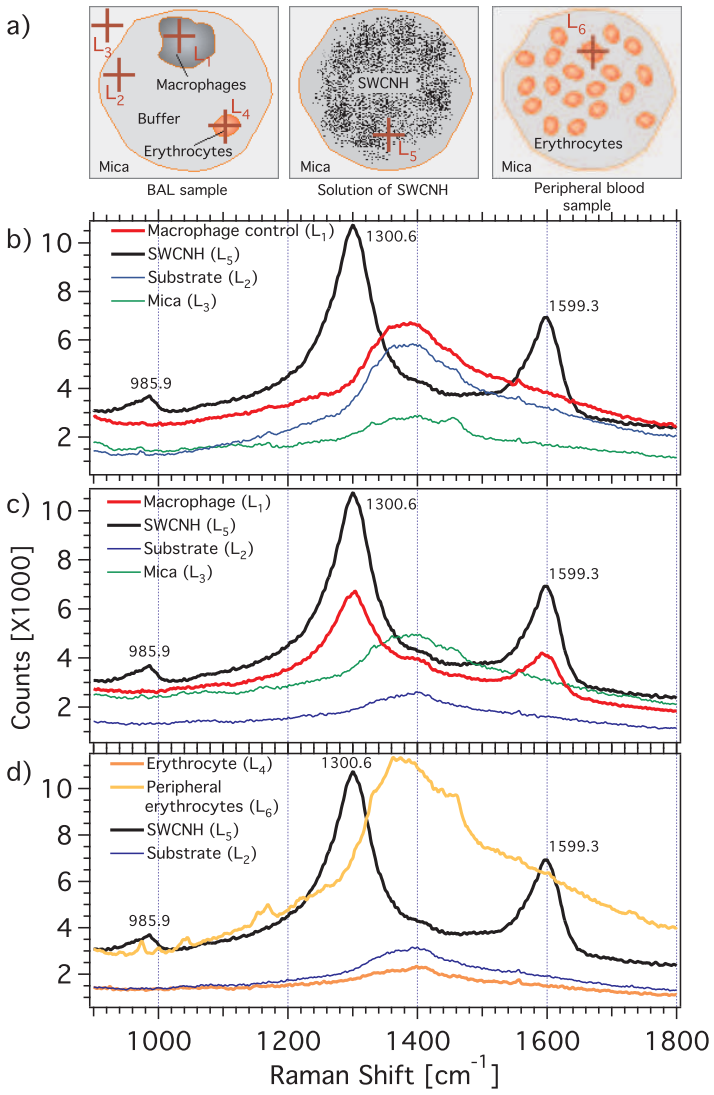

Figure 5.30: Confirming the presence of SWCNHs inside cells using Raman spectroscopy. Raman spectra of BAL sample 7 days after exposure to SWCNH (b) and of a vehicle control for the same period (a). The insets in (a), (b) and (c) depict the typical loci where Raman photons were collected. Multiple measurements were thus performed within the macrophage L_1 (red), just outside but within the buffer L_2 (blue), and on the mica substrate outside the bufferL_3 (green). Using the same mica substrate, the spectra of nanohorns L_5 (black) were obtained from a solution of SWCNH suspended in 1% pluronic with PBS that had been used for the aspiration. The absence of SWCNH signal for the erythrocytes present on BAL samples L_4 (orange) and in the peripheral blood L_6 (yellow) is displayed in (c) [76].

Note that all the measurements presented here were obtained using the difference mode, i.e $|-1_s\ 1_p\rangle$. The visualized intracellular particle population was further probed using micro Raman spectroscopy whence signature of carbon nanohorns from macrophages was measured. New findings in drug delivery, nanotoxicology or interactions between engineered nanomaterials and biological systems could emerge from the present work. The rising commercial use of engineered nanoparticles and the ensuing need for large-scale production pose a risk of unintended human exposure that may impact health [79, 80, 81, 82]. Central to this issue is the ability to determine the fate of nanoparticles in biological systems and in more details their route after inhalation. Collectively, studies to date suggest that toxicity varies widely depending on the chemical content and physical characteristics of the particle [83, 84], creating a need for particle-specific toxicity studies [85, 86]. As yet electron microscopy is the technique the most commonly used to study intracellular structures [87, 88]. Therefore, an analytical tool to examine a surrogate, minimally invasive test system such as BAL or blood can provide a useful screening. Attempts to use TEM to locate nanotubes within alveolar macrophages could positively identify only aggregates [88, 89]. Very recently, using TEM, Porter et al. reported the observation of carbon nanotubes in lysosomes [89]. For a comparable resolution AFM is advantageous [48, 47, 90, 63] because of simpler sample preparation and ability for ambient imaging. However, conventional AFM typically only probes the surface of a specimen with a cantilever tip, making it difficult [15] to analyze structures within a cell. One may envision this limitation as being due to a lack of mechanical excitation of the sample resulting in the inability of the probe to gather the subsurface dynamic attributes.

MSAFM [76, 55] offers a potential circumvention enabling subsurface imaging of soft samples suggesting it to be a potential method to probe cellular uptake of nanoparticles. The phase information in the coupled mode may be detected at the difference frequency [91], which can be displayed as a function of spatial location of the scanning cantilever tip. The resultant phase map may then reveal any contrasts due to acoustic impedance variation that results from nanoscale heterogeneity in a

volume of the cell directly underneath the AFM tip and amounts to a mapping of the cell's elastic response. We explore this viability by using MSAFM to determine the cellular fate of SWCNH using a mouse model to detect and visualize particles within lavage macrophages and erythrocytes (blood cells).

Optical images of macrophages collected from both vehicle controls and SWCNH-treated mice sacrificed 7 days after exposure, shown in Fig. 5.27, reveal the presence of various-sized carbonaceous aggregates within the cytoplasm of macrophages from SWCNH exposed mice (Fig. 5.27 (e)) that are not present in controls (Fig. 5.27 (a)). No such aggregates could be identified by visual inspection of the optical images of the erythrocytes. The region occupied by the nucleus is readily detected and the characteristic macrophage morphology is present in both samples (Fig. 5.27 (b,f)). The topographic image of an alveolar macrophage from an SWCNH-exposed mouse depicts nanoparticles on the surface of the cell (Fig. 5.27 (g)). A striking visualization of the nanohorns buried inside the cell was obtained from the MSAFM image of the same macrophage (Fig. 5.27 (h)) revealing several SWCNH within the cell (marked with arrows in Fig. 5.27 (h)), not visible in the topography image (Fig. 5.27 (g)). Detected for the first time, the sizes of these high-contrast circular particles (presented as white in color) are statistically consistent with the size distribution (70-110nm) that we had assembled from analyzing several AFM images of the SWCNH solution, indicating that nanoparticles, rather than larger aggregates, were taken up by macrophages. No particles were observed in images of BAL cells from control mice (Fig. 5.27 (d)). The contrast in the images, measuring the phase of the local tip-cell surface coupling, originates from the difference in elasticity and density between the SWCNH and the cell and its infrastructures. Interestingly, as in the case of macrophages from SWCNH-exposed mice, we encounter nanoparticles within erythrocytes that were present (although rare) in BAL samples. Soft tissue damage that may occur during the process of harvesting the BAL sample, and/or cross-contamination of BAL fluid with blood as it is withdrawn from the lung can result in the rare observation of erythrocytes in lavage. Fig. 5.28 (a) and (b), show

the topography and MSAFM phase images of erythrocytes that were present in BAL fluid extracted from a mouse 24 hours after SWCNH exposure. While the topograph only resolves nanoparticles on the cellular surface of the erythrocytes (Fig. 5.28 (a)), a surprisingly large number of additional particles are detected in the MSAFM image captured at the same location as the surface topograph (Fig. 5.28 (b)). Higher resolution images of topography (Fig. 5.28 (c)) and MSAFM (Fig. 5.28 (d)) consistently compare and show the particles that have an average diameter of 70 to 110 nm, as reinforced in Fig. 5.28 (e) and Fig. 5.28 (f). The measured sizes agree well with those obtained from electron microscopy of nanohorns [59]. The profiles in Fig. 5.28 (e) and (f), have been taken along Γ_1 and Γ_2 across buried nanohorns in the images (c) and (d), and help to determine that no nanoparticle is seating on top of the cell. To determine if SWCNH association with erythrocytes was due to systemic translocation, as has been suggested in previous studies [87], we used MSAFM to image peripheral blood samples. The results of topographic and subsurface MSAFM imaging of peripheral blood from a control mouse are depicted in Fig. 5.29 (a) and (b), respectively. The corresponding images from an exposed mouse (Fig. 5.29 (c,d)) exhibit contrast areas with sizes matching those of the nanohorns. This observation is supported in the additional images presented in Fig. 5.29 (e-j). We note that, the difference in contrast between images in Fig. 5.27 (h) and 5.28 (d) (appearing in white) and Fig. 5.29 (j) (appearing in black) is due to a difference in the phase accretion associated with the coupling between the oscillations of the cantilever and the cell. The MSAFM images in Fig. 5.29 presenting an intracellular SWCNH population in the peripheral blood from exposed mice support the results of Geiser et al. [87], who observed that nano-sized polystyrene beads are taken up by erythrocytes in vitro. Similar to the case of SWCNH, topographic and MSAFM images reveal the presence of silica nanoparticles within the cell, confirming the ability to resolve features made of stiff material with MSAFM. In order to further validate our MSAFM results, that is, the detection of the presence of SWCNH within the cellular structure, we carried out Raman spectroscopy of the exposed and unexposed

macrophages. For a threshold number density of buried nanohorns, we would expect to observe a sufficient Raman yield. As shown in Fig. 5.30, apart from substrate effects, the Raman spectrum of the SWCNH exhibits a minor band at $985.9cm^{-1}$, and two major bands peaked at $k_D = 1300.6$, and $k_G = 1599.3cm^{-1}$ (20) (black curve in Fig. 5.30). The results capture the Raman signatures of both the BAL samples from vehicle control (Fig. 5.30 (b)) as well as those from the exposed mice (Fig. 5.30 (c)). The insets (Fig. 5.30 (a)) show the locations at which spectra were obtained (L_i). No traces of SWCNH could be found in the case of control macrophages (Fig. 5.30 (b)) as opposed to the case of exposed mouse where a strong SWCNH can readily be identified (Fig. 5.30 (c)) with the D and G bands [92, 93]. No SWCNH bands could be detected in regions exterior to the macrophages as shown in the measurements at points L_1 and L_2. Due to the lower number densities of the SWCNH, and consistent with the optical images, in the case of erythrocytes, no Raman shift could be measured in the regions occupied by the cells from both the BAL samples and the peripheral blood extracted from the mice. Furthermore, the measurements were repeated for silica nanospheres [77], and a comparison of the results was carried out in [78].

Chapter 6

Conclusions and perspectives

Characterization of the physical and chemical properties of the surface and subsurface of soft materials with nanoscale spatial resolution is an important challenge in nanoscience. Such a tool would accelerate to quest for understanding and predicting the fundamental mechanisms of natural phenomena occurring at the nanoscale. Nanosciences impose a strong interdisciplinary approach to create cutting edge instruments for the growing interest of probing biological system at the sub-cellular level.

6.1 The great promises of MSAFM

We have described a new modality of force microscopy that can be of significant importance for nanoscale characterization of material. In a single run, MSAFM is capable of delivering a myriad (Fig. 5.2) of nanoscale features not attainable by other means. Controlled use of the synthesized modes for surface and subsurface characterization of biological cells demonstrate the versatility of presented methodology and suggest potential application in studying complex samples, such as an organic system that exhibits a variety of interrelated chemical, morphological, and mechanical properties, as opposed to simple samples characterized rather with homogeneity, uniformity, and isotropy. The experimental observation that the force is not maximum at the

collapse point of the probe implies that both attractive and repulsive forces are at play under MSAFM. We demonstrated that, within the measurement bandwidth, the $\mathcal{C}_{\pm}^{\beta}$ modes are all fully operational. Further work on MSAFM will provide information on whether or not the observed states can be coherent, opening up for additional phase measurements. MSAFM capitalizes on the full range of frequencies, and utilizes both amplitude and phase towards image formation, therefore many opportunities remain to be explored.

6.2 Subsurface detection of nanoparticles for nanotoxicology studies

The net effect of nanoparticle exposure on health [81, 82] is an area of active research and controversy. Understanding the fate of nanoparticles within the body is critical both to assessing their potential toxicity [94, 95, 96] and efficacy to realize their potential as vehicles of drug delivery [61]. We have, for the first time, demonstrated that MSAFM offers a means to monitor the cellular deposition of nanoparticles following in vivo exposures. MSAFM [76, 55] offers a potential circumvention enabling subsurface imaging of soft samples suggesting it to be a potential method to probe cellular uptake of nanoparticles. To summarize, our MSAFM results show presence of nanoparticles within macrophages of mice lungs exposed to carbon nanohorns and silica nanoparticles. We visualized nanoparticles within both alveolar macrophages and peripheral erythrocytes (red blood cells). Micro Raman spectroscopy carried out on macrophages support our conclusion of SWCNH within the cells. The subsurface imaging capability of MSAFM will help advance the field of nanoparticles-cell interactions. Importantly, advantages of this method include high-resolution subsurface imaging and localization of nanoparticle in biological samples, its compatibility with ambient conditions, minimal sample preparation, and does not require any labeling. Moreover, compared to techniques

such as TEM, MSAFM offers relatively high-throughput sample analysis, enabling the imaging of a population of cells within a reasonable time-frame. The MSAFM method should be particularly useful for determining the efficacy of cell type-specific drug targeting, which is a critical goal for medical uses of nanomaterials. Morphological parameters of cells can be used to distinguish cell types within a sample, providing the ability to assess cell type-specific particle uptake without the need for labeling, required by many other imaging techniques. This method could also be useful in screening for nanoparticle exposure risk using peripheral blood. It is expected that our results will prove useful in resolving critical questions about the fate and potential toxicity of nanoparticles within the body.

6.3 Toward a better understanding of biomass at the cell wall level

Increasing the dynamic attributes of the probe of an AFM that permits simultaneous acquisition of manifold nanoscale information is of great potential application in nanoscience [62, 63, 15, 64]. We showed that such a boost in information dimensionality can be accomplished via a diversification of the frequency content of a force probe. We introduced the concept of MSAFM by presenting the experimental manifestation of a local mechanical probe-sample coupling that facilitates sensitive amplitude and phase mapping of nanoscale material features. It was shown that such a coupling is not unique in the excitation parameter space of the system but forms bands that occupy several megahertz of available frequencies. The rich spectrum of first- and higher-order couplings discovered, was applied to plant cell characterization, aiding the emergent challenges of efficient biomass conversion for biofuel production will be further developed. In addition spectroscopic information on wood cross sections were obtained and demonstrate the evolution in chemical content of the cell walls after various chemical treatments, representative of the chemical treatment used in

its conversion to biofuel. We also studied the chemical composition of the cell wall at the subwavelength scale using MSAFM while illuminating the sample with infrared light. The FTIR results exhibit complex signatures. The laser induced response (single wavelength) reveal the different absorption of energy by the cell walls with respect to the wavelength of illumination. It is expected that our preliminary results will lead to important discoveries in understanding recalcitrance, and has the potential to reach out to many other fields of science.

6.4 Future directions

Understanding complex systems at the nanoscale will have major impacts on world challenges (environment, energy, health, $\cdots$). The development of new tools capable of probing material properties at relevant spatial and temporal scales is necessary. Thus, a tool providing simultaneous morphological, physical, and chemical information at the nanoscale will undoubtedly pave the way to groundbreaking discoveries.

Bibliography

[1] R.P. Feynman. Plenty of room at the bottom. In *Presentation to American Physical Society*, 1959. 1, 2

[2] G. Binnig, H. Rohrer, Ch. Gerber, and E. Weibel. Surface studies by scanning tunneling microscopy. *Physical Review Letters*, 49:57–61, 1982. 2, 7

[3] H.W. Kroto, J.R. Heath, S.C. O'Brien, R.F. Curl, and R.E. Smalley. C60: Buckminsterfullerene. *Nature*, 318:162–163, 1985. 2

[4] G. Binnig, C.F. Quate, and Ch. Gerber. Atomic force microscopy. *Physical Review Letters*, 56:930–933, 1986. 2, 7, 8, 10

[5] M.H. Gass, U. Bangert, A.L. Bleloch, P. Wang, R.R. Nair, and A.K. Geim. Free-standing graphene at atomic resolution. *Nature Nanotechnology*, 3:676–681, 2008. 2

[6] A.K. Geim and A.H. MacDonald. Graphene: Exploring carbon flatland. *Physics Today*, pages 35–41, 2007. 2

[7] K.S. Novoselov, A.K. Geim, S.V. Morozov, D. Jiang, M.I. Katsnelson, I.V. Grigorieva, S.V. Dubonos, and A.A. Firsov. Two-dimensional gas of massless dirac fermions in graphene. *Nature*, 438:197–200, 2005. 2

[8] K.S. Novoselov, A.K. Geim, S.V. Morozov, D. Jiang, Y. Zhang, S.V. Dubonos, I.V. Grigorieva, and A.A. Firsov. Electric field effect in atomically thin carbon films. *Science*, 306:666–669, 2004. 2

[9] A.F. Young and P. Kim. Quantum interference and klein tunneling in graphene heterojunctions. *Nature Physics*, 5:222–226, 2009. 2

[10] D.M. Price, M. Reading, A. Hammiche, and H.M. Pollock. New adventures in thermal analysis. *Journal of Thermal Analysis and Calorimetry*, 60(3):723–733, 2000. 3

[11] A. Dazzi, S. Goumri-Said, and L. Salomon. Theoretical study of an absorbing sample in infrared near-field spectromicroscopy. *Optics Communications*, 235(4-6):351–360, 2004. 3

[12] A. Dazzi, R. Prazeres, E. Glotin, and J.M. Ortega. Local infrared microspectroscopy with subwavelength spatial resolution with an atomic force microscope tip used as a photothermal sensor. *Optics Letters*, 30(18):2388–2390, 2005. 3

[13] G. Binnig, H. Rohrer, Ch. Gerber, and E. Weibel. Tunneling through a controllable vacuum gap. *Appl. Phys. Lett.*, 40:178–180, 1982. 7, 10

[14] G. Binnig, Ch. Gerber, E. Stoll, T.R. Albrecht, and C.F. Quate. Atomic resolution with atomic force microscope. *Europhys. Lett.*, 3:1281–1286, 1987. 7

[15] R. Garcia, R. Margerle, and R. Perez. Nanoscale compositional mapping with gentle forces. *Nature Materials*, 6:405–411, 2007. 8, 31, 50, 87, 93

[16] B. Herman and J.J. Lemasters. *Optical microscopy: Emerging Methods and Applications*. Academic Press, New York, 1993. 8

[17] J.A. Conchello and J.W. Lichtman. Optical sectioning microscopy. *Nature Methods*, 2:920–931, 2005. 8

[18] Amos. W.B. and J.G. White. How the confocal laser scanning microscope entered biological research. *Biology of the cell*, 95:335–342, 2003. 8

[19] G. Cox. Biological confocal microscopy. *Materials Today*, 5:34–41, 2002. 8

[20] E. Ruska. The development of the electron microscope and of electron microscopy. *Nobel Lecture*, 1986. 9

[21] J. Faist, F. Capasso, D.L. Sivco, C. Sirtori, A.L. Hurtchinson, and A.Y. Cho. Quantum cascade laser. *Science*, 264:553–556, 1994. 9, 42, 43

[22] A.M. Donald. The use of environmental scanning electron microscopy for imaging wet and insulating materials. *Nature materials*, 2:511–516, 2003. 9

[23] R. Wiesendanger. *Scanning probe microscopy and spectroscopy.* Cambridge University Press, 1994. 10

[24] E.H. Synge. A suggested method for extending the microscopic resolution into the ultramicroscopic region. *The London, Edinburgh, and Dublin Philisophical Magazine and Journal of Science*, 6:356–362, 1928. 10, 11

[25] E.A. Ash and G. Nicholls. Super-resolution aperture scanning microscope. *Nature*, 237:510–512, 1972. 10, 11

[26] M.F. Garcia-Parajo. Optical antennas focus in on biology. *Nature Photonics*, 2:201–202, 2008. 11

[27] T. S. Van Zanten, A. Cambi, M. Koopman, B. Joosten, C.G. Figdor, and M. F. Garcia-Parajo. Hotspots of gpi-anchored proteins and integrin nanoclusters function as nucleation sites for cell adhesion. *PNAS*, 106:18557, 2009. 11

[28] E. Betzig, J.K. Trautman, T.D. Harris, J.S. Weiner, and R.L. Kostelak. Breaking the diffraction barrier: Optical microscopy at the nanometric scale. *Science*, 251:1468–1470, 1991. 11

[29] B. Bushan. *Handbook of Micro/Nanotribology.* Boca Raton, 1999. 12

[30] C. D. Frisbie, L. F. Rozsynai, A. Noy, M. S. Wrighton, and C. M. Lieber. Functional group imaging by chemical force microscopy. *Science*, 265:2071, 1994. 13

[31] A. Noy, D. V. Vezenov, and C. M. Lieber. Chemical force microscopy. *Annu. Rev. Mater. Sci.*, 27:381, 1997. 13

[32] J. Zlatanova, S. M. Lindsay, and S. H. Leuba. Single molecule force spectroscopy using the atomic force microscope. *Prog. Biophys. Mol. Biol.*, 74:37, 2000. 13

[33] A. Dazzi, R. Prazeres, F. Glotin, J. M. Ortega, M. Al-Sawaftah, and M. de Frutos. Chemical mapping of the distribution of viruses into infected bacteria with a photothermal method. *Ultramicroscopy*, 108:635–641, 2008. 13

[34] A. Dazzi. PhotoThermal Induced Resonance. Application to Infrared Spectromicroscopy. In *Thermal Nanosystems and Nanomaterials*, volume 118 of *Topics in Applied Physics*, pages 469–503. Springer-Verlag Berlin, 2009. 13

[35] K. Kjoller, J. R. Felts, D. Cook, C. B. Prater, and W. P. King. High-sensitivity nanometer-scale infrared spectroscopy using a contact mode microcantilever with an internal resonator paddle. *Nanotechnology*, 21(18), 2010. 14

[36] A. Hammiche, L. Bozec, H.M. Pollock, M. German, and M. Reading. Progress in near-field photothermal infra-red microspectroscopy. *Journal of Microscopy-Oxford*, 213:129–134, 2004. 14

[37] M. Elwenspoek and R. Wiegerink. *Mechanical Microsensors*. Springer, 2001. 15, 18

[38] H. Goldstein. *Classical Mechanics*. Addison-Wesley Publishing Company, 1980. 15

[39] N. Jalili, M. Dadfarnia, and D. Dawson. A fresh insight into the microcantilever-sample interaction problem in non-contact atomic force microscopy. *Journal of Dynamic Systems, Measurement, and Control*, 126:327, 2004. 21

[40] V.P. Carey, G. Chen, C. Grigoropoulos, M. Kaviany, and A. Majumdar. A review of heat transfer physics. *Nanoscale and microscale thermophysical engineering*, 12(1):1–60, 2008. 27

[41] H. Curtis and S. N. Barnes. *Biology*. New York: Worth Publishers, 1989. 30

[42] M. Schmid, W. Hebenstreit, and P. Varga. Quantum wells and electron interference phenomena in al due to subsurface noble gas bubbles. *Phys. Rev. Lett.*, 76:2298–2301, 1996. 30

[43] M.K. Rose, A. Borg, T. Mitsui, D.F. Ogletree, and Salmeron M. Subsurface impurities in pd(111) studied by scanning tunneling microscopy. *Journal of Chemical Physics*, 115:10927–10935, 2001. 30, 31

[44] M.C.M.M. Van der Wielen, A.J.A. van Roij, and H. van Kempen. Direct observation of friedel oscillations around incorporated si dopants in gaas by low-temperature scanning tunneling microscopy. *Phys. Rev. Lett.*, 76:1075–1078, 1996. 30

[45] B.D. Huey. Afm and acoustics: fast, quantitative nanomechanical mapping. *Annual Review of Materials Research*, 37:351–385, 2007. 31

[46] O.V. Kolosov and K. Yamanaka. Nonlinear detection of ultrasonic vibrations in an atomic force microscope. *Japanese journal of applied physics*, 32(8A):L1095–L1098, 1993. 32

[47] O.V. Kolosov, R.C. Martin, C.D. Marsh, G.A. Briggs, T.I. Kamins, and R.S. Williams. Imaging the elastic nanostructures of ge islands by ultrasonic force microscopy. *Physical Review Letters*, 81(5):1046, 1998. 32, 87

[48] U. Rabe and W. Arnold. Acoustic microscopy by atomic force microscopy. *Applied Physics Letters*, 64:1493–1495, 1994. 32, 87

[49] A. San Paulo, J.P. Black, R.M. White, and J. Bokor. Detection of nanomechanical vibrations by dynamic force microscopy in higher cantilever eigenmodes. *Appl. Phys. Lett.*, 91:053116:1–3, 2007. 32

[50] W. Rohrbeck and E. Chilla. Detection of surface acoustic waves by scanning force microscopy. *Phys. Stat. Sol. (a)*, 131:69–71, 1992. 33

[51] E. Chilla, T. Hesjedal, and H.-J. Frohlich. Nanoscale determination of phase velocity by scanning acoustic force microscopy. *Phys. Rev. B*, 55:15852–15855, 1997. 33

[52] N. Anderson, P. Anger, A. Hartschuh, and L. Novotny. Subsurface raman imaging with nanoscale resolution. *Nano Letters*, 6:744–749, 2006. 33

[53] T. Taubner, F. Keilmann, and R. Hillenbrand. Nanoscale-resolved subsurface imaging by scattering-type near-field optical microscopy. *Optics Express*, 13:8893–8899, 2005. 34

[54] U. Rabe, K. Janser, and W. Arnold. Vibrations of free and surface-coupled atomic force microscope cantilevers: Theory and experiment. *Review of scientific instrument*, 67:3281–3293, 1996. 40

[55] L. Tetard, A. Passian, and T. Thundat. New modes for subsurface atomic force microscopy through nanomechanical coupling. *Nature Nanotechnology*, 5:105–109, 2010. 40, 51, 52, 55, 56, 60, 70, 71, 74, 75, 76, 80, 87, 92

[56] M. Beck, D. Hofstetter, T. Aellen, J. Faist, U. Oesterle, M. Iligems, E. Gini, and H. Melchior. Continuous wave operation of a mid-infrared semiconductor laser at room temperature. *Science*, 295:301–305, 2002. 43

[57] L.R. et al. Lynd. How biotech can transform biofuels. *Nature Biotechnology*, 26:169–172, 2008. 45, 74

[58] S. Jung, M. Foston, M. Cameron Sullard, and A.J. Ragauskas. Surface characterization of dilute acid pretreated *Populus deltoides* by ToF-SIMS. *Energy Fuels*, 24:1347–1357, 2010. 45, 81

[59] S. Iijima, M. Yudasaka, R. Yamada, S. Bandow, K. Suenaga, F. Kokai, and K. Takahashi. Nano-aggregates of single-walled graphitic carbon nano-horns. *Chemical Physics Letters*, 309(3-4):165–170, 1999. 46, 89

[60] E.R. Shvedova, A.A.and Kisin, R. Mercer, A.R. Murray, V.J. Johnson, A.I. Potapovich, Y.Y. Tyurina, O. Gorelik, S. Arepalli, D. Schwegler-Berry, A.F. Hubbs, J. Antonini, D.E. Evans, B.K. Ku, D. Ramsey, A. Maynard, V.E. Kagan, V. Castranova, and P. Baron. Unusual inflammatory and fibrogenic pulmonary responses to single-walled carbon nanotubes in mice. *American Journal of Physiology-Lung Cellular and Molecular Physiology*, 289(5):L698–L708, 2005. 47

[61] G.V.S. Rao, S. Tinkle, D.N. Weissman, J.M. Antonini, M.L. Kashon, R. Salmen, L.A. Battelli, P.A. Willard, A.F. Hubbs, and M.D. Hoover. Efficacy of a technique for exposing the mouse lung to particles aspirated from the pharynx. *Journal of Toxicology and Environmental Health-Part A*, 66(15):1441–1452, 2003. 47, 92

[62] O. Sahin, S. Magonov, C. Su, C. F. Quate, and O. Solgaard. An atomic force microscope tip designed to measure time-varying nanomechanical forces. *Nature Nanotechnology*, 2(8):507–514, 2007. 50, 93

[63] O. Sahin. Scanning below the cell surface. *Nature Nanotechnology*, 3:461–462, 2008. 32, 50, 87, 93

[64] R. Garcia. Images from below the surface. *Nature Nanotechnology*, 5:101–102, 2010. 51, 55, 93

[65] R. W. Boyd. *Nonlinear Optics*. Academic Press second edition, 2002. 57

[66] A. Passian, A.L. Lereu, D. Yi, S. Barhen, and T. Thundat. Stochastic excitation and delayed oscillation of a micro-oscillator. *Physical Review B*, 75:233403, 2007. 61

[67] A. Wig, E.T. Arakawa, A. Passian, T.L. Ferrell, and T. Thundat. Photothermal spectroscopy of bacillus anthracis and bacillus cereus with microcantilevers. *Sensors and Actuators B*, 114:206, 2006. 61

[68] E.F. Nichols and G.F. Hull. A preliminary communication on the pressure of heat and light radiation. *Physical Review (Series I)*, 13:307–320, 1901. 61

[69] A. Wig, A. Passian, E.T. Arakawa, T.L. Ferrell, and T. Thundat. Optical thin film interference effects in microcantilevers. *Journal of Applied Physics*, 95:1162–1165, 2004. 61, 69

[70] L. Tetard, A. Passian, U.C. Farahi, R.H. Kalluri, B.H. Davison, and T. Thundat. Spectroscopy and atomic force microscopy of biomass. *Ultramicroscopy*, 2010. 65, 80

[71] M. Tsuboi. Infrared spectrum and crystal structure of cellulose. *Journal of polymer science*, 25:159–171, 1957. 68

[72] V. Pini, B. Tiribilli, C.M.C. Gambi, and M. Vassalli. Dynamical characterization of vibrating afm cantilevers forced by photothermal excitation. *Phys. Rev. B*, 81:054302, 2010. 70

[73] D. J. Cosgrove. Growth of the plant cell wall. *Nature Reviews Molecular Cell Biology*, 6:850–861, 2005. 74

[74] P. Albersheim, A. Darvill, K. Roberts, R. Sederoff, and R. Staehelin. *Plant Cell Walls*. Taylor and Francis. 81

[75] D. Harris, V. Bulone, S.-Y. Ding, and Seth DeBolt. Tools for cellulose analysis in plant cell walls. *Plant Physiology*, 153:420–426, 2010. 81

[76] L. Tetard, A. Passian, K.T. Venmar, R.M. Lynch, B.H. Voy, G. Shekhawat, V.P. Dravid, and T. Thundat. Imaging nanoparticles in cells by nanomechanical holography. *Nature Nanotechnology*, 3:501–505, 2008. 83, 84, 85, 86, 87, 92

[77] L. Tetard, A. Passian, R.M. Lynch, B.H. Voy, G. Shekhawat, V.P. Dravid, and T. Thundat. Elastic phase response of silica nanoparticles buried in soft matter. *Applied Physics Letters*, 93:133113, 2008. 85, 90

[78] L. Tetard, A. Passian, R.H. Farahi, and T. Thundat. Atomic force microscopy of silica nanoparticles and carbon nanohorns in macrophages and red blood cells. *Ultramicroscopy*, 2010. 85, 90

[79] A. Nel, T. Xia, L. Madler, and N. Li. Toxic potential of materials at the nanolevel. *Science*, 311(5761):622–627, 2006. 87

[80] Panessa-Warren, B. J. and Warren, J. B. and Wong, S. S. and Misewich, J. A. Biological cellular response to carbon nanoparticle toxicity. *Journal of Physics-Condensed Matter*, 18:S2185–S2201, 2006. International School and Workshop on Nanoscience and Nanotechnology, Monte Porzio Catone, ITALY, NOV 14-16, 2005. 87

[81] V. Stone and K. Donaldson. Nanotoxicology - Signs of stress. *Nature Nanotechnology*, 1(1):23–24, 2006. 87, 92

[82] V.L. Colvin. The potential environmental impact of engineered nanomaterials. *Nature Biotechnology*, 21(10):1166–1170, 2003. 87, 92

[83] P. J. Borm. *Part. Fibre Toxicol.*, 3, 2006. 87

[84] T. Xia, M. Kovochich, J. Brant, J.and Oberley T. Hotze, M.and Sempf, C. Sioutas, J. I. Yeh, M. R. Wiesner, and A. E. Nel. Comparison of the abilities of ambient and manufactured nanoparticles to induce cellular toxicity according to an oxidative stress paradigm. *Nano Letters*, 6(8):1794–1807, 2006. 87

[85] Oberdörster, G. and Oberdörster, E. and Oberdörster, J. Nanotoxicology: An emerging discipline evolving from studies of ultrafine particles. *Environmental Health Perspectives*, 113(7):823–839, 2005. 87

[86] M.P. Holsapple, W.H. Farland, T.D. Landry, N.A. Monteiro-Riviere, J.M. Carter, N.J. Walker, and K.V. Thomas. Research strategies for safety evaluation of nanomaterials, part II: Toxicological and safety evaluation of nanomaterials, current challenges and data needs. *Toxicological Sciences*, 88(1):12–17, 2005. 87

[87] M. Geiser, B. Rothen-Rutishauser, N. Kapp, S. Schurch, W. Kreyling, H. Schulz, M. Semmler, V.I. Hof, J. Heyder, and P. Gehr. Ultrafine particles cross cellular membranes by nonphagocytic mechanisms in lungs and in cultured cells. *Environmental Health Perspectives*, 113(11):1555–1560, 2005. 87, 89

[88] J.M. Wörle-Knirsch, K. Pulskamp, and H.F. Krug. Oops they did it again! Carbon nanotubes hoax scientists in viability assays. *Nano Letters*, 6(6):1261–1268, 2006. 87

[89] A. E. Porter, M. Gass, K. Muller, J. N. Skepper, P. A. Midgley, and M. Welland. Direct imaging of single-walled carbon nanotubes in cells. *Nature Nanotechnology*, 2(11):713–717, 2007. 87

[90] N. F. Martinez, S. Patil, J. R. Lozano, and R. Garcia. Enhanced compositional sensitivity in atomic force microscopy by the excitation of the first two flexural modes. *Applied Physics Letters*, 89(15), 2006. 32, 87

[91] G.S. Shekhawat and V.P. Dravid. Nanoscale imaging of buried structures via scanning near-field ultrasound holography. *Science*, 310:89–92, 2005. 87

[92] M.J. Mathews, M.A. Pimenta, G. Dresselhaus, M.S. Dresselhaus, and M. Endo. Origins of dispersive effects of the raman d band in carbon materials. *Physical Review B*, 59:R6585–R6588, 1999. 90

[93] F. Tuinstra and J.L. Koenig. Raman Spectrum of Graphite. *Journal of Chemical Physics*, 53(3):1126–&, 1970. 90

[94] C.W. Lam, J.T. James, R. McCluskey, and R.L. Hunter. Pulmonary toxicity of single-wall carbon nanotubes in mice 7 and 90 days after intratracheal instillation. *Toxicological Sciences*, 77(1):126–134, 2004. 42nd Annual Meeting of the Society-of-Toxicology, Salt Lake City, Utah, Mar 09-13, 2003. 92

[95] C. Medina, M. J. Santos-Martinez, A. Radomski, O. I. Corrigan, and M. W. Radomski. Nanoparticles: pharmacological and toxicological significance. *British Journal of Pharmacology*, 150(5):552–558, 2007. 92

[96] X. Fan, J. Tan, G. Zhang, and F. Zhang. Isolation of carbon nanohorn assemblies and their potential for intracellular delivery. *Nanotechnology*, 18(19), 2007. 92

Vita

Laurene Tetard was born in Troyes, France on August 29, 1983. She studied in France until she graduated with a Master of Science degree in Physics from the Université de Bourgogne in Dijon in 2006. The same year, she moved to Knoxville, Tennessee (USA) and started her graduate work in the Physics Department at the University of Tennessee. She worked as a Graduate Research Assistant in Dr. Thomas Thundat's group at the Oak Ridge National Laboratory (ORNL) for five years, under the supervision of Dr. Ali Passian. She was awarded the Chancellor's Honors for Extraordinary Professional Promise in 2010. She was also one of the recipients of the R&D100 2010 awards for the work on subsurface imaging at the nanoscale. In the course of her graduate work, she has co-authored two patents on subsurface imaging and chemical characterization at the nanoscale and several publications on Scanning Probe Microscopy.